Optical and Related Properties of Inorganic Nanoparticles

A Thesis

Submitted For the Degree of

Doctor of Philosophy

by

S. Venkataprasad Bhat

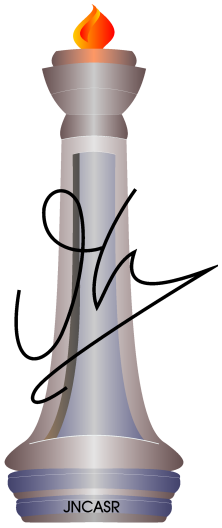

Chemistry and Physics of Materials Unit
Jawaharlal Nehru Centre for Advanced Scientific Research
Bangalore – 560 064

OCTOBER 2010

To all who excite the spectra..

DECLARATION

I hereby declare that the matter embodied in the thesis entitled "**Optical and Related Properties of Inorganic Nanoparticles**" is the result of investigations carried out by me at the Chemistry and Physics of Materials Unit, Jawaharlal Nehru Centre for Advanced Scientific Research, Bangalore, India under the supervision of Prof. C.N.R.Rao and that it has not been submitted elsewhere for the award of any degree or diploma.

In keeping with the general practice in reporting scientific observations, due acknowledgement has been made whenever the work described is based on the findings of other investigators.

S. Venkataprasad Bhat

CERTIFICATE

I hereby certify that the matter embodied in this thesis entitled "**Optical and Related Properties of Inorganic Nanoparticles**" has been carried out by Mr. S. Venkataprasad Bhat at the Chemistry and Physics of Materials Unit, Jawaharlal Nehru Centre for Advanced Scientific Research, Bangalore, India under my supervision and that it has not been submitted elsewhere for the award of any degree or diploma.

Prof. C.N.R.Rao
(Research Supervisor)

Acknowledgements

I acknowledge Prof. C.N.R. Rao, FRS for giving me this opportunity to work under his guidance, suggesting the problems and introducing me into different areas of research. I express my sincere gratitude to him for his immense support, guidance and inspiration.

I am extremely grateful to Dr. A. Govindaraj for teaching me the various aspects of experimental research and for his constant encouragement and help throughout the project work.

I thank the past and present chairmen of CPMU, Prof. C. N. R. Rao, FRS and Prof. G. U. Kulkarni, President M. R. S. Rao, for providing me the various facilities to carry out my research work. Thanks to CSIR for the research fellowship, IISc for the facilities.

I thank Dr. Deepak, Dr. Vivekchand, Dr. Biswas, Dr. Datta Late, Dr. Prashant Kumar, Dr. Mangalam, Gomathi, Basant, A.Ghosh, Sahu, Dr. Swain, Shrinu, Gopal for their invaluable help during the work. I thank Dr. G. De, Prof. S Ramakrishnan, Dr. Harish chander, Prof Sundaresan, Dr. Ranjan Datta, Prof. S. B. Krupanidhi, Dr. M. Thirumavalavan and Prof. Chandrabhas for their help and discussions.

I thank all the faculty members in JNC; In particular, Prof. Balasubramaniam, Prof. Chandrabhas, Prof. Kulkarni, Prof. Waghmare, Prof. Sundaresan, Prof. Swapan Pati for their informative courses.

I thank Anil, Basavaraj, Selvi, Srinath, Srinivas, Srinivasa Rao, Usha Madam and Vasu for their help in various measurements. I thank Veeco lab staff for the facilities and help. I also thank Arokianathan, Sunil and Moorthy for their assistance. I am thankful to all the office staff in CSIR-COE JNCASR, CPMU Office; Mrs. Sashi, Gowda, Xavier , Victor and Mrs. Sudha.

I would like to thank all my past and present lab mates; Drs. Gautam, Ujjal, Sardar, Motin, Deepak, Ashish, Behera, Ved, Dan, Moumita,Vivek, Thiru, Kalyani, Chandu and Kanishka; Gomathi, Leela, Subramanyam, Neenu, Bello, Manjunatha, Rakesh, Kalyan, Basant, Barun, Anupama, Claudy, Sahu, Matte, Sandeep, Urmi for their fruitful discussions and wonderful work atmosphere. I thank Postdocs, Visiting scientists and POCE, SRF students for their pleasant company. I thank all my batchmates and friends for their support.

I thank Mr. Jayachandra and staff members from administration, academic, complab, library and hostel for the services offered.

It is a pleasure to thank Mrs. Indumati Rao and Sanjay Rao for their wonderful hospitality.

I acknowledge all my teachers who guided me throughout my career.

I would like express by deepest regards to my parents and family for their love, patience, understanding and motivation.

I should be grateful to many people who have contributed to my growth and helped me in one or the other way. So I thank them all.

Preface

Many modern technologies have advanced to the point that the relevant feature size is on the order of a few to a few hundreds of nanometer. At the fundamental level, there is an urgent need to better understand the properties of materials on the nanoscale level. At the technological front, there is a strong demand to develop new techniques to fabricate and measure the properties of nanomaterials and related devices.

One of the most fascinating and useful aspects of nanomaterials is their optical properties. This thesis contains the results of the experiments carried out to study the optical and related properties of inorganic nanoparticles and is divided into seven parts. Part-1 of the thesis gives a brief overview of inorganic nanomaterials presenting their optical properties and related applications relevant for the studies carried out in the subsequent parts.

Part 2 deals with the results of investigations of ZnO nanoparticles and is divided into three sections. In section 1, the studies of changes in the band edge of ZnO nanoparticles doped with Mn, Co, and Ni are discussed along with their magnetic properties. Section 2 presents studies of photoluminescence and photoconducting properties of colloidal ZnO nanoparticles annealed in an oxygen atmosphere at various temperatures. Section 3 contains results of studies on the photoconductivity of ZnO-graphene nanocomposites.

Part 3 of the thesis, comprising two sections, contains results of investigations of GaN nanoparticles. Section 1 deals with the synthesis and optical properties of In doped GaN nanoparticles. White-light emission characteristics of nanocomposites based on GaN nanoparticles are examined in the second section.

Part 4 deals with the studies based on ReO_3 nanoparticles. Surface enhanced Raman scattering (SERS) from molecules adsorbed on nanoparticles of metallic ReO_3 is presented in Section 1. Section 2 presents studies of effect of these nanoparticles on the performance of silicon solar cell.

Part 5 presents the effect of refractive index of the medium on the luminescence bands of nanophosphors. Part 6 contains results of optical spectroscopic studies of composites of conducting polyaniline with CdSe and ZnO nanoparticles. In Part 7, a Raman study of the phase transition in $KHSO_4$ is presented.

Contents

Part 1

Inorganic Nanomaterials: A Brief Overview

1.1 Introduction

Over the past decade, nanomaterials have been the subject of enormous interest. These materials, notable for their extremely small feature size, have the potential for wide-ranging industrial, biomedical and electronic applications. Owing to the intriguing size-dependent properties of nanophase materials, the recent development of nanoscience and nanotechnology has opened up novel fundamental and applied frontiers in materials science and engineering. Simply saying, nanoscience tells us how to understand the basic theories and principles of nanoscale structures, devices and systems (1-100 nm) and nanotechnology tells us what to do and how to use these nanoscale materials.

Nanomaterials can be metals, ceramics, polymeric materials or composite materials. The unit of nanometer derives its prefix 'nano' from a Greek word meaning dwarf or extremely small. One nanometer spans 3-5 atoms lined up in a row. By comparison, the diameter of a human hair is about 5 orders of magnitude larger than a nanoscale particle. At the nanomaterial level,

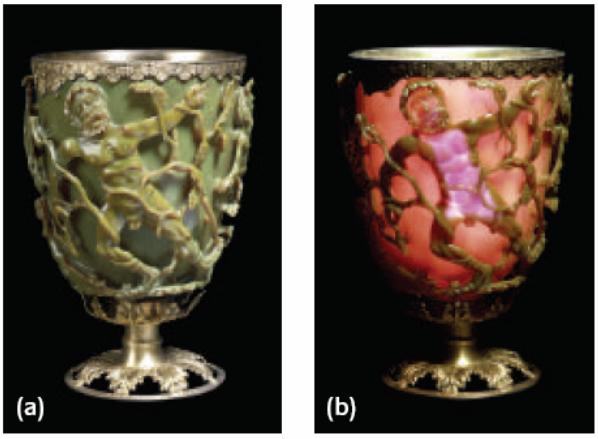

Figure 1.1.1: Lycurgus cup in (a) reflected and (b)transmitted light.

some material properties are affected by the laws of atomic physics rather than behaving as traditional bulk materials do. Surfaces and interfaces are also important in explaining nanomaterial behavior. In bulk materials, only a relatively small percentage of atoms will be at the surface or interface (like a crystal grain boundary). In nanomaterials, the small feature size ensures that many atoms will be near interfaces. Surface properties such as energy levels, electronic structure and reactivity can be quite different from interior states and give rise to quite different material properties.

Although widespread interest in nanomaterials is recent, the concept was raised over half a century ago. Physicist Richard Feynman delivered a talk in 1959 at the annual meeting of the American Physical Society at the California Institute of Technology (Caltech) entitled "There's Plenty of Room at the Bottom" in which he commented that there were no fundamental physical reasons that materials could not be fabricated by manoeuvring individual

atoms [1]. Nanomaterials have actually been produced and used by humans for hundreds of years. Clusters of metals are known from ancient times. They were employed to dye glass and fabrics and as a therapeutic aid in the treatment of arthritis. Purple of cassius, a popular purple dye in olden days was subsequently found to be made of tin oxide and Au nanoparticles. The secret behind the color of the Lycurgus cup (See Figure 1.1.1), a Roman glass artifact dated to 4 AD, that appears red in transmitted light and green in reflected light was found to be due to Au and Ag nanoparticles impregnated in glass [2]. The techniques used to produce these materials were considered trade secrets at the time and are not wholly understood even now.

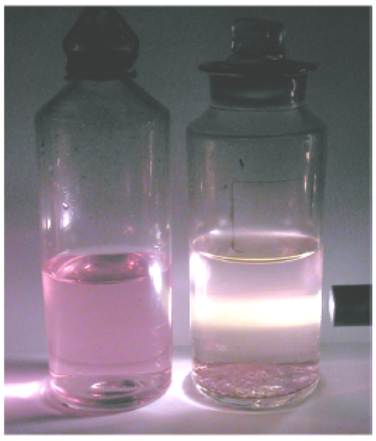

Figure 1.1.2: Gold colloid prepared in 1857 by Michael Faraday (on the right) along with a pink solution (on the left) made by him to resemble the colloids (from [3]).

Michael Faraday provided the first scientific description of the optical properties of nanometer-scale metals, which he termed as devided metals, in his classic 1857 paper [4]. He established that several dyes were indeed made

of metal particles. After a thorough study of gold sols, Faraday concluded "*... the gold is reduced in exceedingly fine particles, which becoming diffused, produce a beautiful ruby fluid... the various preparations of gold, whether ruby, green, violet or blue in colour... consist of that substance in a metallic divided state.*" Figure 1.1.2 shows one of the Faraday's gold colloids (on the right) along with a pink solution (on the left) made by Faraday to resemble the gold colloid, which are on display at Royal institution in London. Figure shows that only the gold colloid shows clear Faraday-Tyndall effect when light is transmitted through it [3].

The first scientific paper on nanotechnology was published in 1981 by Eric Drexler [5], a former student of Dr. Feynman at Caltech. Drexler's idea of molecular manufacturing was followed by his book [6] entitled: *Engines of Creation:The Coming Era of Nanotechnology* published in 1986 where he proposed the atom-stacking mechanism to produce machines smaller than a living cell and also presented some potential applications of nanotechnology. The main breakthrough in nanotechnology occurred in 1981 when Binnig and Rohrer [7] at IBM Zurich invented the scanning tunneling microscope (STM), the first instrument to generate real space images of surfaces with atomic resolution. This discovery opened up the important new field of nanotechnology and was recognized by the 1986 Nobel Prize in Physics, along with the inventor of the electron microscope.

Modern materials science is characterized by a close interplay between physics and chemistry. This is especially true for synthesis of nanomaterials. On the one hand are the top-down methods which rely on continuous breakup of a piece of bulk matter while on the other are the bottom-up methods that

build up nano materials from their constituent atoms. The top-down and bottom-up approaches can also be considered to be physical and chemical methods respectively. Most physical methods involve the evaporation of a solid material to form a supersaturated vapor from which homogenous nucleation of nanoparticles occurs. In these methods, the size of the particles is controlled by temporarily inactivating the source of evaporation or by slowing the rate by temporarily inactivating the source of evaporation or by introducing gas molecules to collide with the particles. Some of the physical methods used are arc discharge, ion sputtering, laser ablation, spray pyrolysis, ball milling *etc.*

Chemical methods are generally carried out under mild conditions and are relatively straight forward. Any chemical reaction resulting in a sol consists of three steps: seeding, particle growth and growth termination by capping. Nanocrystals can be prepared by several chemical methods, typical of them being reduction of salts, solvothermal synthesis and decomposition of molecular precursors, of which the first is the most common method used in the case of metal nanocrystals. Metal oxide nanocrystals are generally prepared by the decomposition of precursor compounds such as acetate, acetylacetonate and cuferronates in appropriate solvents, often under solvothermal conditions. Metal chalcogenide or pnictide nanocrystals are obtained by the reaction of metal salts with a chalcogen or pnicogen source or the decomposition of single source precursors under solvothermal or thermolysis conditions. Addition of suitable capping agents such as long-chain alkane thiols, alkyl amines and trioctylphosphine oxide (TOPO) during the synthesis of

nanocrystals enables the control of size and shape. Monodisperse nanocrystals are obtained by post-synthesis size-selective precipitation. Core@shell particles involving metal, semiconductor or oxide nanocrystals in the core, with shells composed of different materials have also been investigated [8–10].

1.2 Optical properties

Optical properties of nanomaterials are among the most exploited and useful properties for technological applications [11]. The optical properties of nanomaterials, similar to other properties, depend on parameters such as size, shape, surface characteristics and other variables including doping and interaction with the surrounding environment. Many of the fascinating color effects in nature are due to optical phenomena such as interference, diffraction and scattering involving nanostructured materials [12].

The electronic energy levels and density of states (DOS) determine the properties of materials including optical and electronic properties as well as their functionalities. For nanoscale materials, the energy levels and DOS vary as a function of size resulting in dramatic changes in the materials properties. The energy level spacing increases with decreasing dimension and this is known as the quantum size confinement effect.

For semiconductors, the Fermi level, E_F is in between the filled (valence band) and the unfilled (conduction band) levels. The minimum amount of energy required for the formation of electron - hole pair upon excitation is the bandgap energy of the semiconductor. It is the energy difference between the top of the valence band and the bottom of the conduction band. When the size of the semiconductor material becomes smaller than the Bohr radius, it

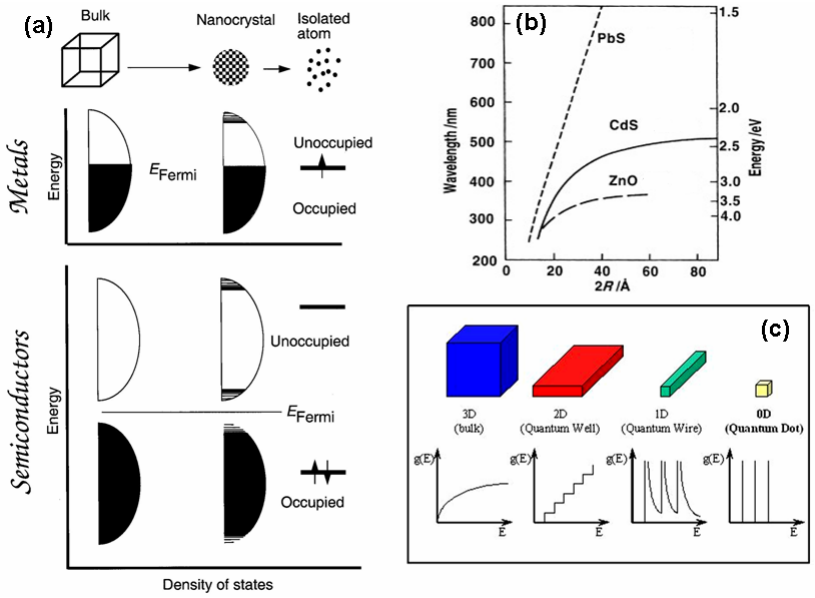

Figure 1.2.1: (a) Density of states for metal and semiconductor nanocrystals compared to those of the bulk and of isolated atoms, (b) Variation of bandgap of semiconductor nanoparticles as a function of their diameter and (c) Variation of density of states with the dimensionality (from [13]).

would decrease the space in which the charge carriers move and thus confine their motion. The situation is equivalent to the motion of an electron in a box, whose energy eigenvalues (E_n) are given by

$$E_n = \frac{n^2\pi^2\hbar^2}{2mL^2} \tag{1.2.1}$$

where m is the effective mass. As the size of the box (L) is reduced, the energy level spacing increases since it is inversely proportional to L^2. Thus, as the size of the nanoparticles decreases, the energy levels become discrete and the bandgap effectively increases (Figure 1.2.1a). Bulk metals possess a partially filled electronic band and their ability to conduct electrons is due

to the availability of a continuum of energy levels above the Fermi level, E_F. However when bulk metal is broken down, the continuum of electronic states break down and ultimately, the material becomes insulating. The excitonic nature of the light absorption in semiconductor nanoparticles permits direct correlation of the bandgap with the absorption edge. A high-quality absorption spectrum for monodisperse nanoparticles can be used to calculate size of the synthesized nanoparticles directly. Fig 1.2.1(b) shows the empirical relationships between the diameter and the bandgap for various semiconductor nanoparticles [8, 13].

Similarly, the shape of the nanoparticles plays a crucial parameter in the determination of their properties [14–16]. The DOS (g(E)) of nanoparticles simultaneously evolves from continuous levels into discrete states as the dimensionality is decreased from 3D to 0D as described by the relation g(E) $\propto E^{\frac{n}{2}-1}$, where n is the dimensionality and E is the energy (Figure 1.2.1c). In 3D materials, g(E) is a smooth square root function of energy. The 2D sheet is confined along a specific direction (*e.g.* z-axis) and show staircase like DOS. 1D rods or tubes confined along two directions (*e.g.* x, y direction) show saw-tooth like DOS, while for 0D particles it is like δ -function [17].

The quantum size confinement effect becomes significant particularly when the particle size becomes comparable to or smaller than the Bohr exciton radius. The simplest example is the well-known blue-shift of absorption and photoluminescence spectra of semiconductor nanoparticles with decreasing particle size, particularly when the size is small enough. Figure 1.2.2 shows optical emission colors and absorption spectra of different sized CdSe nanoparticles or quantum dots (QDs) [18]. The absorption spectra show a

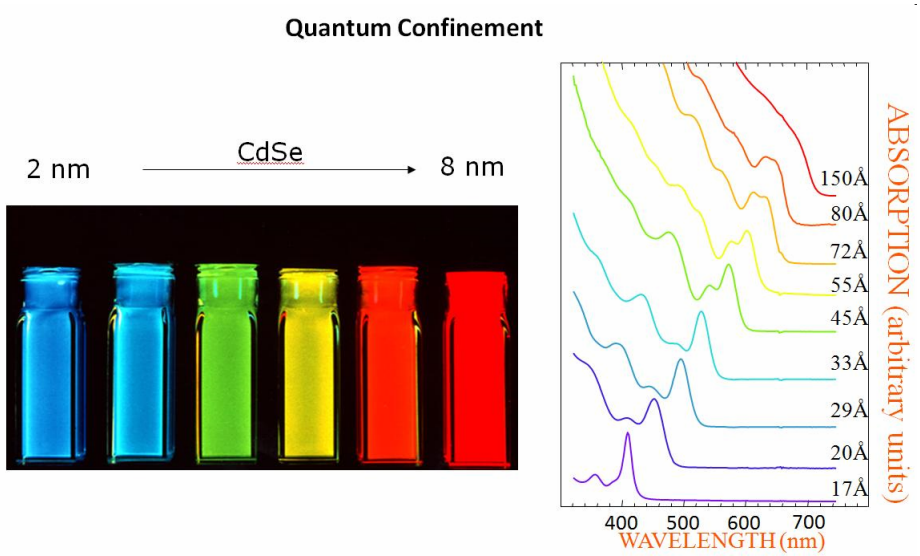

Figure 1.2.2: Left: Fluorescence image of CdSe QDs as a function of size. Right: Absorbance spectrum as a function of size (From [18, 19]).

consistent red shift as the size of the particle increases. The emission from monodisperse semiconductor nanoparticles such as CdSe is intense, narrow and can be tuned across the visible spectrum by changing the size. Further control over the emission can be exercised by varying the surface structure and controlling diameter distribution. The optical properties of the semiconductor nanoparticles also change with the shape (Figure 1.2.3) [20]. The quantum confinement effect in the case of reduction in the length of the nanorods is weaker than the effect observed for diameter reduction. The emission from CdSe nanoparticles changes from non-polarized to purely linearly polarized as the nanoparticle shape evolves from spherical to rod-like [16].

Due to the fact that the band edge is more affected by quantum confinement and the Fermi level of metal is at the center of the band, metals

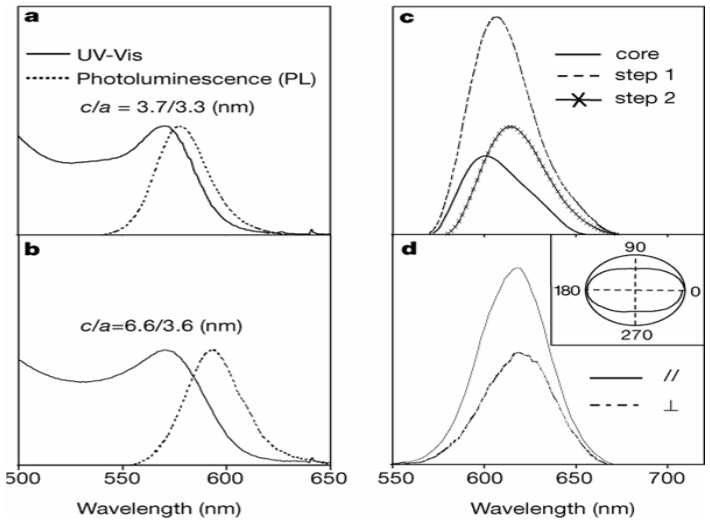

Figure 1.2.3: Absorbance and photoluminescence (PL) spectra of CdSe (a) nanoparticles and (b) nanorods of comparable diameter, (c) Photoluminescence spectra of core@shell nanorods with different shell thickness and (d) Polarization resolved PL spectra of CdSe nanorods at 4.7 K, recorded with the detecting polarization direction parallel (parallel) and perpendicular (perpendicular) to the direction of stretching of the polymer in which the nanorods are alligned to a certain extent. Inset in (d) gives the polar plot of the integrated PL as a function of the angle between the detecting polarization direction and the polymer stretching direction (From [20]).

are less affected by spatial confinement than semiconductors for similar size range. The optical properties of metal nanostructures in the visible region are dominated by the surface plasmon absorption caused by collective conduction band electron oscillation in response to the electrical field of the light radiation (Figure 1.2.4a). The surface plasmon resonance was theoretically explained by Mie in 1908 [21], including linear optical properties such as extinction and scattering of small nanoparticles. The frequency and width of the surface plasmon absorption depends on the size and shape of the metal nanoparticles as well as on the dielectric constant of the metal itself and the

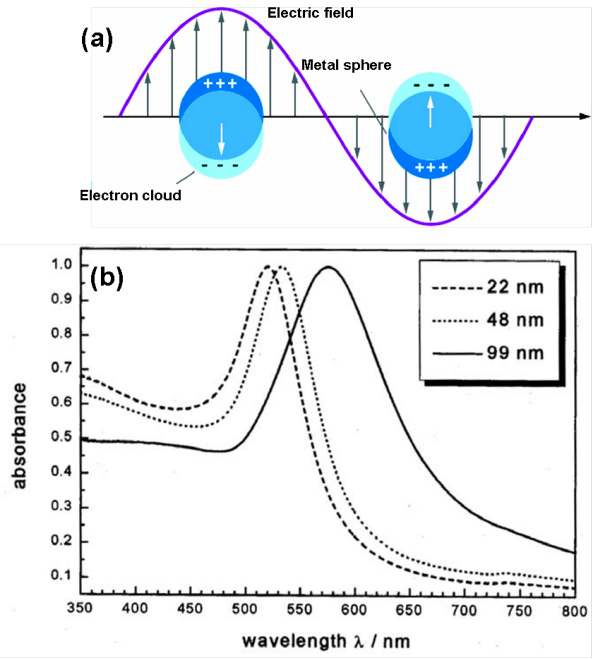

Figure 1.2.4: (a) Origin of the surface plasmon resonance in metal nanoparticles (b)Optical absorption spectra showing the plasmon bands of 22, 48 and 99 nm spherical gold nanoparticles(from [22]).

surrounding medium [22–25].

Figure 1.2.4b shows optical absorption spectra of 22, 48 and 99 nm spherical gold nanoparticles [22]. Because the spherical particles are completely symmetrical, there is only one dipolar plasmon resonance. By elongating a spherical particle in one dimension, however, it is possible to form another lower energy dipolar resonance mode in the longitudinal direction while the original transverse mode persists. Figure 1.2.5 shows optical absorption spectra of gold nanorods with different aspect ratios (AR) in comparison with the spectra for nanoparticles of different sizes [23]. The absorption spectra of the metal nanoparticles is also sensitive to the dielectric constant or refractive

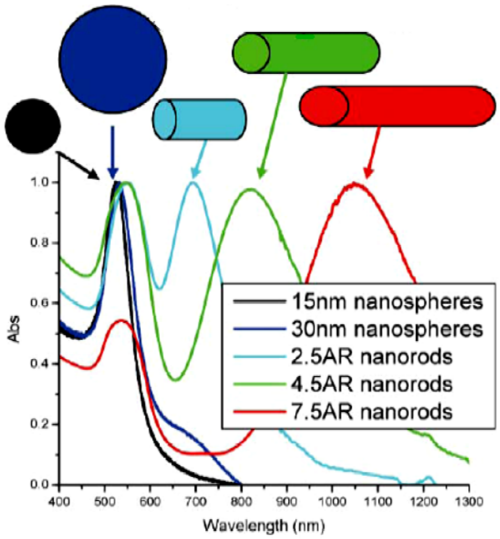

Figure 1.2.5: Optical absorption spectra of spherical gold nanoparticles and gold nanorods of different aspect ratio (AR) (from [23]).

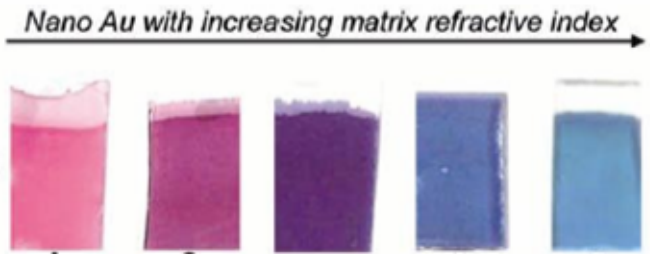

Figure 1.2.6: Tuning the plasmon absorption band of gold nanoparticles with refractive index of the medium (From [24]).

index of the surrounding. Figure 1.2.6 shows the shift in the plasmon band of the gold nanoparticles observed by embedding them in matrices of different refractive indices [24]. Thus, by simply controlling the physical dimensions or surroundings, one can generate gold nanostructures with absorption covering the entire visible and near IR regions of the optical spectrum.

In comparison to bulk solids, nanomaterials are unique in their huge surface-to-volume (S/V) ratio, typically, million-fold increase compared to bulk materials. For a typical nanoparticle containing a few hundred atoms, there are a significant number of surface atoms. These surface atoms tend to be unsaturated chemically or have different bonding environment compared to atoms in the interior and would thus have energy level different from those in the interior, thereby introducing electronic states within the bandgap, often called trap states. These surface states will serve to trap charge carriers and also alter associated optical properties and functionalities. Charge carrier trapping plays a critical role in the electron relaxation process of photoinduced carriers. Section 2 in the second part of this thesis presents a study of photoconduction and photoluminescence properties of ZnO nanoparticles with respect to the changes in the surface states upon annealing in an oxygen atmosphere for different temperatures as well as doping with Co and Mn. The very large surface-to-volume ratio also affects other properties of nanostructures such as chemical reactivity, thermodynamic and kinetic stability and interaction with the embedding environment *etc.*

Optical and other properties of semiconductor nanoparticles have been altered through the use of hybrid methodologies that produce core@shell, alloy and doped nanostructures. The principle behind doping is to tune the

bandgap as well as to introduce electronic states within the bandgap so as to create additional transitions and influence the property and functionality of the host material. Section 1 in the first part of this thesis presents studies of the changes in the band edge of ZnO nanoparticles doped with Mn^{2+}, Co^{2+} and Ni^{2+}.

Doping, the intentional introduction of impurities, is found to be difficult to achieve in some cases. For example, Mn can be incorporated into CdS and ZnS nanoparticles, but not into CdSe [26]. Doped luminescent semiconductor nanoparticles (*e.g.* ZnS:Cu and ZnS:Mn) are of strong interest for possible use in opto-electronics such as LEDs and lasers or as novel phosphors. Doping for n- and p-type conduction has been achieved in many semiconductor nanostructures. ZnO has n-type character, even in the absence of intentional doping. There are only few reports of successful p-doping of ZnO nanostructures [27]. Non-stoichiometry is said to be the origin of n-type character in ZnO, but the subject remains controversial. The defects are generally believed to ruin the optical properties by charge carrier trapping. But the n-type conductivity of ZnO with strong luminescence in the visible region makes it appropriate for phosphor applications in vacuum fluorescent displays and field emission displays [28]. The intense green emission from ZnO nanoparticles can be utilized in white light emitting diodes [29]. The nano-scale Indium composition fluctuations due to Indium aggregation or phase separation in InGaN quantum wells (Figure 1.2.7) play a key role in high-efficient green emitting LEDs [30, 31]. The indium clusters are able to act as local traps for migrating photon-emitting carriers and seem to boost the overall device performance. Second part of this thesis contains a study

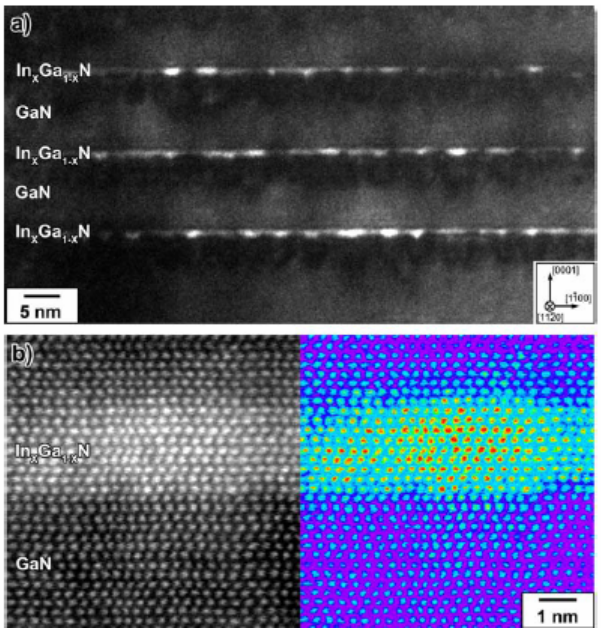

Figure 1.2.7: (a) Annular dark-field scanning transmission electron micrographs of InGaN quantum wells in the active LED region; (b) Z-contrast micrographs (left) in grey scale and (right) in false colour code showing Indium-rich quantum dot-like clusters with sizes in the range of 1-3 nm (From [30]).

of synthesis and optical properties of In doped GaN nanoparticles, where we observe the effect of In doping on the wavelength and broadness of the emission band.

In core@shell nanoparticles, the shell provides a physical barrier between the optically active core and the surrounding medium, thus making the nanoparticles less sensitive to environmental changes, surface chemistry, and photo-oxidation. The shell further provides an efficient passivation of the surface trap states, giving rise to a strongly enhanced fluorescence quantum yield (See Figure 1.2.3c). This effect is a fundamental prerequisite for the use of nanoparticles in applications such as biological labeling and light-emitting

devices, which rely on their emission properties [32]. The unique quantum dot structure with a composition gradient in the thick shells (See inset of Figure 1.2.8) as well as the uniform and high surface coverage in the test device due to the stable surface modification, leads to the high efficiency of CdSe@ZnS core@shell quantum dot based LEDs [33]. Figure 1.2.8 also shows images of CdSe@ZnS quantum dot structure obtained by compositionally sensitive imaging techniques utilizing the spherical aberration-corrected FEI Titan analytical electron microscope [34].

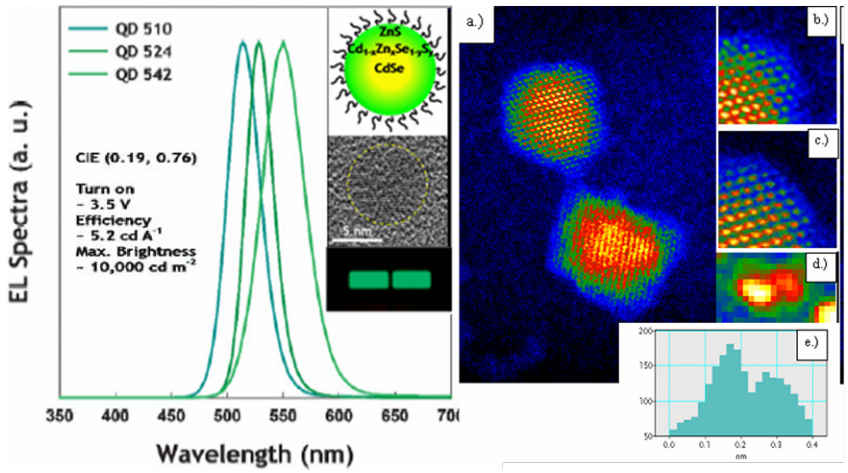

Figure 1.2.8: EL spectra of QLEDs based on different QDs (left) with the inset showing a schematic diagram of QD structure, TEM image of an actual QD and QLEDs emitting green light (From [33]). Annular dark-field scanning transmission electron microscope images of a CdSe@ZnS quantum dot (a, b and c on the right) showing individual atom-pair (d) with intensity trace (e) across the atom-pair (From [34]).

To take full advantage of the particle size effect, the particles must be separated and the best possible way of accomplishing this is to disperse the

particles in a matrix. Nanoparticles in matrices have interesting optical properties, due to the effects of quantum confinement as well as the surrounding medium. By embedding an optically functional phase into a processable transparent matrix material, the optical properties can be utilized in more technologically important forms such as films and fibers. Such composite materials have many interesting new optical properties and potential applications. The dispersion of metal particles into liquids or polymers leads to interesting absorption spectra that can be controlled by changing the metal used, the particle size, degree of dispersion, the polydispersity of the particle size and also the dielectric constant of the matrix as discussed earlier. This makes them potentially useful for applications in biological detection as well as in colored optical filters.

The changes in the emission spectra that occur after interaction of the target analyte and the ability to function as energy transfer donors in fluorescence resonance energy transfer (FRET) mechanisms are the basis of many of the semiconductor nanoparticle-based optical probes reported so far [35]. By incorporating semiconductor nanoparticles into polymer, glass or ceramic matrix materials, many of their interesting optical and related properties including absorption, emission and nonlinearity have been studied [36]. Part 6 of the thesis presents the optical properties of CdSe and ZnO nanoparticles embedded in a conducting polymer matrix, polyaniline.

The photonic bandgap materials are composed of array of nanoparticles with periodically packed structures [39]. For example, a peacock feather made up of an array of melanin rods connected by keratin as depicted in Figure 1.2.9 is a natural photonic crystal [12,38]. Opals are another example

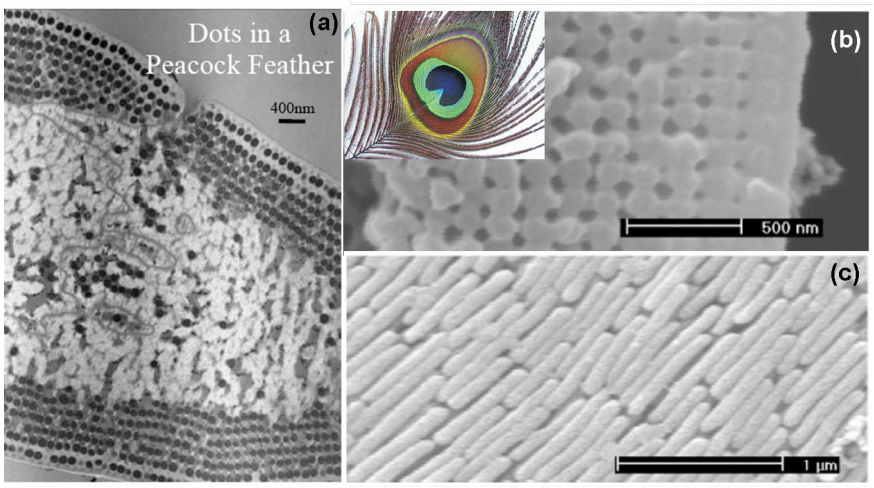

Figure 1.2.9: (a) Transmission electron microscope showing the nanostructures in a peacock feather (From [37]), Scanning electron microscope images of (b) Transverse cross section of the outer cortex layer of a barbule and (c) Longitudinal cross section of a barbule with the surface keratin layer removed (From [38]).

of this type of material in nature and they are precious gems composed of submicron sized silica spheres packed together and cemented with another slightly different silica. Periodic variation in the dielectric constant or refractive index is key to the unique photonic properties of these materials. In some case, semiconductor nanoparticles are introduced in the voids of the photonic bandgap materials to influence the gap and optical properties such as photoemission. For example, it was found that the emission lifetime of Mn^{2+} in Mn-doped ZnS nanophosphor is dependent on the refractive index of the photonic material [40]. Part 3 of the thesis presents the effect of varying the refractive index of the matrices on the emission bands of nanophosphors such as CdSe and YAG:Ce nanoparticles.

1.3 Applications

Nanomaterials offer many advantages over bulk materials, depending on the type of application. One of the advantages is the processibility over large areas, especially when combined with matrix materials such as polymers and glasses resulting in nanocomposite materials. The optical properties of nanomaterials have been exploited for many applications such as sensing and detection, optical imaging, biomedicine, environmental protection, light energy conversion and optoelectronics.

Both semiconductor and metal nanostructures have been used extensively for optical, chemical and biomedical detection by taking advantage of their unique optical properties. The detection scheme usually makes use of their absorption, scattering (*e.g.* PL and Raman) or other effects such as photothermal conversion. For example, ZnO nanoparticles have been suggested as potentially economical material for UV detectors, since it absorbs UV light corresponding to the bandgap [41]. Part 1, Section 2 of the thesis contains studies of UV photodetectors based on colloidal ZnO nanoparticles.

Semiconductor nanoparticles have been widely used replacing dye molecules as fluorescence labels in biomedical detection. In most cases, luminescence quenching or enhancement of nanoparticles is detected when they interact with the target analyte. One of the most commonly encountered techniques based on photoluminescence is FRET, which involves nonradiative transfer of energy from a donor molecule (or nanoparticle) to an acceptor molecule (or nanoparticle). Therefore, the signature of FRET is quenching of the

donor fluorescence followed by lower energy or longer wavelength fluorescence of the acceptor. FRET based on semiconductor nanoparticles often as donors and to a lesser degree as acceptors or both as donors and acceptors is reported [35].

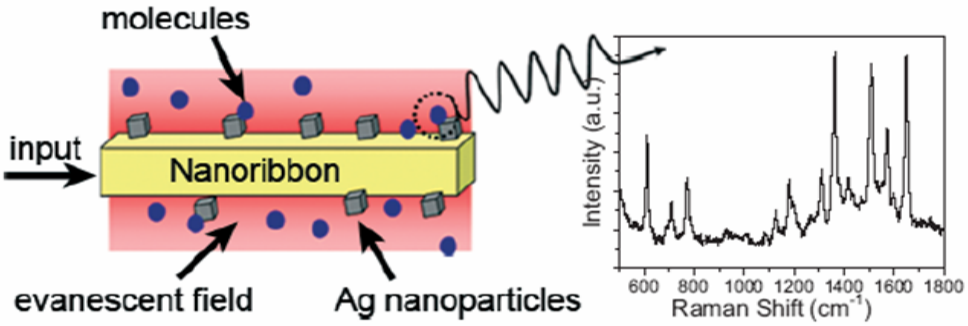

Figure 1.3.1: A cartoon of the nanoribbon evanescent wave SERS sensor. Analyte molecules in close proximity to a metal-decorated nanoribbon show amplified Raman scattering (from [42]).

Surface Plasmon Resonance (SPR) sensing is a commercially available optical detection technique based on the measurement of changes in the surface plasmon absorption band of a thin metal layer or metal nanostructures caused by interaction with a target analyte of interest [43]. Even small changes in adsorbate dielectric constant can have an observable effect on resonance wavelength. Another important application of metal nanostructures is surface enhanced Raman scattering (SERS). Normal Raman scattering, first discovered in 1928 [44], is a widely used spectroscopic technique for chemical analysis, detection and imaging. The major limitation of normal

Raman scattering is the very small signal or low quantum yield of scattering (on the order of 10^{-7}) [45]. SERS, discovered in the middle 1970s, has made Raman or SERS more popular for practical applications due to the combined advantages of molecular specificity and large signal [46]. SERS is based on the enhancement of Raman scattering of an analyte molecule near or on a roughened metal substrate surface. Figure 1.3.1 shows an example of a nanoribbon-based optical SERS sensor that takes advantage of the waveguiding property of the nanoribbon for improving the Raman signal [42]. Gold and silver metal nanoparticles have been used as labels for optical detection as well as substrates in SERS of biomolecules such as DNA and proteins [47, 48]. Part 5, Section 1 of this thesis presents the studies which show metallic ReO_3 nanoparticles to be SERS active.

The nanoparticles have been also used for imaging in cell biology and animal biology [49, 50]. Luminescent semiconductor nanoparticles have been used not only to label cellular structures and receptors, but also to track the path and fate of individual cells including stems cells. SPR and Raman scatering techniques based on metal nanoparticles are also developed for imaging applications. Other imaging techniques based on metal nanostructures include photothermal imaging and photoacoustic imaging.

Besides detection and imaging applications, some nanomaterials have also been explored as therapeutic agents, for drug delivery as well as in diagnotics and implants [51]. An interesting application is the use of nanomaterials as photosensitizer in a process called photodynamic therapy (PDT) [52]. PDT is a medical technique for cancer treatment that uses a combination of light,

photosensitizers and oxygen. Photothermal imaging can be extended to therapeutic treatment such as cancer cell destruction or ablation which is sometimes called photothermal ablation therapy. Metal nanoshells consisting of a dielectric core covered by a thin metallic shell which is typically gold, possess optical properties which can be designed to be favourable for biomedical imaging or therapeutic applications. Figure 1.3.2 shows the use of gold /silica nanoshells for photothermal ablation therapy [53].

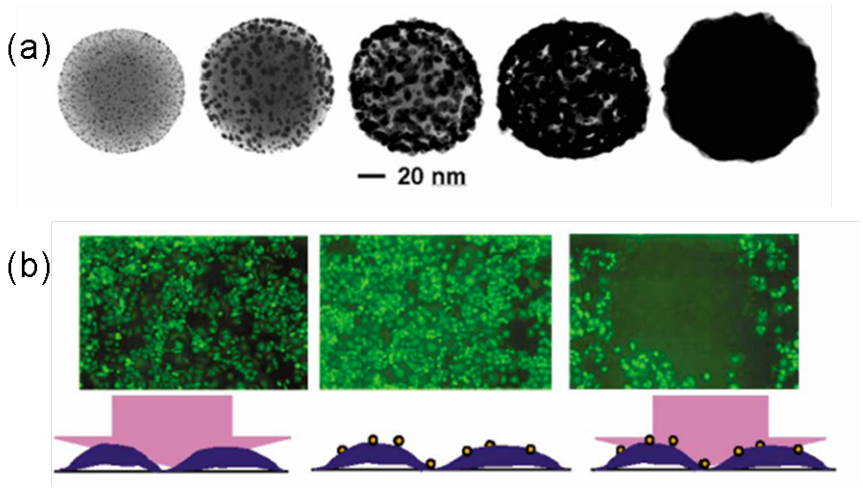

Figure 1.3.2: (a) Transmission electron microscope images of gold/silica nanoshells during shell growth and (b) Left: cells after exposure to laser only (no nanoshells). Middle: cells incubated with nanoshells but not exposed to laser light. Right: cell incubated with nanoshells after laser exposure. The dark circle seen in the image on the right corresponds to the region of cell death caused by exposure to laser light after incubation with nanoshells (from [53]).

Nanomaterials have played a critical role in many important chemical reactions as reactants, catalysts or photocatalysts. Their reactivities are often altered or enhanced due to size dependent changes in their redox potentials and high density of active surface states associated with a very large

surface-to-volume ratio. Photocatalytic oxidation of organic and biological molecules is of great interest for environmental applications, especially in the destruction of hazardous wastes or pollutants [54]. One of the most important areas of application of photocatalytic reactions is removal or destruction of contaminates in water [55]. Besides photocatalysis, nanoparticles can also directly participate in photochemical reactions. It has been demonstrated that photo-oxidation of some small molecules on semiconductor nanoparticles can lead to the formation of biologically important molecules such as amino acids, peptide oligomers and nucleic acids [56, 57].

Semiconductor nanoparticles of different size generate different colored filters, when coated on glass or quartz substrates [58]. Special type of filters can be constructed from so-called photonic crystals. Composites of nanosized metal particles in transparent dielectrics can be used as nonlinear optical materials in photonic devices for applications such as optical computing and real time holography [36]. The nanomaterials are also considered as diffractive components for other photonics applications such as sensors [59] and tunable gratings [60]. The optical coatings made of nanostructures as well as polymer nanocomposites also have been studied for possible use as antireflection coatings (ARCs) in solar cells [61]. Figure 1.3.3 shows a highly aligned ZnO nanorod array fabricated via low temperature aqueous solution deposition and its antireflection properties [62].

Increasing solar cell efficiency while maintaining a low production cost has been the primary objective of solar energy conversion. Nanomaterials can be employed to achieve improved performance of the solar cells via light

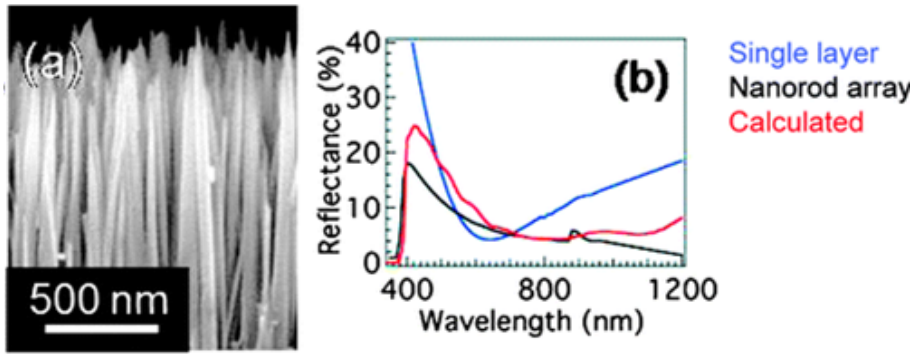

Figure 1.3.3: (a) Cross section SEM image of a highly tapered ZnO nanorod array. (b) Experimental and calculated reflectance spectra of ZnO nanorod array antireflection coatings along with that of a SiN single layer antireflection coating on Si solar cell (from [62]).

trapping techniques such as antireflection coatings. Recently, metallic nanostructures have been used to realize broad band absorption enhancement and improved photocarrier generation in thinfilm solar cells [63]. In section 2 of part 4, the effect of metallic ReO_3 nanoparticles on photocurrent generation in silicon solar cells have been presented. Likewise, Up-converting and down-converting phosphors in nanosizes also have great promise in increasing efficiency of Si solar cells.

Besides Si, other semiconductor materials such as CdSe, CdTe, CuInSe and GaAs, have been used for solar cells in bulk crystalline, thin film or polycrystalline forms [64]. Solar cells based on semiconductor nanomaterials have been investigated as alternatives, especially in terms of reducing the cost and large area fabrication on flexible substrates. Two general types

of nanomaterial-based solar cells are the solar cells based on semiconductor nanoparticles [65] and dye-sensitized solar cells [66]. The types of solar cells that capitalize salient properties of semiconductor nanoparticles are metal-semiconductor or Schottky junction photovoltaic cell, semiconductor nanostructure-polymer solar cell and semiconductor-semiconductor system including quantum dot sensitized solar cell (See Figure 1.3.4). Semiconductor nanoparticles (*e.g.* PbSe) open up new ways to harvest solar energy by utilizing hot electrons or by generating multiple charge carriers with a single photon [67, 68].

In a dye-sensitized solar cell, dye molecules are adsorbed onto the surface of nanostructured material such as TiO_2 or ZnO. The high surface to volume ratio of these nanoparticles improves the charge collection from the dye molecules and hence the efficiency of the solar cells. Recently, there has been increasing research effort to use inorganic semiconductor nanoparticles as sensitizers for solar cell applications. In these quantum dot sensitized solar cells, the semiconductor nanoparticles replace organic dye molecule and potential advantages include thermal stability and color tunability by controlling nanoparticle size and shape.

Limitation with nanoparticle based solar cells is the poor transport properties due to grain boundaries or trap states that significantly limit their conversion efficiency. Commercialization of large scale solar cells based on nanostructure architecture has yet to be realized [69]. Similar to photovoltaics, nanomaterials are also used for the design of other solar energy conversion devices for artificial photosynthesis and for producing fuels such as hydrogen by semiconductor assisted photocatalysis [70]. Nanoparticles

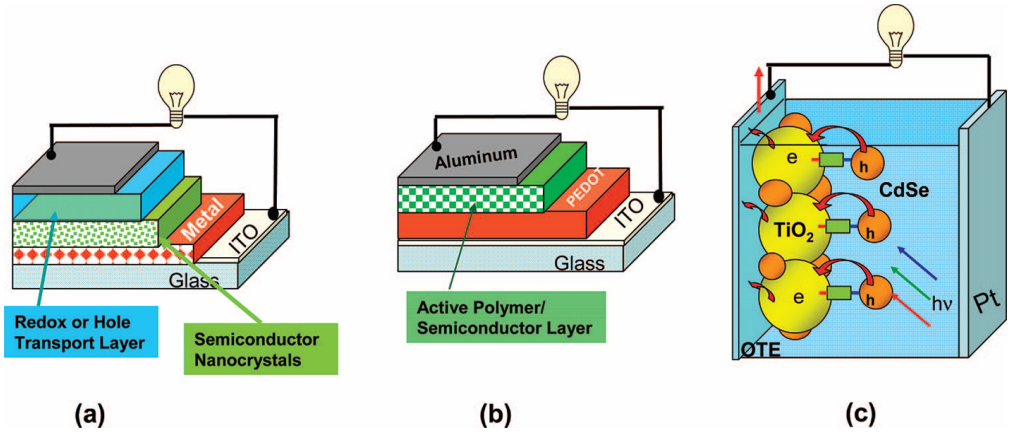

Figure 1.3.4: Schematic diagram showing the strategies to develop semiconductor nanoparticle based solar cells: (a) metal-semiconductor junction, (b) polymer-semiconductor and (c) semiconductor-semiconductor systems (from [69]).

offer some potential advantages for photoelectrodes in photoelectrochemical cells, including large surface area and fast diffusion.

Another area of application of nanomaterials that has attracted considerable interest is lasers. It is possible to build lasers with different wavelengths by simply changing the size of the nanostructures. This has been demonstrated mostly for quantum dots self-assembled in clean environments based on physical methods such as molecular beam epitaxy (MBE)or metal organic chemical vapor deposition (MOCVD) [71, 72]. Nanoparticles such as TiO_2 have been used to enhance stimulated emission for conjugated polymers based on multiple reflection effect [73]. The lasing action observed in colloidal nanoparticles of CdSe [74] demonstrates the feasibility of quantum dot lasers based on solution processing, when the nanoparticles are clean and has little surface defects. Room-temperature ultraviolet lasing in ZnO

nanowire arrays has been demonstrated by measuring the excitation density-dependent emission with excitation from the fourth harmonic of a Nd:YAG laser [75]. Light emission was collected in the direction normal to the end surface plane (along the c-axis) of the nanowires and lasing was observed in the absence of any fabricated mirrors with increasing pump power as shown in Figure 1.3.5.

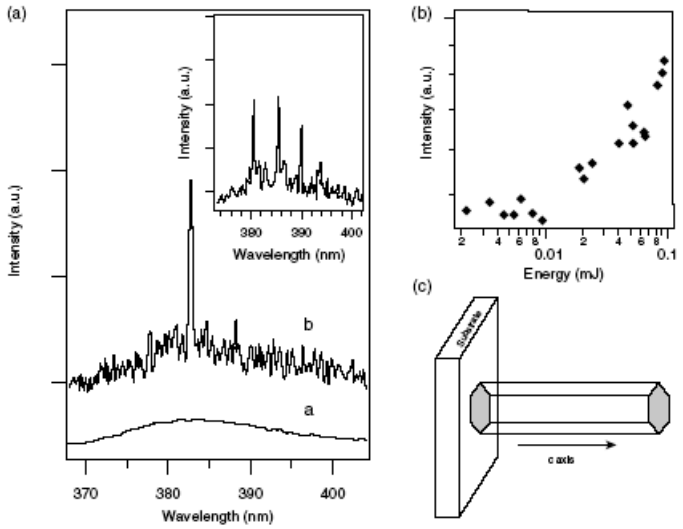

Figure 1.3.5: ((a) Emission spectra from nanowire arrays below (line a) and above (line b and inset) the lasing threshold, (b) Integrated emission intensity from nanowires as a function of optical pumping energy intensity and (c) Schematic illustration of a nanowire as a resonance cavity with two naturally faceted hexagonal end faces acting as reflecting mirrors (from [75]).

Solid state lighting is an area of fast growing interest. The future of high-efficiency low cost artificial lighting is believed to be in the use light emitting diodes. Nanostructuring currently plays a key role in the high efficiency performance of Group III-nitride heterostructure LEDs [76]. The nanomaterials such as TiO_2 or SiO_2 nanoparticles are used to enhance light

emission of LED devices with other materials, *e.g.* conjugated polymers, as the active media [77]. Highly luminescent semiconducting nanoparticles are used as the active materials for light generation directly [78–80]. Figure 1.3.6 shows the device structure and emission spectra of a LED device using the hybrid layer containing red, green and blue emitting CdSe@ZnS quantum dots as the active layer [80]. Another solid state lighting technology that is already compatible with low cost manufacturing is alternating current (AC) powder or thinfilm electroluminescence. Nanoparticle systems exhibiting AC electroluminescence also have been reported recently [81–83].

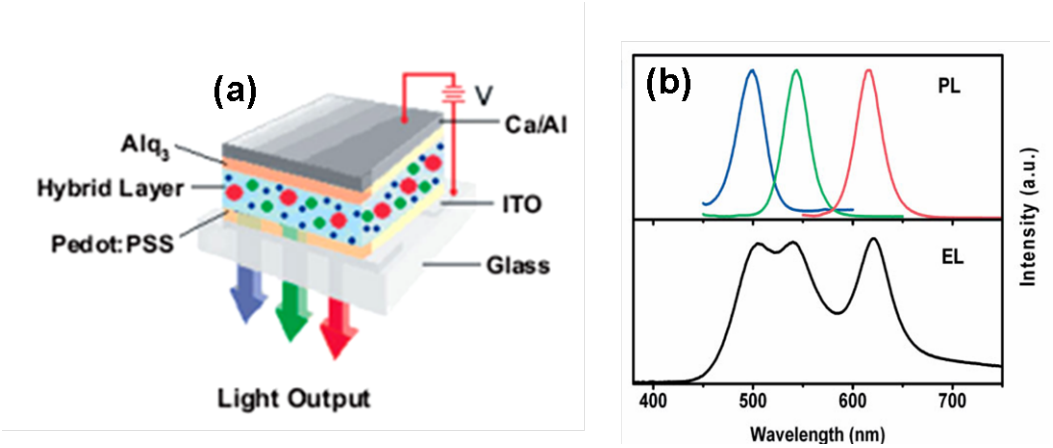

Figure 1.3.6: (a) The structure of the ternary quantum dot LED device using hybrid of red, green, and blue emitting nanoparticles as active layer and (b) PL and EL spectra of the LED device (from [80]).

Since the mobility of the charge carriers is usually much lower than in bulk single crystals, charge transport is one of the major limitations in efficient light generation in such devices. Nanocomposites and new nanostructures such as nanowires, nanorods and nanobelts may provide some interesting alternatives with better transport properties than nanoparticles. Along with

the applications in lasers and LEDs, the luminescent nanomaterials are also used as novel phosphors for solid state lighting [84]. Examples are nanoparticles of Mn or Cu doped ZnS and rare earth ion doped $Y_3Al_5O_{12}$, Y_2O_3, ZnO, GaN *etc.* The phosphors based on luminescent nanoparticles and their nanocomposites are employed for the down-conversion of blue or UV light emission from LEDs to generate white light. Part 2, Section 2 of the thesis contains studies of white light emitting phosphors based on nanocomposites of GaN nanoparticles with other nanophosphors and conjugated polymers.

References

[1] R. P. Feynman, *Eng. Sci.* **23**, 22 (1960).

[2] I. Freestone, N. Meeks, M. Sax, C. Higgitt, *Gold Bull.* **40**, 270 (2007).

[3] R. D. Tweney, *Perspectives on Science* **14**, 97 (2006).

[4] M. Faraday, *Phil. Trans. R. Soc. London* **147**, 145 (1857).

[5] E. K. Drexler, *Proc. Natl. Acad. Sci.* **78**, 5275 (1981).

[6] E. K. Drexler, *Engines of Creation:The Coming Era of Nanotechnology* (Anchor Press/Doubleday, Garden City, New York, 1986).

[7] G. Binnig, H. Rohrer, *Rev Mod. Phys.* **59**, 615 (1987).

[8] C. N. R. Rao, A. Mueller, A. K. Cheetham, *The Chemistry of Nanomaterials: Synthesis, Properties and Applications* (Wiley-VCH, Weinheim, 2004).

[9] C. N. R. Rao, S. R. C. Vivekchand, K. Biswas, A. Govindaraj, *Dalton Transactions* **34**, 3728 (2007).

[10] C. N. R. Rao, A. Mueller, A. K. Cheetham, *Nanomaterials Chemistry: Recent Developments* (Wiley-VCH, Weinheim, 2007).

[11] J. Z. Zhang, *Optical Properties and Spectroscopy of Nanomaterials* (World Scientific: Hackensack, NJ., 2009).

[12] M. Srinivasarao, *Chem. Rev.* **99**, 1935 (1999).

[13] C. N. R. Rao, G. U. Kulkarni, P. J. Thomas, P. P. Edwards, *Chem-Euro J.* **8**, 29 (2002).

[14] Z. W. Pan, Z. R. Dai, Z. L. Wang, *Science* **291**, 1947 (2001).

[15] X. Y. Kong, Y. Ding, R. Yang, Z. L. Wang, *Science* **303**, 1348 (2004).

[16] J. Hu, L. S. Li, W. Yang, L. Manna, L. W. Wang, A. P. Alivisatos, *Science* **292**, 2060 (2001).

[17] S. V. Goponenko, *Optical properties of Semiconductor Nanocrystals* (Cambridge University Press, New York, 1998).

[18] C. B. Murray, D. J. Noms, M. G. Bawendi, *J. Am. Chem. Soc.* **115**, 8706 (1993).

[19] See website:*http://nanocluster.mit.edu/research.php.*

[20] X. Peng, L. Manna, W. Yang, J. Wickham, E. Scher, A. Kadavanich, A. P. Alivisatos, *Nature* **404**, 59 (2000).

[21] G. Mie, *Ann. Phys.* **25**, 329 (1908).

[22] S. Link, M. A. El-Sayed, *Int. Rev. Phys. Chem.* **19**, 409 (2000).

[23] S. Eustis, M. A. El-Sayed, *Chem. Soc. Rev.* **35**, 209 (2006).

[24] S. K. Medda, S. De, G. De, *J.Mater.Chem.* **15**, 3278 (2005).

[25] H. Chen, X. Kou, Z. Yang, W. Ni, J. Wang, *Langmuir* **24**, 5233 (2008).

[26] S. Erwin, L. Zu, M. Haftel, A. L. Efros, T. A. Kennedy, D. J. Norris, *Nature* **436**, 91 (2005).

[27] G. D. Yuan, W. J. Zhang, J. S. Jie, X. Fan, J. A. Zapien, Y. H. Leung, L. B. Luo, P. F. Wang, C. S. Lee, S. T. Lee, *Nano Lett.* **8**, 2591 (2008).

[28] A. Janotti, C. G. V. de Walle, *Rep. Prog. Phys.* **72**, 126501 (2009).

[29] M. Willander, O. Nur, N. Bano, K. Sultana, *New J. Phys.* **11**, 125020 (2009).

[30] J. R. Jinschek, R. Erni, N. F. Gardner, A. Y. Kim, C. Kisielowski, *Solid State Commun.* **137**, 230 (2006).

[31] C. C. Yang, S.-W. Fengb, Y.-S. Linc, Y.-C. Cheng, C.-C. Liaob, C.-Y. Tsai, K.-J. Mac, J.-I. Chyie, *Proc. SPIE* **4280**, 20 (2001).

[32] P. Reiss, M. Protiere, L. Li, *Small* **5**, 154 (2009).

[33] W. K. Bae, J. Kwak, J. W. Park, K. Char, C. Lee, S. Lee, *Adv. Mater.* **21**, 1690 (2009).

[34] See website: *http://www.nist.gov/cstl/surface/837-02-herzing-2008-titan-nanoscale.cfm*, Surface and Microanalysis Science Division, CSTL, NIST, US; Last updated: June 9, 2009; Last accessed: April 22, 2010.

[35] J. M. Costa-Fernandez, *Anal. Bioanal. Chem.* **384**, 37 (2006).

[36] P. M. Ajayan, L. S. Schadler, P. V. Braun, *Nanocomposite Science and Technology* (Wiley-VCH, Weinheim, 2003).

[37] See website: *http://www.uark.edu/depts/physics/faculty/index.php?name=salamo*, Department of Physics, University of Arkansas; Last Updated: May 13, 2009; Last accessed: April 22, 2010.

[38] J. Zi, X. Yu, Y. Li, X. Hu, C. Xu, X. Wang, X. Liu, R. Fu, *Proc. Natl. Acad. Sci.* **100**, 12577 (2003).

[39] X. Zhang, B. Sun, R. H. Friend, H. Guo, D. Nau, H. Giessen, *Nano Lett.* **6**, 651 (2006).

[40] J. Zhou, Y. Zhou, S. Buddhudu, S. L. Ng, Y. L. Lam, C. H. Kam, *Appl. Phys. Lett.* **76**, 3513 (2000).

[41] Y. Jin, J. Wang, B. Sun, J. C. Blakesley, N. C. Greenham, *Nano Lett.* **8**, 1649 (2008).

[42] D. J. Sirbuly, A. Tao, M. Law, R. Fan, P. Yang, *Adv. Mater.* **19**, 61 (2007).

[43] J. Homola, S. S. Yee, G. Gauglitz, *Sensors and Actuators B* **54**, 3 (1999).

[44] C. V. Raman, K. S. Krishnan, *Nature* **121**, 501 (1928).

[45] J. R. Ferraro, K. Nakamoto, *Introductory Raman Spectroscopy* (Academic Press, Boston, 1994).

[46] M. Fleischmann, P. J. Hendra, A. J. McQuillan, *Chem.Phys.Lett.* **26**, 163 (1974).

[47] M. E. Stewart, C. R. Anderton, L. B. Thompson, J. Maria, S. K. Gray, J. A. Rogers, R. G. Nuzzo, *Chem. Rev.* **108**, 494 (2008).

[48] P. K. Jain, X. Huang, I. H. Sayed, M. A. Sayed, *Plasmonics* **2**, 107 (2007).

[49] P. Sharma, S. Browna, G. Walterc, S. Santrad, B. Moudgil, *Adv. Colloid Interface Sci.* **123-126**, 471 (2006).

[50] N. Sounderya, Y. Zhang, *Recent Patents on Biomedical Engineering* **1**, 34 (2008).

[51] V. Wagner, A. Dullaart, A.-K. Bock, A. Zweck, *Nature Biotechnol.* **24**, 1211 (2006).

[52] J. P. Celli, B. Q. Spring, I. Rizvi, C. L. Evans, K. S. Samkoe, S. Verma, B. W. Pogue, T. Hasan, *Chem. Rev.* (2010).

[53] C. Loo, A. Lin, L. Hirsch, M. H. Lee, J. Barton, N. Halas, J. West, R. Drezek, *Technol. Cancer Res. Treat.* **3**, 33 (2004).

[54] M. R. Hoffmann, S. T. Martin, W. Y. Choi, D. W. Bahnemann, *Chem. Rev.* **95**, 69 (1995).

[55] N. Serpone, R. F. Khairutdinov, *Semiconductor Nanoclusters-Physical, Chemical and Catalytic Aspects* (Elsevier, New York, 1997).

[56] W. W. Dunn, Y. Aikawa, A. J. Bardm, *J. Am. Chem. Soc.* **103**, 6893 (1981).

[57] H. Harada, T. Ueda, T. Sakata, *J. Phys. Chem.* **93**, 1542 (1989).

[58] M. C. Tsai, T. L. Tsai, C. T. Lin, R. J. Chung, H. S. Sheu, H. T. Chiu, C. Y. Lee, *J. Phys. Chem. C* **112**, 2697 (2008).

[59] J. H. Holtz, S. A. Asher, *Nature* **389**, 829 (1997).

[60] J. M. Weissman, H. B. Sunkara, A. S. Tse, S. A. Asher, *Science* **274**, 959 (1996).

[61] K. C. Krogman, T. Druffel, M. K. Sunkara, *Nanotechnology* **16**, S338 (2005).

[62] Y.-J. Lee, D. S. Ruby, D. W. Peters, B. B. McKenzie, J. W. P. Hsu, *Nano Lett.* **8**, 1501 (2008).

[63] K. R. Catchpole, A. Polman, *Opt. Express* **16**, 21793 (2008).

[64] T. Markvart, L. Castaner, *Practical Handbook of Photovoltaics: Fundamentals and Applications* (Elsevier, Oxford, UK, 2003).

[65] N. C. Greenham, X. G. Peng, A. P. Alivisatos, *Phys. Rev. B-Condens. Matter* **54**, 17628 (1996).

[66] B. Oregan, M. Gratzel, *Nature* **353**, 737 (1991).

[67] R. T. Ross, A. J. Nozik, *J. Appl. Phys.* **53**, 3813 (1982).

[68] R. D. Schaller, V. I. Klimov, *Phys. Rev. Lett.* **92**, 186601 (2004).

[69] P. V. Kamat, *J. Phys. Chem. C* **112**, 18737 (2008).

[70] P. V. Kamat, *J. Phys. Chem. C* **111**, 2834 (2007).

[71] K. Hinzer, J. Lapointe, Y. Feng, A. Delage, S. Fafard, A. J. SpringThorpe, E. M. Griswold, *J. Appl. Phys.* **87**, 1496 (2000).

[72] S. Tanaka, H. Hirayama, Y. Aoyagi, Y. Narukawa, Y. Kawakami, S. Fujita, *Appl. Phys. Lett.* **71**, 1299 (1997).

[73] F. Hide, B. J. Schwartz, M. A. Diazgarcia, A. J. Heeger, *Chem. Phys. Lett.* **256**, 424 (1996).

[74] V. I. Klimov, A. A. Mikhailovsky, S. Xu, A. Malko, J. A. Hollingsworth, C. A. Leatherdale, H. J. Eisler, M. G. Bawendi, *Science* **290**, 314 (2000).

[75] M. H. Huang, S. Mao, H. Feick, H. Q. Yan, Y. Y. Wu, H. Kind, E. Weber, R. Russo, P. D. Yang, *Science* **292**, 1897 (2001).

[76] E. B. Stokes, A. D. Stiff-Roberts, C. T. Dameron, *Electrochem. Soc. Interface* **15**, 23 (2006).

[77] S. A. Carter, J. C. Scott, P. J. Brock, *Appl. Phys. Lett.* **71**, 1145 (1997).

[78] V. L. Colvin, M. C. Schlamp, A. P. Alivisatos, *Nature* **370**, 354 (1994).

[79] J. L. Zhao, J. Y. Zhang, C. Y. Jiang, J. Bohnenberger, T. Basche, A. Mews, *J. Appl. Phys.* **96**, 3206 (2004).

[80] Y. Li, A. Rizzo, R. Cingolani, G. Gigli, *Adv.Mater.* **18**, 2545 (2006).

[81] K. Manzoor, S. R. Vadera, N. Kumar, T. R. N. Kutty, *Appl. Phys. Lett.* **84**, 284 (2004).

[82] K. Manzoor, V. Aditya, S. R. Vadera, N. Kumar, T. R. N. Kutty, *Solid State Commun.* **135**, 16 (2005).

[83] V. Wood, J. E. Halpert, M. J. Panzer, M. G. Bawendi, V. Bulovic, *Nano Lett.* **9**, 2367 (2009).

[84] H. Chander, *Mater.Sci.Eng.Rep.* **49**, 113 (2005).

Part 2

Investigations of Zinc Oxide Nanoparticles

Summary

ZnO nanoparticles doped with Mn^{2+}, Co^{2+} and Ni^{2+} have been prepared by the decomposition of acetate solid solutions. The magnetic properties of Mn^{2+} doped ZnO samples prepared by decomposition of acetate solid solution in argon atmosphere were studied. All the doped ZnO samples failed to show ferromagnetism. Electronic absorption spectroscopy has been used to measure the bandgaps of the doped ZnO samples and the variation of the bandgap with dopant concentration has been examined. The bandgap of Mn^{2+} doped ZnO showed an initial decrease followed by a linear increase while in the case of Co^{2+} and Ni^{2+} doped ZnO, there was a progressive decrease of bandgap with dopant concentration.

Papers based on these studies have appeared in Solid State Communications (2005), (2009) and Nanotechnolgy (2010).

Photoluminescence and photoconductivity of thin films of colloidal ZnO nanoparticles have been investigated by annealing them in an oxygen atmosphere at different temperatures. The changes in the defect-related emission and photoconducting properties with the annealing temperature have been examined in detail. The samples annealed at low temperatures showed better photocurrent to dark current contrast ratio with faster response and decay. The decreased contrast ratio for high temperature annealed samples acompanied by decrease in the intensity of defect related photoluminescence established the role of defects in the photoconductivity mechanism.

The effect of graphene on the photoconductivity response of ZnO nanoparticles in ZnO - graphene mixed system has been observed. The time resolved photocurrent studies showed that the photoresponse of the mixed system was faster, with small amount (< 0.5 wt %) of graphene added to ZnO nanoparticles. The photoconductivity of the mixed system decreased with the gradual increase in the graphene content. With the addition of 0.5 wt% of graphene, ZnO nanoparticles showed high conductivity and no sensitivity to UV light illumination.

2.1 Studies of transition metal ion doped ZnO nanoparticles

2.1.1 Introduction

Zinc oxide is a II-VI semiconductor, having the wurtzite structure (Figure 2.1.1) with wide direct band gap (∼3.3 eV). ZnO is therefore a candidate for optoelectronic applications in the short wavelength range. In fact, the high exciton binding energy in ZnO (about 60 meV) would allow for excitonic transitions even at room temperature, which could mean higher radiative recombination efficiency for spontaneous emission as well as a lower threshold voltage for laser emission. ZnO is now being considered as a potential material for a wide range of applications such as piezoelectric, opto-electronic and luminescent devices as well as chemical sensors. Extensive studies have been carried out to modify the properties of ZnO for different applications [1]. Doping with transitional metal elements leads to many interesting properties of ZnO.

Currently, much experimental and theoretical research is focused on dilute magnetic semiconductors (DMS) based on ZnO doped with transition metal ions such as Mn and Co, since the predicted room temperature ferromagnetism in the DMS may be useful in spintronics. The ferromagnetism in Mn and Co doped ZnO is not established and there are many contradictory experimental observations [2]. Room temperature ferromagnetism has been reported in thin films and bulk samples of Mn substituted ZnO by few workers [3, 4], but several studies on well-characterized bulk samples of ZnO

substituted with Mn did not show collective magnetism [5]. As per the previous studies carried out in our lab, Mn and Co doped ZnO samples with 2% and 6% dopant concentrations prepared by decomposition of acetate solid solutions in air, failed to show ferromagnetism [6]. This method gives excellent oxide solid solutions, wherein the dopant ions are substitutionally present in the host crystal lattice.

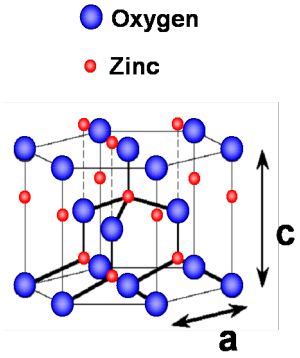

Figure 2.1.1: Structure of ZnO.

It is strongly believed that the defects in dilute magnetic semiconductor materials play a critical role in inducing ferromagnetism [7,8]. Chen *et.al.* [9] observed that the magnetic properties of bulk Mn doped ZnO samples prepared by solid state reaction are dependent on the processing conditions such as sintering temperature and atmosphere. They observed ferromagnetic interaction in the samples sintered in Ar atmosphere below 700^{o}C and found that ferromagnetism disappeared when samples were sintered in air. This motivated us to examine the effect of Ar atmosphere on the magnetic properties of our samples. We have prepared the Mn doped ZnO samples with 2% and 4 % dopant concentrations by decomposing the acetate solid solutions

in the presence of Ar gas and studied their magnetic properties.

However, the ternary nature of the DMS provides a possibility of tuning band gap by varying the composition of the material. The doping can also induce intermediate electronic levels to create gaps of different sizes. It has been proposed that DMS materials with ferromagnetic impurities may serve to overcome the non-radiative recombination in high efficiency solar cells based on the intermediate level semiconductor (ILSC) concept, with impurity induced intermediate levels [10]. Thus, doping of ZnO with transition elements such as Mn, Co and Ni offers a viable means of tuning the band parameters. A linear variation in the bandgap with composition is expected on the basis of the virtual crystal approximation (VCA). DMS materials are known to show a deviation from the linear dependence in the form of band gap bowing as in ZnMnSe and CdMnS [11,12]. The observed dip in the band gap has been theoretically explained as a manifestation of strong exchange interaction present between d electrons of Mn, and the s and p electrons of the host matrix. This strong exchange interaction between d electrons of the magnetic transition metal ions and the sp carriers is a most distinctive feature of DMS. Although the exchange interaction is especially important in the presence of an external magnetic field H, in certain cases it can manifest at H = 0. A similar effect of sp-d exchange interaction on the band gap has been reported in Mn doped ZnO from the previous studies.

Fukumura *et al.* [4] and Jung *et al.* [13] report an overall blue-shift in the band gap with increase in Mn concentration in thin epitaxial films of Mn doped ZnO. The observations of Fukumura *et al.* show an initial decrease of band gap for small concentrations of Mn, followed by an increase. This

non-monotonic variation of band gap is more pronounced in Mn-doped ZnO nanocrystals studied by Viswanatha *et al.* [14]. The increase in the band gap is as expected from VCA due to the higher band gap energy of the MnO (4.2 eV). The decrease in band gap for low concentrations of Mn is attributed to the sp-d exchange interactions. Co doped ZnO thin films show a decrease in band gap with increasing Co concentration [15], and a similar behavior is found in polycrystalline samples prepared hydrothermally by Bouloudenine *et al.* [16]. This red shift is explained as mainly due to the sp-d exchange interactions between the band electrons and the localized d electrons of cobalt ions substituting zinc ions. A decrease in the band gap of ZnO thin films due to nickel doping was reported by Shimono *et al.* [17].

We have investigated the optical band gap variations in $Zn_{1-x}Mn_xO$, $Zn_{1-x}Co_xO$ and $Zn_{1-x}Ni_xO$ (0.0 <x>0.1) samples, prepared by the decomposition of the acetate solid solutions. We have measured the band edges of the doped ZnO samples from the absorption spectra and compared the results with the literature.

2.1.2 Experimental details

Mn doped ZnO samples with 2% and 4% Mn were prepared starting from zinc acetate [$CH_3(COO)_2Zn.2H_2O$] and manganese acetate [$CH_3(COO)_2Mn.4H_2O$] taken in required molar ratios and dissolved in 20 ml of distilled water to get a clear solution. The solution was kept at 100^oC ($\sim$10 hr) for drying. The powder so obtained was heated in the purified argon gas at 600^oC for 3 hours to get polycrystalline powder samples of Mn doped ZnO. Similarly, $Zn_{1-x}Mn_xO$ samples with x= 0.01, 0.03, 0.05, 0.07 and 0.10 were prepared

by heating the respective solid solution of zinc acetate and manganese acetate in air. In the case of Co doped ZnO, zinc acetate and cobalt acetate [$CH_3(COO)_2Co.4H_2O$] were taken in the respective molar ratios (corresponding to 1, 3, 5, 7 and 10% Co) and dissolved in 20 ml of distilled water to get a clear solution. The solution was dried at 100 ^oC overnight and the resulting powder heated in air at 500 ^oC for 3 hours. The same procedure was followed for the preparation of 1% , 3%, and 5% Ni doped ZnO starting with nickel acetate [$CH_3(COO)_2Ni.4H_2O$]. X-ray diffraction (XRD) patterns of the samples were recorded using a X-ray diffractometer (Seifert). The chemical compositions of the samples were verified using an Oxford Energy Dispersive X-ray (EDX) analyzer attached with a Leica S-440i Scanning Electron Microscope (SEM). The particle size and morphology were studied by Field Emission Scanning Electron Microscopy (FESEM). Magnetic properties were measured using a SQUID magnetometer (Quantum Design MPMS). Room temperature optical absorption spectra were recorded in the 2000 - 200 nm wavelength range using a Perkin Elmer Lambda 900 UV/VIS/NIR spectrophotometer equipped with diffuse reflectance accessory.

2.1.3 Results and discussion

The XRD patterns of $Zn_{1-x}Mn_xO$, $Zn_{1-x}Co_xO$, and $Zn_{1-x}Ni_xO$ samples (Figures 2.1.2 and 2.1.3) showed that they had the wurtzite structure of ZnO (JCPDS file: 36-1451). A slight increase in the cell parameters is observed in the case of Mn doped ZnO, but there is little change in Co and Ni doped ZnO samples. The $Zn_{1-x}Mn_xO$ samples with $x \leq 0.07$ show only the peaks corresponding to ZnO giving no evidence of impurity phases. Samples with

x > 0.07, however, showed additional peaks in the XRD patterns due to the formation of $ZnMn_2O_4$. $Zn_{1-x}Co_xO$ samples also show a similar behav-

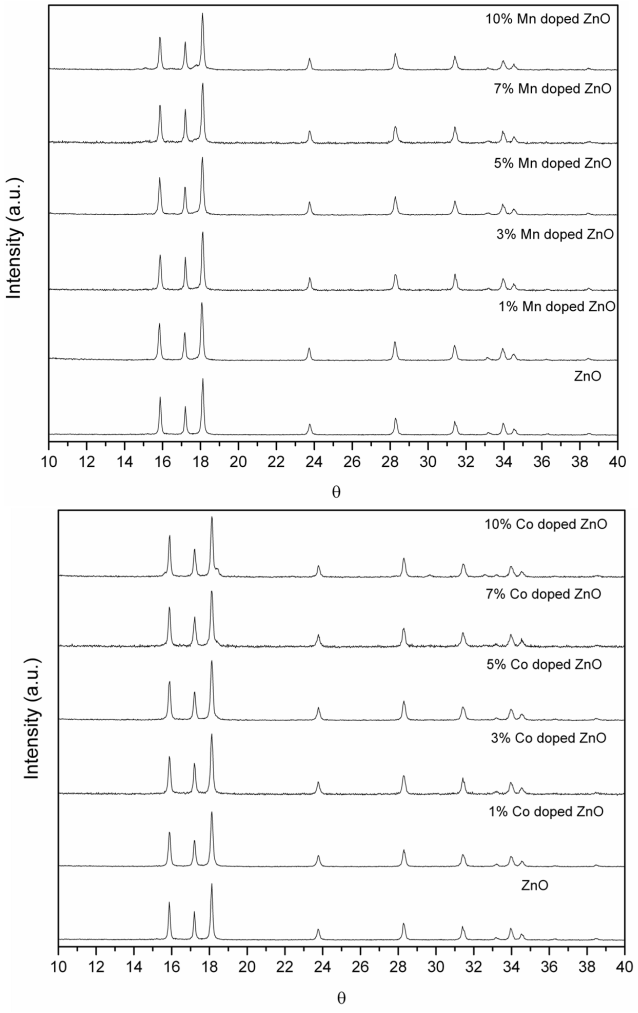

Figure 2.1.2: XRD patterns of Mn and Co doped ZnO samples.

ior with additional peaks for samples with x > 0.07, due to $ZnCo_2O_4$ and Co_3O_4. In the case of Ni doped ZnO, additional peaks corresponding to NiO were seen when x > 0.05. EDX analysis confirmed the percentages of the Mn, Co, and Ni in the respective samples to be close to the nominal values

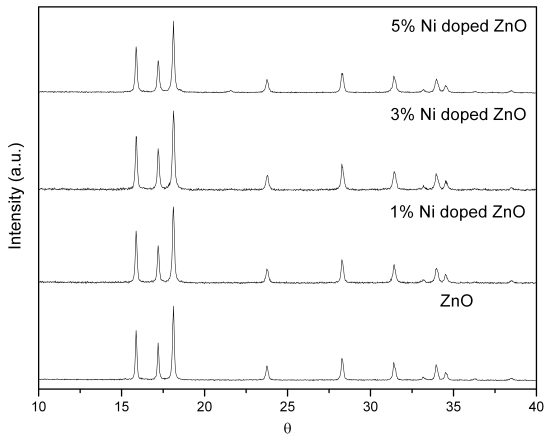

Figure 2.1.3: XRD patterns of Ni doped ZnO samples.

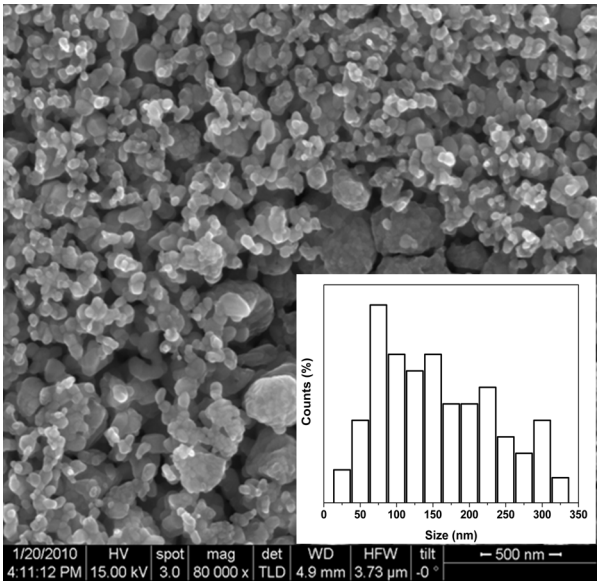

Figure 2.1.4: A typical FESEM image of doped ZnO samples showing the size distribution histogram as an inset.

used for the preparations. FESEM image of the doped ZnO samples (Figure 2.1.4) showed that they consist of particles of 50-200 nm diameter. The

temperature variation of the magnetic susceptibility for the 2% and 4% Mn-doped samples at 10 kOe (Figure 2.1.5) shows the paramagnetic behaviour, following the Curie−Weiss law.

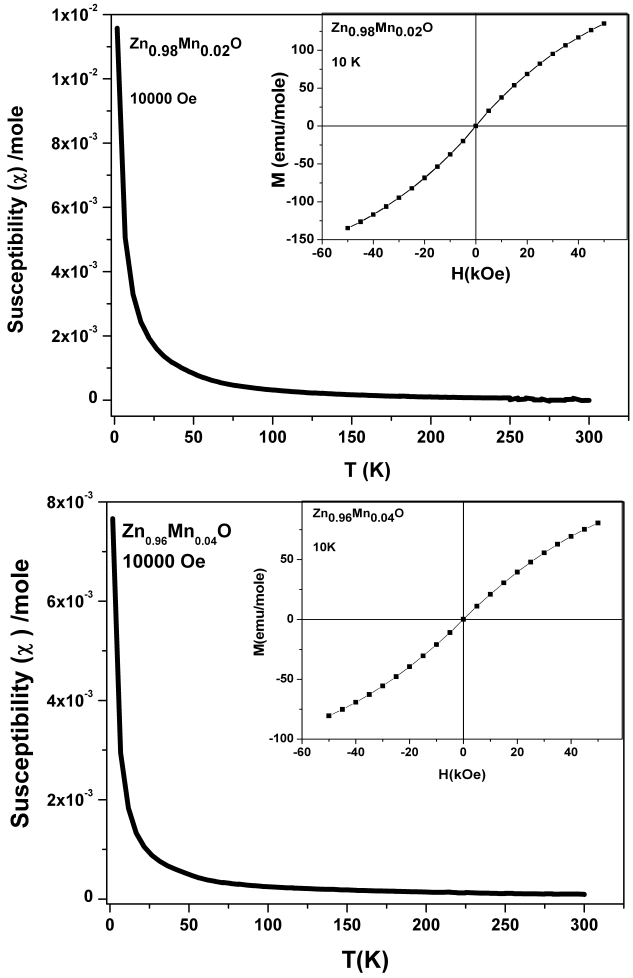

Figure 2.1.5: Magnetic susceptibility versus temperature plots for 2% and 4% Mn doped ZnO samples prepared in argon atmosphere.Insets show M vs H plots for the samples at 10K.

Furthermore, we do not observe any magnetic hysteresis down to 10 K in the M vs H curves proving the absence of ferro-magnetism (Insets in

Figure 2.1.5). Thus, the annealing atmosphere of argon has no effect on the magnetic properties of Mn doped ZnO. Co and Ni doped ZnO samples also show similar magnetic properties with no evidence for ferromagnetism (Figure 2.1.6). It appears nearly certain that robust ferromagnetism cannot

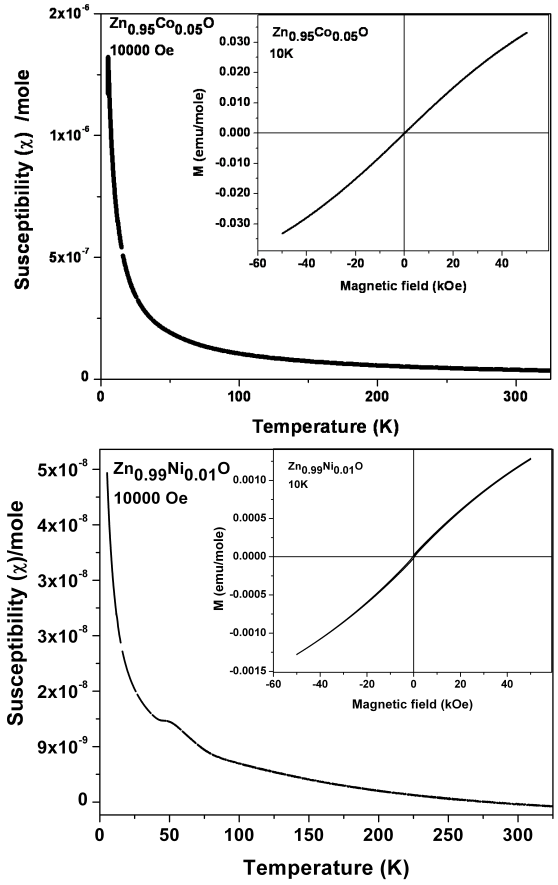

Figure 2.1.6: Magnetic susceptibility versus temperature plots for 5% Co and 1% Ni doped ZnO samples.Insets show M vs H plots for the samples at 10K.

occur in dilute magnetic semiconductors such as Mn doped ZnO and in cases when ferromagnetism is observed, it is not intrinsic [18]. If at all, it may occur if additional charge carriers are present which are most likely to be defect

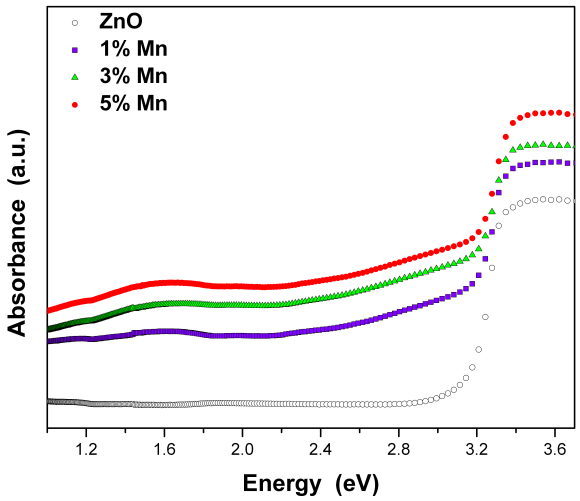

Figure 2.1.7: Absorption spectra of Mn doped ZnO samples.

induced as observed for nanoparticles of many inorganic materials exhibiting surface ferromagnetism including doped as well as undoped ZnO [7, 19, 20].

Typical room temperature optical absorption spectra for $Zn_{1-x}Mn_xO$ samples (0.0< x >0.07) are shown in Figure 2.1.7. Absorbance data was obtained from the diffuse reflectance (R_d) by using the relation, Absorbance (A) = -log(R_d). The band gap energies of the samples were determined using a simple method by taking the intersection of the extrapolated lines from the linear vertical and horizontal regions near the band edge [21]. The variation of the band edge with x is shown in Figure 2.1.8. We observe an initial red shift in the band gap up to 3%, followed by a linear increase with the Mn concentration. This behavior is comparable to that found with thin films and nanoparticles with minimum in the gap for x = 0.03 [4, 14]. This is due to strong sp-d interactions in the samples at low concentration of Mn ions, as mentioned earlier. The larger decrease in the band gap in Mn doped ZnO

nanocrystals found by Vishwanatha et al. [14] is due to spatial confinement.

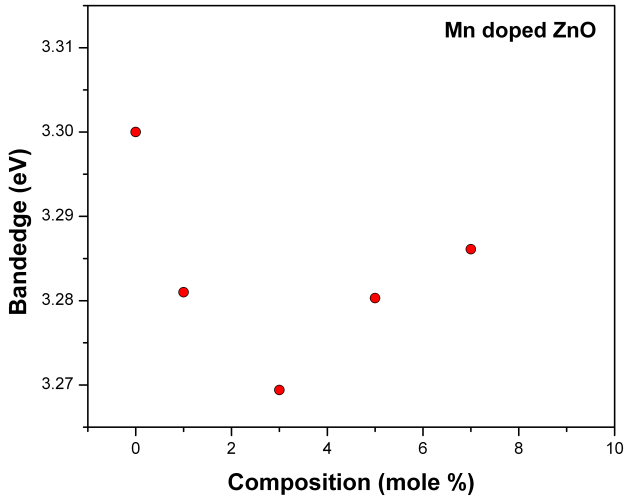

Figure 2.1.8: Shift of band edge in Mn doped ZnO with composition.

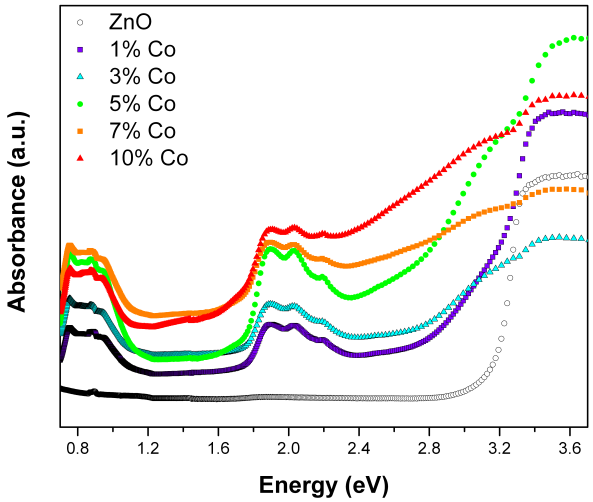

Figure 2.1.9: Absorption spectra of Co doped ZnO.

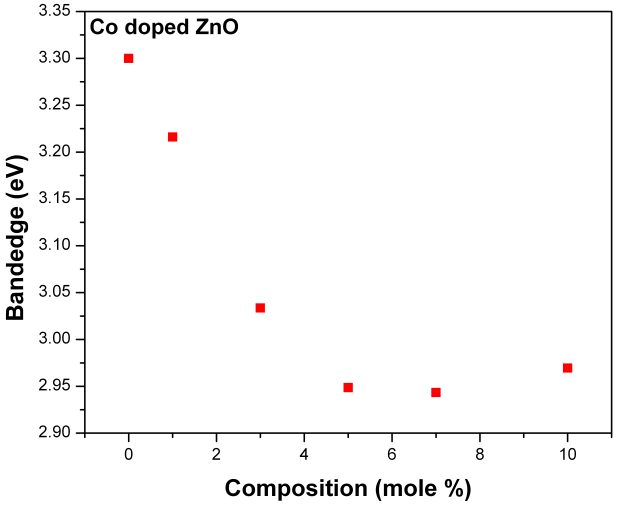

Figure 2.1.10: Shift of band edge in Co doped ZnO with composition.

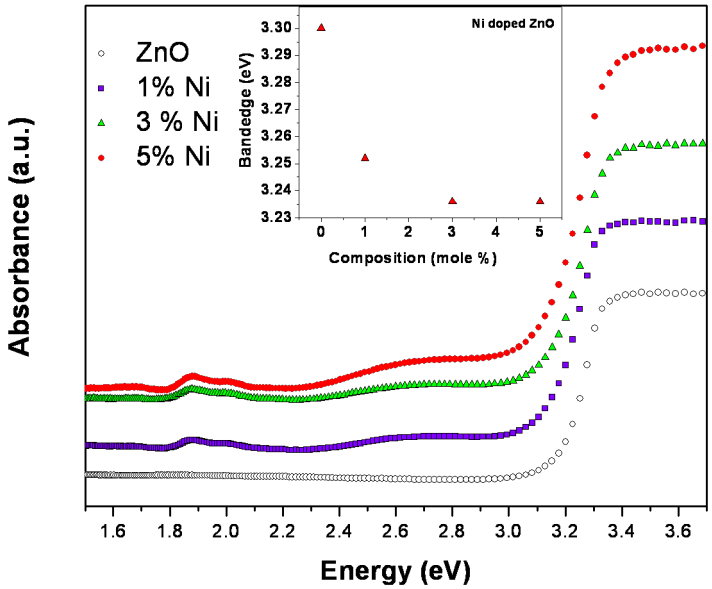

Figure 2.1.11: Absorption spectra of Ni doped ZnO. Inset shows the shift of band edge in Ni doped ZnO with composition.

Typical absorption spectra of Co doped ZnO samples are shown in Figure 2.1.9. The spectra also show additional absorption peaks due to the transitions of tetrahedral Co^{2+} ions [6, 16]. The band gap of Co doped ZnO shows a decrease with increasing Co concentration (Figure 2.1.10), similar to the earlier observations [15, 16]. The decrease in the bandgap is considerably greater than in $Zn_{1-x}Mn_xO$. The spectra of Ni doped ZnO samples are shown in the Figure 2.1.11. The spectra show small additional peaks near 1.9 eV due to the transitions of Ni^{2+} [22]. Inset in Figure 2.1.11 shows that band gap of Ni doped ZnO decreases with composition in conformity with earlier observations on thin films [17], but the decrease in bandgap is smaller than in $Zn_{1-x}Co_xO$. Clearly, sp-d exchange interactions are responsible for the bandgap variations in both Co- and Ni- doped ZnO samples.

2.1.4 Conclusions

The present studies on the magnetic properties of Mn doped ZnO prepared by the decomposition of acetate solid solutions in Ar atmosphere establish them to be not ferromagnetic, again confirming that ZnO cannot be rendered ferromagnetic by doping with Mn. The present studies also show that the bandgap of ZnO doped with Mn^{2+}, Co^{2+} and Ni^{2+} prepared by the decomposition of acetate solid solutions, varies with the composition. Mn^{2+} doped ZnO shows a decrease in the bandgap for low dopant concentrations, followed by a linear increase. Co^{2+} and Ni^{2+} doped ZnO show a progressive decrease in the bandgap with dopant concentration. The decrease in the bandgap in the case of Co^{2+} substituted ZnO is the highest amongst the three systems, with the bandgap decreasing by about 0.3 eV for 4% Co doping.

2.2 Photoluminescence and Photoconducting Properties of ZnO nanoparticles

2.2.1 Introduction

There is tremendous interest in the use of nanomaterials for the fabrication of various types of devices such as sensors, detectors, transistors and solar cells [23]. Ultraviolet photodetectors have a wide range of applications including flame sensing, environmental and biological research, astronomical studies, optical communications and missile launch detection. Conventional UV-enhanced silicon photodiodes for ultraviolet (UV) photodetection, exhibit some limitations inherent to silicon technology. Studies on wide-bandgap semiconductors, such as GaN, SiC, ZnO *etc.* proved the possibility of developing photodetectors with intrinsic visible-blindness operating at room temperature [24].

ZnO, being an environmentally friendly semiconductor with a wide band gap, shows UV photoconducting properties which depend on adsorption and photodesorption of oxygen on the surface. Various methods of synthesis and processing as well as the stability at high temperatures and in harsh environments makes ZnO a material of great interest. UV photodetectors fabricated based on ZnO thin films deposited by metal-organic chemical vapor deposition, pulsed laser deposition or radio frequency sputtering *etc.* known to perform depending sensitively on the stoichiometry and trap densities. There have been several studies on the photoconductivity of sol-gel derived ZnO thin films [25, 26]. Due to the larger surface to volume ratio in comparison to

planar film structures, nanostructures of ZnO are better candidates and has been extensively studied for UV photodetector application. The photoconducting properties of ZnO nanowires produced by chemical vapor deposition have been investigated showing the high sensitivity of the conductivity to UV light exposure [27–29]. Keem *et al.* [30] reported on the photoresponse behavior of ZnO nanowires grown by thermal evaporation of ZnO powder. Ahn *et al.* [31] studied the photoconductivity of ZnO nanorods synthesized by the sol-gel technique. Recently, solution based UV photo detectors using colloidal ZnO particles has been demonstrated by Jin *et al.* [32]. These solution-based ZnO nanoparticle devices appear to be promising as low-cost, flexible, large-area UV photodetectors.

UV photoconductivity of ZnO is governed by surface-related and bulk-related processes. The surface-related process is primarily governed by the adsorption and desorption of the chemisorbed oxygen at the surface of the ZnO, which is exploited for gas sensing applications [33]. It is generally accepted that oxygen molecules are adsorbed onto ZnO surfaces by capturing free electrons from the n-type ZnO which create a low-conductivity depletion layer near the surface.

$$O_2(g) + e^- \longrightarrow O_2^-(ad) \tag{2.2.1}$$

Upon illumination at photon energies above the semiconductor bang gap, electron-hole pairs are generated. The holes that migrate to the surface along the potential gradient produced by band-bending, either discharge the negatively charged adsorbed oxygen ions to photodesorb oxygen from the

surfaces or effectively get trapped at the ZnO nanoparticle surfaces.

$$h^+ + O_2^-(ad) \longrightarrow O_2(g) \tag{2.2.2}$$

This results in an increase in the free carrier concentration and a decrease in the width of the depletion layer. This leads to an enhancement of carrier injection and transport, producing a persistent photocurrent.

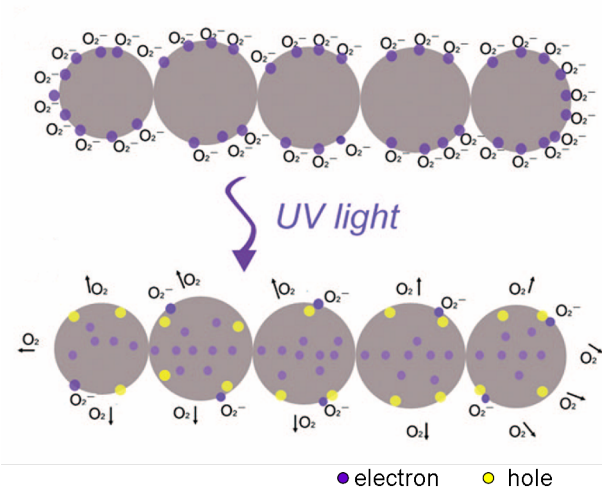

Figure 2.2.1: Charge carrier trapping and transport in the ZnO nanoparticle films in the dark and UV illumination.

When the illumination is turned off, oxygen readsorbs on the nanocrystal surfaces, returning the device to its initial state. This process becomes prominent in nanocrystalline films where the surface area is large (Figure 2.2.1). In the bulk-related process, oxygen molecules in the grain boundaries contribute to photoconductivity. Some O_2 neutrals are embedded in the grain boundaries of ZnO and form oxygen ions by taking up an electron. Upon

UV light illumination, these species liberate electrons by capturing the photo generated holes and the electrons drift in the electric field and contribute to the photoconductivity.

The bulk-related process is however considered to be faster in comparison to the surface-related process. Studies by Kumar *et al.* [34] show role of dispersal of nanoneedles on the surface of the ZnO film where the bulk related phenomena dominates, giving higher and fast photosensitivity. For UV-detection, the fast component, due to the generation of photocarriers and their radiative and nonradiative recombination through local centres, is of greater importance.

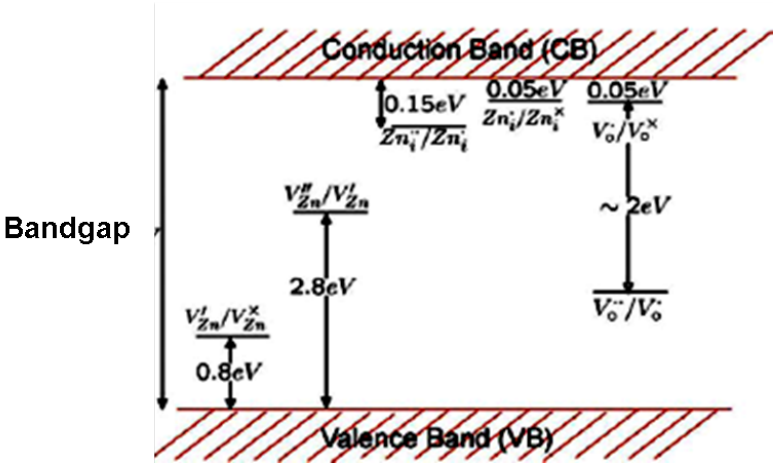

Figure 2.2.2: Energy levels of native defects in ZnO. The donor defects are $Zn_i^{\cdot\cdot}$, $Zn_i^{\cdot}$, $Zn_i^{\times}$, $V_o^{\cdot\cdot}$, $V_o^{\cdot}$, V_o and the acceptor defects are V_{Zn}'', V_{Zn}'. (i = Interstitial sites, Zn = Zinc, O = Oxygen, V = Vacancy. A dot indicates a positive charge, a prime indicates a negative charge and a cross indicates zero charge)(From [35]).

The intrinsic n-type conductivity of ZnO with very high electron density of ∼1021 cm^{-3} is due to availability of lot of oxygen vacancies and Zn interstitials. ZnO has a relatively open structure, with a hexagonal close

packed lattice where Zn atoms occupy half of the tetrahedral sites (see Figure 2.1.1). All the octahedral sites are empty. Hence, there are plenty of sites for ZnO to accommodate intrinsic (namely Zn interstitials) defects and extrinsic dopants. The electronic energy levels of native imperfections in ZnO are illustrated in Figure 2.2.2 There are a number of intrinsic defect states within the bandgap of ZnO with defect ionization energies varying from 0.05 to 2.8 eV. Zn interstitials and oxygen vacancies are known to be the predominant ionic defect types. However, which defect dominates in native, undoped ZnO is still a matter of controversy [35, 36]. These inherent defect centres, such as oxygen vacancies and zinc interstitials are believed to be responsible for visible photoluminescence in ZnO. Markevich *et al.* [37] have shown that recombination centers responsible for the orange band were the centers of photosensitivity.

Defects in ZnO strongly depend on the preparation and annealing conditions which in turn affect the phtoconducting properties. There have been studies on the effect of annealing under different conditions on the defect-related emission of ZnO thin films and nanostructures [35, 38–40]. Thus Ghosh *et al.* [25] found that air-annealed ZnO films are preferable for photodetector applications due to the lower dark current. The large concentration of defects in the ZnO nanostructures prepared at low temperatures can be controlled by annealing in oxygen at different temperatures. It is therefore important to carry out a study of the effect of annealing temperature on the photoluminescence as well as the photoconduction properties of ZnO nanostructures. Also, the low temeprature processed ZnO nanoparticle films are extensively used as electron transport layers in various opto-electronic

devices such as solar cells and light emitting diodes, where these properties may play a crucial role [41,42]. Here,we have studied the effect of annealing in an oxygen atmosphere on the photoluminescence and photoconducting properties of thin films of colloidal ZnO nanoparticles. We have also extended the study to Mn and Co doped ZnO nanoparticles.

2.2.2 Experimental details

ZnO nanocrystals were prepared by a procedure described in the literature [43]. The procedure involves the hydrolysis of zinc acetate in methanol using KOH. In brief, zinc acetate (0.01 moles) was dissolved in methanol (125 ml) under vigorous stirring at about 60^oC. Subsequently, a solution of KOH (0.03 moles, 65 ml) in methanol was added drop wise at 60^oC. The reaction mixture was stirred for 2 h at 60^oC. The resulting nanoparticles were collected and dispersed in choloroform leading to a solution with a concentration of ca. 25 mg/ml. Co and Mn doped ZnO nanoparticles were obtained using the same procedure with addition of cobalt acetate and manganese acetate respectively, to the intitial zinc acetate solution. The nominal percentage of cobalt and manganese in the doped ZnO nanoparticles ($\sim$ 3 mol%) was confirmed by EDAX (Energy Dispersive X-ray Analysis). Transmission electron microscope (TEM) images and selected area electron diffraction (SAED) of ZnO nanoparticles were obtained using a JEOL JEM 3010, operating at 300 kV. X-ray diffraction (XRD) pattern of the nanoparticles was recorded using a Bruker AXS D8 DISCOVER instrument. Thermogravimetric analysis (TGA) of the nanoparticles was carried out on a Mettler- Toledo-TG-850 instrument in an oxygen atmosphere.

Transparent films of the ZnO nanoparticles were prepared on quartz substrates by spin coating the chloroform solution. The thickness of the films was in the range 200-250 nm as measured by using a Dektak Stylus Profiler. The ZnO nanoparticle films were then annealed in 1000 sccm oxygen flow at different temperatures (250^{o}C, 450^{o}C, 550^{o}C and 650^{o}C) for 15 hours. Absorption spectra of the thin films were recorded with a Perkin Elmer UV-visible-NIR spectrometer. Photoluminescence spectra (PL) were recorded using a FluoroLog spectrofluorimeter (JOBIN YVON) using 300 nm light as the excitation.

UV photodetectors were fabricated by evaporating a 100 nm thick gold layer on top of the thin films through a shadow mask to form electrodes with a gap of 150 μm. Electrical measurements of all the devices were carried out with a Keithley 236 source measure unit under ambient conditions. The photocurrent and spectral response of the devices were recorded under illumination by a xenon lamp through a monochromator (TRIAX 180, JOBIN YVON). The intensity of the light at 370 nm was calculated using a Hamamatsu S133 photodiode.

2.2.3 Results and discussion

A typical TEM image of the as-prepared ZnO nanoparticles is shown in Figure 2.2.3. The nanoparticles are crystalline, as revealed by the selected area electron diffraction pattern shown as an inset in the 2.2.3. The diameter of the nanoparticles is in the 3-7 nm range.The XRD pattern of the as-prepared ZnO nanoparticles (Figure 2.2.4) can be indexed on the basis of the wurtzite structure.

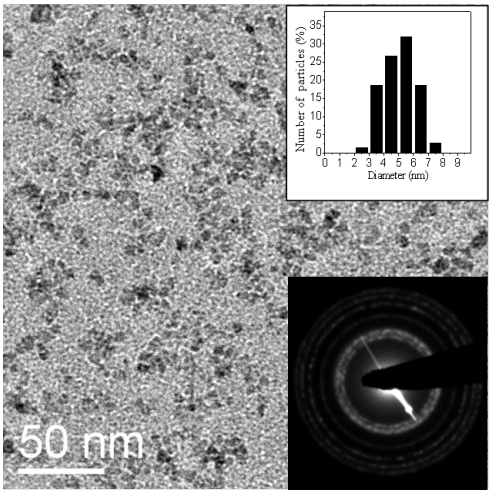

Figure 2.2.3: TEM image of the as-prepared ZnO nanoparticles with the insets showing the particle size distribution and selected area electron diffraction pattern.

Figures 2.2.5 and 2.2.6 show the absorption and PL spectra respectively of the as-prepared ZnO nanoparticle films and the films annealed in oxygen at various temperatures. The as-prepared nanoparticles show a absorption peak at 350 nm, which is blue-shifted compared to that of bulk ZnO (370 nm), due to quantum confinement. As the annealing temperature is increased, the absorbance onset of the ZnO films shifts to higher wavelengths, suggesting that there is an increase in the size of the nanocrystals upon sintering. The PL spectra of the as-prepared nanoparticles show an intense defect- related band centered at 560 nm (green) and a weak band-edge luminescence centered at 373 nm (UV).

In spite of numerous studies on the visible luminescence of ZnO, its origin is still controversial, and a number of suggestions have been made [40]. For example, the green luminescence has been attributed to defects such as

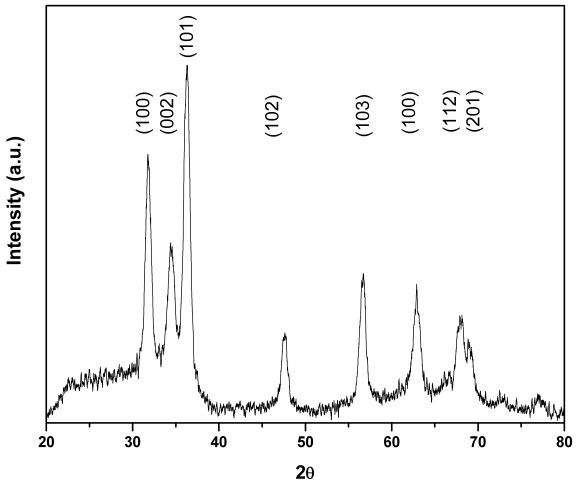

Figure 2.2.4: XRD pattern of the as-prepared ZnO nanoparticles.

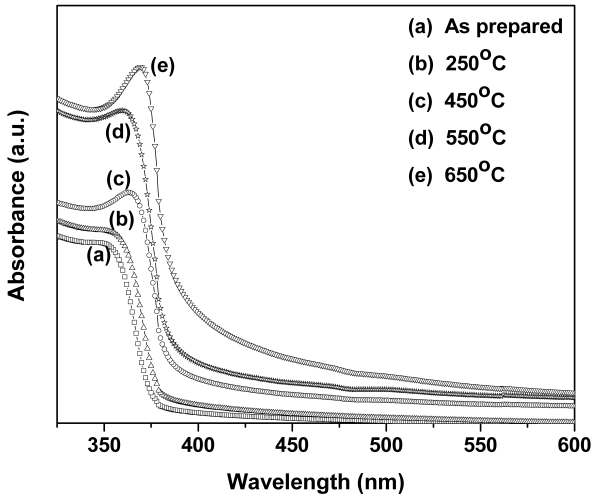

Figure 2.2.5: UV visible absorption spectra of as-prepared ZnO nanoparticle film and the films annealed in oxygen at different temperatures.

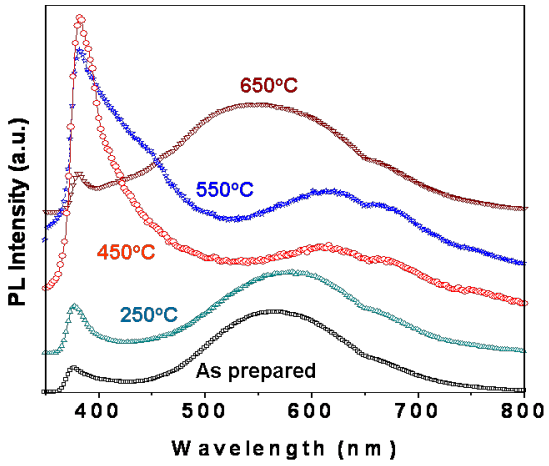

Figure 2.2.6: Photoluminescence spectra of as-prepared ZnO nanoparticle film and the films annealed in oxygen at different temperatures.

oxygen vacancies, zinc vacancies as well as donor-acceptor pairs. In the case of colloidal ZnO nanoparticles, this may be due to the presence of surface defects which include acetate and -OH groups [44]. On annealing in oxygen up to 450^{o}C, there is a dramatic increase in the band-edge luminescence as compared to the intensity of the green emission. This may be due to the removal of the adsorbed groups [45] as indicated by the weight loss in the thermogravimetric analysis (TGA) shown as Figure 2.2.7.

The red shift of the emission peak is due to the increase in particle size upon sintering. The band edge luminescence peak also becomes broader, due to the presence of an additional emission peak developed in the violet region and the emission in the visible region is shifted to longer wavelengths possibly due to the formation of interstitial defects [40]. The peak is more prominent in the samples heated to 550^{o}C, where the size of the nanoparticles

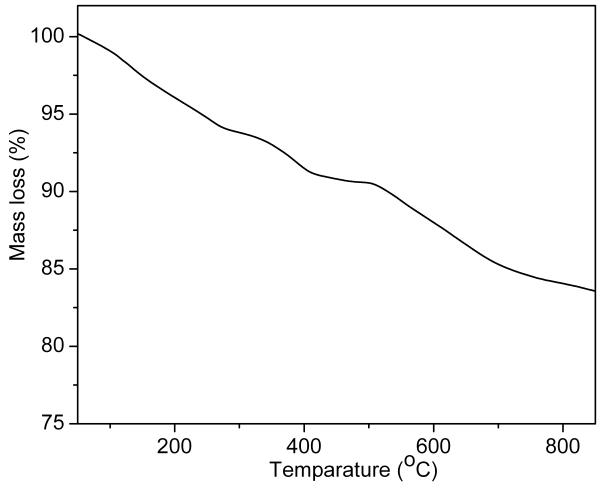

Figure 2.2.7: TGA curve for the ZnO nanoparticles.

increases [46]. Further increase in the annealing temperature leads to the re-appearance of green luminescence as in the films annealed at 650^{o}C. This is because annealing at higher temperatures causes a loss of oxygen leading to oxygen vacancies [38,47]. This is verified from the TGA of ZnO nanoparticles showing a loss of mass around 550^{o}C to 700^{o}C (See Figure 2.2.7). The ratio, R, of PL intensity of the UV near band edge emission to that of the visible broad band emission is listed in Table 2.2.1 as a measure of the optical quality of the films.

Figures 2.2.8 (a) and (b) show the I-V characteristics of the samples annealed at various temperatures, upon UV light illumination (λ = 370 nm) and in dark respectively. The as-prepared sample and the sample annealed at 250^{o}C show I-V characteristics with low values of dark and photocurrents, which may be due to the negatively charged acetate ions adsorbed on the

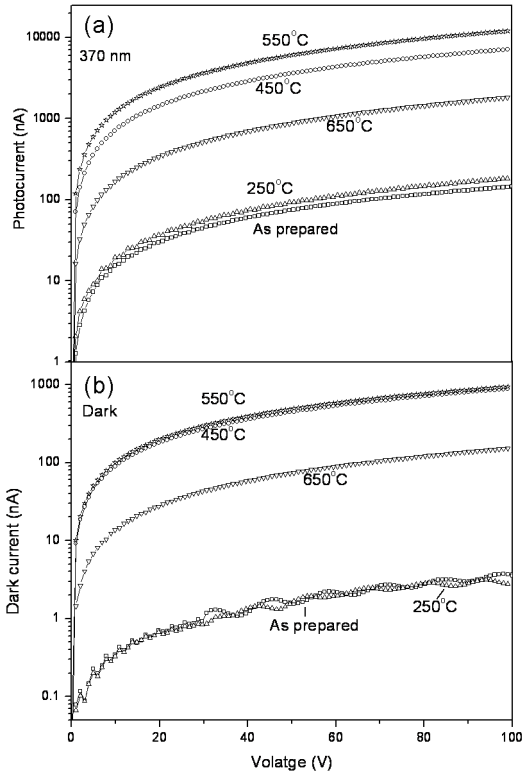

Figure 2.2.8: I-V characteristics of the as-prepared and the annealed ZnO nanoparticle film devices (a) upon UV light illumination and (b) in the dark.

zinc oxide surface resulting in an electrostatic repulsion of the electrons inside the ZnO [48]. As the annealing temperature is increased, both the dark current and the photocurrent of the samples increase due to the removal of the absorbed species from the surface, thereby releasing trapped carriers for conduction. The decrease in the dark and photocurrents for the sample annealed at 650^{o}C is in consistent with the generation of oxygen vacancies as substantiated by the PL spectra. The photocurrent to dark current contrast ratio, η, at 100V for the different samples are listed in Table 2.2.1. The values of η are lower for high temperature annealed samples which also show

	R	η	Responsivity (A/W)	Photoconductive gain	Q	α
ZnO, As prepared	3.3	42	0.15	0.53	41	0.74
ZnO, 250 ^{o}C annealed	1.7	59	0.2	0.68	39	1.12
ZnO, 450 ^{o}C annealed	0.2	9	7	24	34	0.46
ZnO, 550 ^{o}C annealed	0.4	14	12.5	42	12	0.66
ZnO, 650 ^{o}C annealed	2.7	13	1.9	6.4	5	0.33
Co:ZnO, As prepared		5.2	0.17	0.56	1.66	
Mn:ZnO, As prepared		2.1	0.04	0.13	1.04	

Table 2.2.1: The parameters R, η, responsivity, photoconductive gain, Q and α for ZnO nanoparticle films annealed at different temperatures at incident optical power 0.3 mW/cm^2.

a decrease in the intensity of defect related emission in the PL spectra.This demonstrates that defects play a major role in the mechanism of photoconductivity in ZnO. The approximate values of the responsivity of the devices, defined as the photocurrent per unit of incident optical power, at an incident optical power of 0.3 mW/cm^2 are also listed in Table 2.2.1 along with the values of the photoconductive gain (electrons flowing per incident photon).

Figure 2.2.9 presents the spectral photoresponse of the ZnO films annealed at various temperatures. The photocurrent for the as-prepared sample shows an onset at 380 nm, becoming maximum at 350 nm. The photocurrent peak shifts to longer wavelengths as the annealing temperature is increased due to the increase in the size of the nanoparticles, consistent with the absorption spectra. The photoresponse for the wavelengths longer than 400 nm is negligible showing high selectivity of the devices. The values of UV to visible

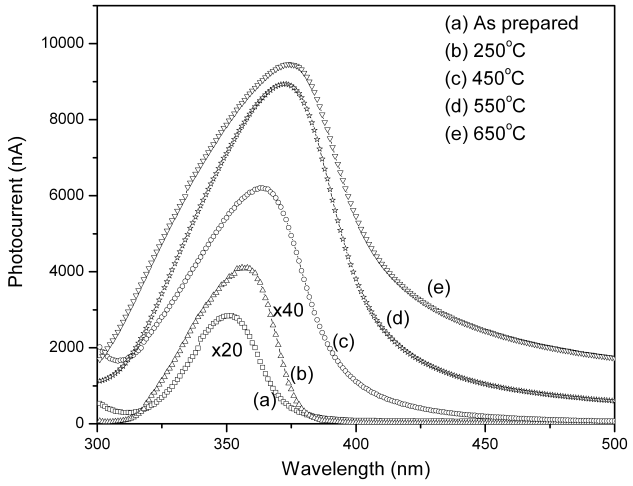

Figure 2.2.9: Spectral photoresponse of the ZnO films annealed at different temperatures.

rejection ratio, Q, defined as the ratio of the maximum photocurrent in the UV region to the minimum photocurrent (at 450 nm), are listed in Table 2.2.1.

The intensity dependence of the photocurrent in a typical ZnO nanoparticle film device annealed at 450^{o}C at 370 nm is shown in Figure 2.2.10. The photocurrent, I_P, follows a simple power law relationship with intensity (P) [28]:

$$I_P = P^{\alpha} \tag{2.2.3}$$

The values of α for the ZnO nanoparticle films annealed at different temperatures are given in Table 2.2.1. The power law dependence is attributed to the varying distribution of the trap states [49, 50].

Figure 2.2.11 shows time-resolved photocurrent spectra at 100 V in response to a 120 s light pulse (370 nm) for the ZnO films annealed at different

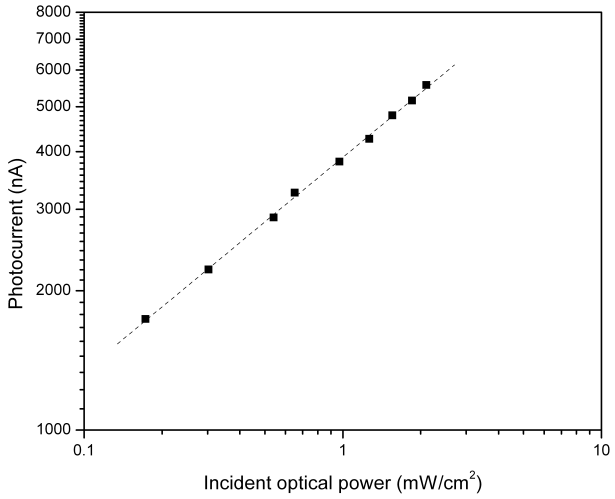

Figure 2.2.10: The dependence of the photocurrent on the incident optical power for a typical ZnO nanoparticle thinfilm device at 370 nm.

temperatures. The time constants for the response and decay are obtained by the linear fitting of the photocurrent response curve in a logarithmic scale, following equations (2.2.4) and (2.2.5) respectively [51].

$$I = I_0(1 - e^{-t/\tau r}) \tag{2.2.4}$$

$$I = I_0(e^{-t/\tau r}) \tag{2.2.5}$$

The response and decay time constants τ_{r1}, τ_{r2}, τ_{d1} and τ_{d2} obtained for the different samples are listed in Table 2.2.2. The photocurrent in the as prepared and the low-temperature annealed samples exhibits rapid growth and decay, suggesting that photoconduction is mainly governed by bulk-related defects. The slower response and increase in the decay time for the

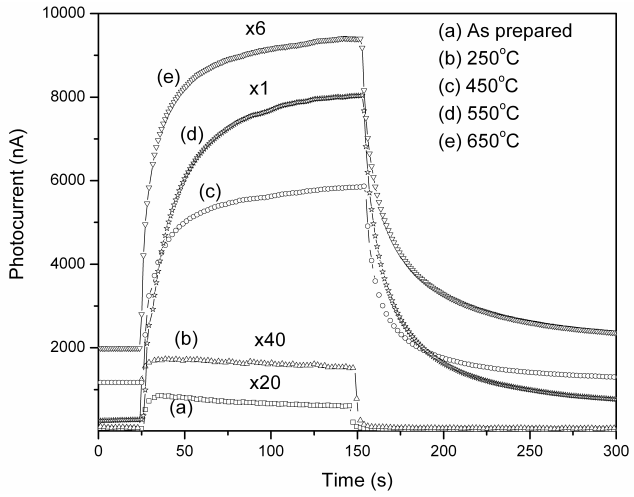

Figure 2.2.11: Time resolved photocurrent spectra for the as prepared and the annealed ZnO nanoparticle thinfilm devices at 100 V in response to a 120 s light pulse.

	τ_{r1} (s)	τ_{r2} (s)	τ_{d1}(s)	τ_{d2}(s)
ZnO, As prepared	3.7	–	6.3	–
250^{o}C annealed	3.5	–	5.6	–
450^{o}C annealed	9	1748	53	1449
550^{o}C annealed	8.6	1136	52	400
650^{o}C annealed	9.7	1587	50	1000
Co:ZnO, As prepared	40	2762	90	1352
Mn:ZnO, As prepared	558	10890	813	14700

Table 2.2.2: The response and decay time constants τ_{r1} , τ_{r2}, τ_{d1} and τ_{d2} for ZnO nanoparticle films annealed at different temperatures.

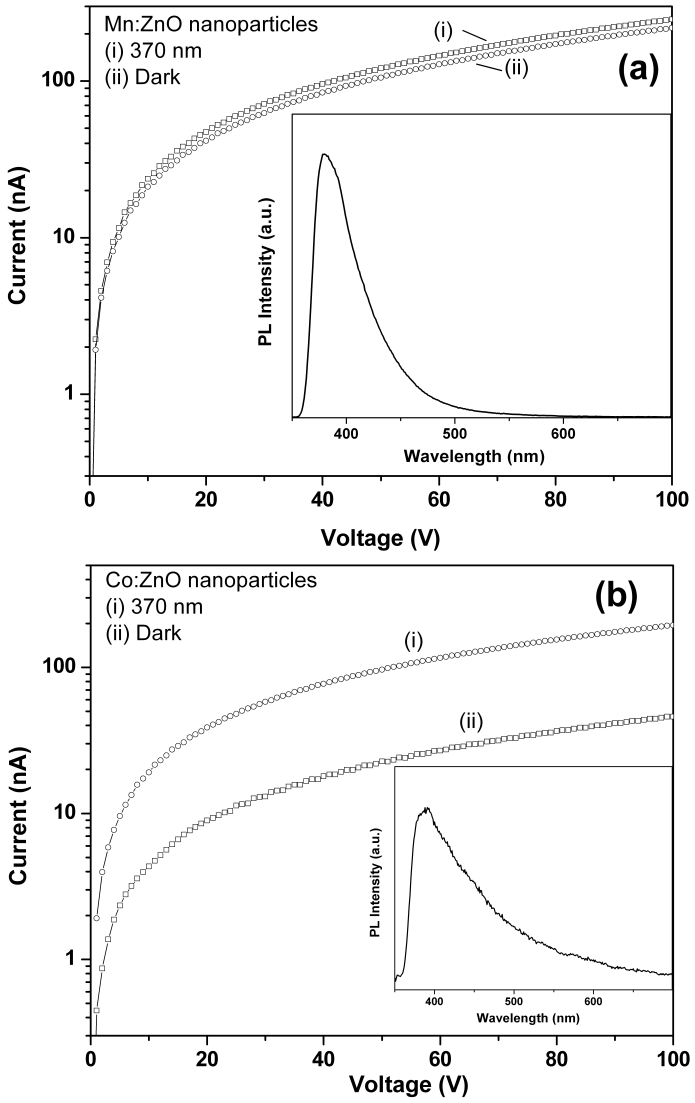

Figure 2.2.12: I-V characteristics in UV light as well as in dark for (a) Mn doped (b) Co doped ZnO nanoparticle film devices. Insets in (a) and (b) show the PL spectra of Mn doped and Co doped ZnO nanparticles respectively.

samples annealed at high temperatures indicate the dominance of the surface related process [34]. The increase in decay time can also be explained based on the increase in the potential barrier height with the increase in grain size [52].

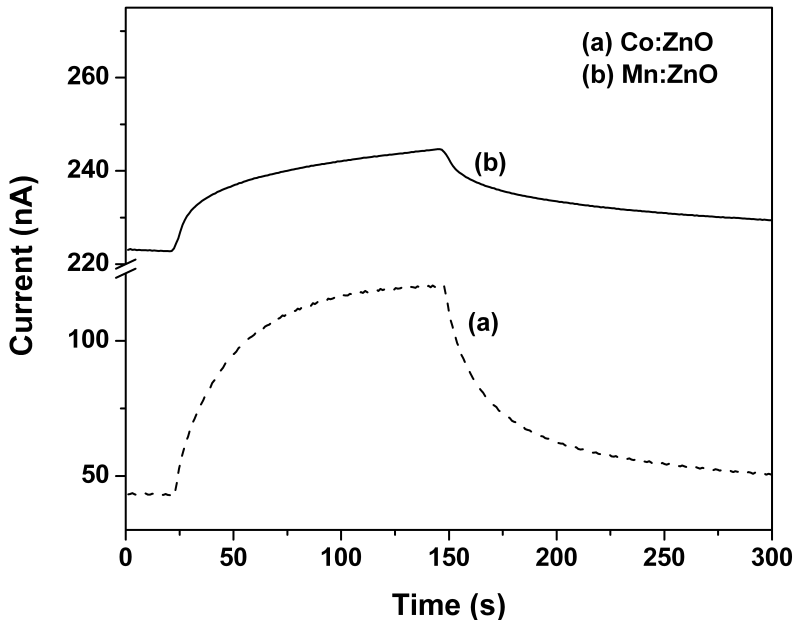

Figure 2.2.13: Time resolved photocurrent spectra for as prepared Mn and Co doped ZnO nanoparticle thinfilm devices at 100 V in response to a 120 s light pulse.

Figures 2.2.12 (a) and (b) show I-V characteristics upon UV light illumination as well as in dark for spin coated thin films of as prepared Mn and Co doped ZnO nanopaticles respectively. Insets in the Figures 2.2.12 (a) and (b) show the PL spectra of the Mn and Co doped ZnO nanoparticles respectively. The PL spectra show that the broad green emission band due to the defects is quenched to a large extent and the band edge emission is enhanced as compared to the undoped ZnO nanoparticles. This indicates

that the nanoparticles are well passivated [53, 54]. The I-V measurements in dark and upon UV light illumination show that the doped samples have higher dark current and lower sensitivity to UV light. The time resolved photocurrent studies on the doped samples showed slower response and decay of the photocurrent (Figure 2.2.13). The values of different parameters for the doped ZnO samples are listed in Tables 2.2.1 and 2.2.2 along with undoped ZnO samples.

2.2.4 Conclusions

In conclusion, the present study demonstrates the marked effect of the annealing temperature on the photoluminescence and photoconducting properties of thin films of ZnO nanoparticles. The results show that the optical quality as well as the dark and the photocurrents of the thin films are strongly dependent on the annealing temperature. The samples annealed at higher temperatures (450^{o}C and 550^{o}C) show higher dark current as well as photocurrent with a slower response and decay compared to samples annealed at lower temperatures. The better photocurrent to dark current ratio shown by low temperature annealed samples, which show defect related green emission, establishes the role defects in photoconductivity. The doping of Co and Mn causes increase in the dark current with decreased photocurrent to dark current ratio, which is substantiated by the absence of green emission. This study suggests a means of controlling defects in ZnO nanoparticles to attain the desired photoconducting properties.

2.3 Photoconductivity of ZnO nanoparticle-Graphene composites

2.3.1 Introduction

Composite materials have received much attention in optoelectronic applications, because they provide the scope to tune the properties depending on the nature of the constituents in the composite structure. For example, it has been shown that by hybridizing two semiconductors [55] and semiconductor-metal systems [56], it is possible to enhance the charge separation and improve the efficiency of the interfacial charge transfer process. Since the mechanism of photoconductivity in ZnO involves charge carrier trapping and transport across ZnO interfaces, the photoconducting properties are expected to be different in the case of composites. Devi *et al.* [57] observed that the photocurrent decays more rapidly in mixed ZnO-MgO system compared to pure ZnO. Negative photoconductivity has been observed for ZnO quantum dots embedded in SiO_2 matrix due to interface defect states acting as trap centres for photoexcited electrons [58]. Photoconductivity in ZnO-polyaniline(PANI) inorganic-organic hybrid structures have been studied and the observed photoresponse parameters were better than those of only ZnO film of similar thickness [59, 60]. Dutta *et al.* [61] showed that ZnO-carbon nanotube nanocomposite structure showed faster ultraviolet photoresponse time constants compared to the bare ZnO.

Similarly, there have been attempts to utilize the nanostructures such as

carbon nanotubes as additives in nano-composites for optoelectronic applications so that one can facilitate their tailored properties [62, 63]. Graphene is new nanocarbon with its interesting electronic and optical properties which are of great interest in academic as well as technological and industrial sectors [64]. Recently, there have been reports of photovoltaic and non-linear optical limiting applications using soluble graphene materials [65, 66]. Also, it has been shown that the bulk films of graphene sheets exhibit photoconductivity upon illumination of a high intensity laser [67]. Graphene with its similar physical properties but larger surface areas, expected to be a low cost alternative to carbon nanotubes in nanocomposites. The development of semiconductor- graphene or metal nanoparticle-graphene composites may provide an important milestone to develop energy harvesting and conversion strategies [68]. Recently, graphene-TiO_2 nanocomposites have been used to prepare thin films acting as electrodes of dye sensitized solar cells (DSSCs) [69]. It has been shown that a small amount of graphene can effectively enhance the performance of DSSCs by providing rapid electron transport paths and extending electron lifetime. Kamat *et al.* [70] showed that the electron transfer from ZnO nanoparticles to graphene oxide sheets has been found to be effective in carrying out its reduction and decreasing the resistivity of chemically functionalized graphene films. Nevertheless, the study on the UV photoresponse properties of ZnO- graphene mixed system is not reported, which generates a curiosity to investigate the effect of graphene as an additive on the photoconductivity of ZnO nanoparticles.

2.3.2 Experimental details

ZnO nanoparticles with an average diameter of 5 nm were prepared by a procedure described in the literature [43]. The method involves hydrolysis of zinc acetate in methanol using KOH. In a typical synthesis, zinc acetate (0.01 mol) was dissolved in methanol (125 ml) under vigorous stirring at about 333 K. Subsequently, a solution of KOH (0.03 mol, 65 ml) in methanol was added drop wise at 333 K. The reaction mixture was stirred for 6 h at 333 K. The white precipitate thus obtained was harvested by centrifugation and washed thoroughly with ethanol and air-dried at 313 K. Graphene (HG) was prepared by carrying out arc discharge of graphite electrodes in the presence of H_2 (200 torr) and He (500 torr). HG contains 2-3 layers of graphene [71].

The dispersion of appropriate composition of ZnO and graphene in CCl_4 was achieved by prolonged sonication for 1 hour. The dispersion was then centrifuged at 4000 RPM and the collected sample was then dried up. The dried up sample was then pressed into the form of rectangular pellet of dimension 4 mm x 7 mm x 1 mm. The electrical connections were made from the two faces of the pellet, using the silver paste and an aluminium sheet as bottom support. This device was held in vertical orientation where the top surface of the pellet could be exposed to UV light (370 nm) from a xenon lamp through a monochromator (TRIAX 180, JOBIN YVON). Electrical measurements of all the devices were carried out with a Keithley 236 source-measure unit under ambient conditions.

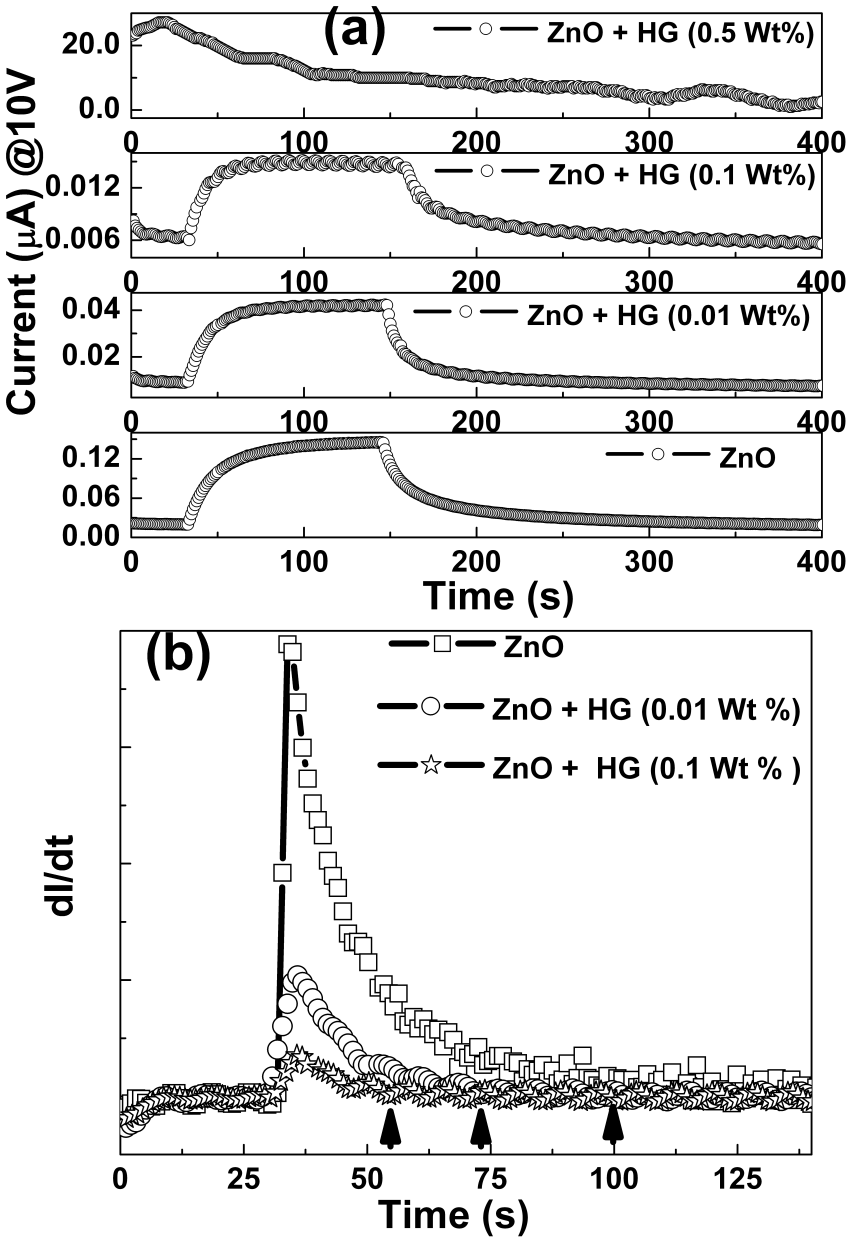

Figure 2.3.1: (a) Photocurrent and (b) differential current as functions of time for a fixed voltage (10 V) for ZnO nanoparticles in admixture with various weight percentages of HG.

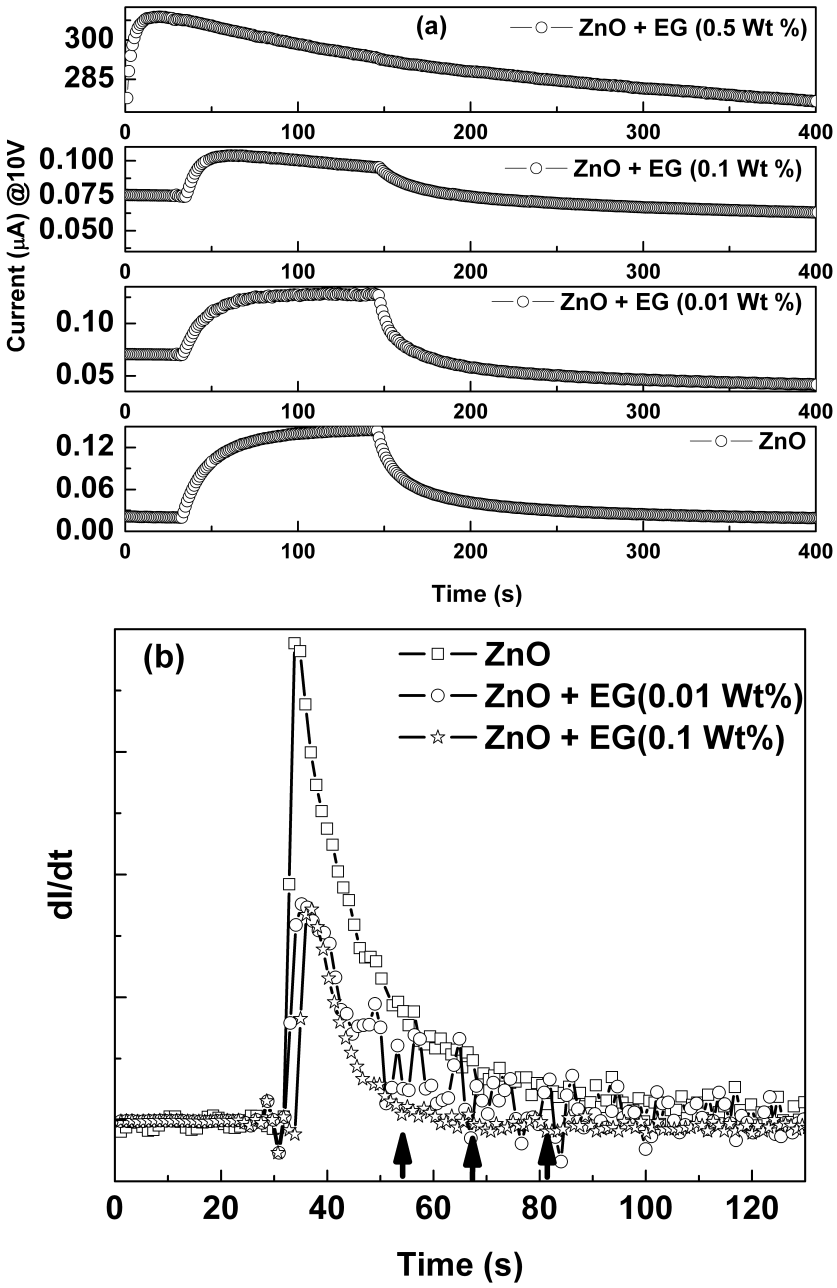

Figure 2.3.2: (a) Photocurrent and (b) differential current as functions of time for a fixed voltage (10 V) for ZnO nanoparticles in admixture with various weight percentages of EG.

2.3.3 Results and discussion

In Figure 2.3.1a we show the results from time resolved photocurrent studies of ZnO samples with different wt % of graphene (HG) as the additive. The time resolved photocurrent spectra were recorded at an applied voltage of 10 V, in response to a light pulse with the width of $\sim$ 120 s and wavelength 370 nm. The photoconductivity was found to decrease gradually with the increase in the graphene content. The results show that even a small amount of HG in ZnO improves the photoresponse, with quick saturation time as illustrated in differential current vs. time graph in Figure 2.3.1b. With the gradual increase in loading of graphene, response to the UV light becomes faster and at the same time, the photoconductivity reduces. Reduction in the conductivity with increase in HG loading may be attributed to the charging of graphene flakes. At 0.5 wt % of HG, however, electrical conductivity in dark increases by several orders of magnitude, possibly due to the formation of electrically conducting channels and it does not show any photoconductivity. We have found similar results with mixture of ZnO and EG, the graphene obtained by exfoliation of graphitic oxide (Figure 2.3.2).

2.3.4 Conclusions

Photoconductivity of ZnO nanoparticles have been observed to change by adding graphene to it. The addition of small amount ($<$ 0.5 wt %) of graphene to ZnO nanoparticles gives rise to fast response to UV light and also decrease in photoconductivity. There is increase in conductivity of ZnO nanoparticles by adding 0.5 wt % graphene to it.

References

[1] V. A. Karpina, V. I. Lazorenko, C. V. Lashkarev, V. D. Dobrowolski, L. I. Kopylova, V. A. Baturin, S. A. Pustovoytov, A. J. Karpenko, S. A. Eremin, P. M. Lytvyn, V. P. Ovsyannikov, E. A. Mazurenko, *Cryst. Res. Technol.* **39**, 980 (2004).

[2] W. Prellier, A. Fouchet, B. Mercey, *J. Phys. Condens. Matter* **15**, R1583 (2003).

[3] P. Sharma, A. Gupta, K. Rao, F. Owens, R. Sharma, R. Ahuja, J. Guillen, B. Johansson, G. Gehring, *Nat.Mater.* **2**, 673 (2003).

[4] T. Fukumura, Z. Jin, A. Ohtomo, H. Koinuma, M. Kawasaki, *Appl.Phys.Lett.* **75**, 3366 (1999).

[5] S. Kolesnik, B. Dabrowski, *J.Appl.Phys.* **96**, 5379 (2004).

[6] C. N. R. Rao, F. L. Deepak, *J.Mater.Chem.* **15**, 573 (2005).

[7] K. R. Kittilstved, N. S. Norberg, D. R. Gamelin, *Phys. Rev. Lett.* **94**, 147209 (2005).

[8] J. Philip, A. Punnoose, B. I. Kim, K. M. Reddy, S. Layne, J. O. Holmes, B. Satpati, P. R. LeClair, T. S. Santos, J. S. Moodera, *Nat.Mater.* **5**, 298 (2003).

[9] W. Chen, L. F. Zhao, Y. Q. Wang, J. H. Miao, S. Liu, Z. C. Xia, S. L. Yuan, *Appl.Phys.Lett.* **87**, 042507 (2005).

[10] P. Olsson, J.-F. Guillemoles, C. Domain, *J. Phys.: Condens. Matter* **20**, 064226 (2008).

[11] J. K. Furdyna, *J.Appl.Phys.* **64**, R29 (1988).

[12] R. B. Bylsma, W. M. Becker, J. Kossut, U. Debska, D. Yoder-Short, *Phy.Rev.B* **33**, 8207 (1986).

[13] S. W. Jung, A. S.-J., G. . Yi, C. U. Jung, S. . Lee, S. Cho, *Appl.Phys.Lett.* **80**, 4561 (2002).

[14] R. Viswanatha, S. Sapra, S. S. Gupta, B. Satpati, P. V. Satyam, B. N. Dev, D. D. Sarma, *J.Phys.Chem.B* **108**, 6303 (2004).

[15] K. J. Kim, Y. R. Park, *Appl.Phys.Lett.* **81**, 1420 (2002).

[16] M. Bouloudenine, N. Viart, S. Colis, A. Dinia, *Chem.Phys.Lett.* **397**, 73 (2004).

[17] D. Shimono, S. Tanaka, T. Torikai, T. Watari, M. Murano, *J.Ceram.Process.Res.* **2**, 184 (2001).

[18] R. Seshadri, *Curr. Opin. Solid State Mater. Sci.* **9**, 1 (2005).

[19] A. Sundaresan, C. N. R. Rao, *solid state commun.* **149**, 1197 (2009).

[20] D. Inamdar, A. Lad, A. Pathak, I. Dubenko, N. Ali, S. Mahamuni, *J.Phys.Chem.C* **114**, 1451 (2010).

[21] M. Nowak, B. Kauch, P. Szperlich, *Rev. Sci. Instrum.* **80**, 046107 (2009).

[22] P. V. Radovanovic, N. S. Norberg, K. E. McNally, D. R. Gamelin, *J.Am.Chem.Soc.* **124**, 15192 (2002).

[23] C. N. R. Rao, A. Mueller, A. K. Cheetham, *The Chemistry of Nanomaterials: Synthesis, Properties and Applications* (Wiley-VCH, Weinheim, 2004).

[24] E. Monroy, F. Omns, F. Calle, *Semicond.Sci.Technol.* **18**, R33 (2003).

[25] R. Ghosh, B. Mallik, S. Fujihara, D. Basak, *Chem.Phys.Lett.* **403**, 415 (2005).

[26] S. Mridha, D. Basak, *Chem.Phys.Lett.* **427**, 62 (2006).

[27] A. Bera, D. Basak, *Appl.Phys.Lett.* **93**, 053102 (2008).

[28] H. Kind, H. Yan, B. Messer, M. Law, P. Yang, *Adv.Mater.* **14**, 158 (2002).

[29] J. B. K. Law, J. T. L. Thong, *Appl.Phys.Lett.* **88**, 133114 (2006).

[30] K. Keem, H. Kim, G. . Kim, J. S. Lee, B. Min, K. Cho, M. . Sung, S. Kim, *Appl.Phys.Lett.* **84**, 4376 (2004).

[31] S. E. Ahn, J. L. Soo, H. Kim, S. Kim, B. H. Kang, K. H. Kim, G. T. Kim, *Appl.Phys.Lett.* **84**, 5022 (2004).

[32] Y. Jin, J. Wang, B. Sun, J. C. Blakesley, N. C. Greenham, *Nano Lett.* **8**, 1649 (2008).

[33] C. S. Rout, A. R. Raju, A. Govindaraj, C. N. R. Rao, *J.Nanosci.Nanotechnol.* **7**, 1923 (2007).

[34] S. Kumar, G. . Kim, K. Sreenivas, R. P. Tandon, *J.Phys.Condens.Matter* **19**, 472202 (2007).

[35] L. Schmidt-Mende, J. L. MacManus-Driscoll, *Mater.Today* **10**, 40 (2007).

[36] A. Janotti, C. G. V. de Walle, *Rep. Prog. Phys.* **72**, 126501 (2009).

[37] I. V. Markevich, V. I. Kushnirenko, L. V. Borkovska, B. M. Bulakh, M. K. Sheinkman, I. V. Prokopenko, *Solid State Commun.* **144**, 236 (2007).

[38] L. Irimpan, D. Ambika, V. Kumar, V. P. N. Nampoori, P. Radhakrishnan, *J.Appl.Phys.* **104**, 033118 (2008).

[39] S. Kurbanov, G. Panin, T. W. Kim, T. W. Kang, *Jpn.J.Appl.Phys.* **46**, 4172 (2007).

[40] A. B. Djurisic, Y. H. Leung, K. H. Tam, Y. F. Hsu, L. Ding, W. K. Ge, Y. C. Zhong, K. S. Wong, W. K. Chan, H. L. Tam, K. W. Cheah, W. M. Kwok, D. L. Phillips, *Nanotechnology* **18**, 095702 (2007).

[41] H. J. Bolink, E. Coronado, M. Sessolo, *Chem.Mater.* **21**, 439 (2009).

[42] S. K. Hau, H. L. Yip, N. Baek, J. Zou, K. Malley, A. Jen, *Appl.Phys.Lett.* **92**, 253301 (2008).

[43] C. Pacholski, A. Kornowski, H. Weller, *Angew.Chem.Int.Ed.* **41**, 1188 (2002).

[44] H. K. Yadav, K. Sreenivas, V. Gupta, S. P. Singh, R. S. Katiyar, *J.Mater.Res.* **22**, 2404 (2007).

[45] V. Noack, A. Eychmller, *Chem.Mater.* **14**, 1411 (2002).

[46] L. Irimpan, V. P. N. Nampoori, P. Radhakrishnan, A. Deepthy, B. Krishnan, *J.Appl.Phys.* **102**, 063524 (2007).

[47] J. Zhou, Y. Wang, F. Zhao, Y. Wang, Y. Zhang, L. Yang, *J.Lumin.* **119-120**, 248 (2006).

[48] C. Ingrosso, A. Petrella, M. L. Curri, M. Striccoli, P. Cosma, P. D. Cozzoli, A. Agostiano, *Appl.Surf.Sci.* **246**, 367 (2005).

[49] J. J. Schellenberg, K. C. Kao, *J.Phys.D: Appl.Phys.* **21**, 1764 (1988).

[50] N. V. Joshi, *Photoconductivity: Art, Science, and Technology* (Marcel Dekker Inc. New York, 1990).

[51] S. Mridha, M. Nandi, A. Bhaumik, D. Basak, *Nanotechnology* **19**, 275705 (2008).

[52] R. Ghosh, D. Basak, *J.Appl.Phys.* **101**, 113111 (2007).

[53] X. T. Zhang, Y. C. Liu, J. Y. Zhang, Y. M. Lu, D. Z. Shen, X. W. Fan, X. G. Kong, *J. Cryst. Growth* **254**, 80 (2003).

[54] R. Viswanatha, S. Chakraborty, S. Basu, D. D. Sarma, *J. Phys. Chem. B* **110**, 22310 (2006).

[55] L. Spanhel, H. Weller, A. Henglein, *J. Am. Chem. Soc.* **109**, 6632 (1987).

[56] V. Subramanian, E. E. Wolf, P. V. Kamat, *J. Am. Chem. Soc.* **126**, 4943 (2004).

[57] S. Devi, S. G. Prakash, *Pramana- J.Phys.* **39**, 145 (1992).

[58] S. Panigrahi, A. Bera, D. Basak, *Appl.Mater.Interfaces* **1**, 2408 (2009).

[59] G. K. Paul, A. Bhaumika, A. S. Patra, S. K. Bera, *Mater.Chem.Phys.* **106**, 360 (2007).

[60] S. Mridha, D. Basak, *Appl. Phys. Lett.* **92**, 142111 (2008).

[61] M. Dutta, D. Basak, *Chem.Phys.Lett.* **480**, 253 (2009).

[62] B. Pradhan, S. K. Batabyal, A. J. Pal, *Appl. Phys. Lett.* **88**, 093106 (2006).

[63] A. Chindaduang, P. Duangkaew, S. Pratontep, G. Tumcharern, *J. Microsc. Soc. Thailand* **23**, 115 (2009).

[64] C. N. R. Rao, K. Biswas, K. S. Subrahmanyam, A. Govindaraj, *J. Mater. Chem.* **19**, 2457 (2009).

[65] Z. Liu, Q. Liu, Y. Huang, Y. Ma, S. Yin, X. Zhang, W. Sun, Y. Chen, *Adv. Mater.* **20**, 3924 (2008).

[66] M. Feng, H. Zhan, Y. Chen, *Appl.Phys.Lett.* **96**, 033107 (2010).

[67] X. Lv, Y. Huang, Z. Liu, J. Tian, Y. Wang, Y. Ma, J. Liang, S. Fu, X. Wan, Y. Chen, *Small* **5**, 1682 (2009).

[68] P. V. Kamat, *J. Phys. Chem. Lett.* **1**, 520 (2010).

[69] S. Sun, L. Gao, Y. Liu, *Appl.Phys.Lett.* **96**, 083113 (2010).

[70] G. Williams, P. Kamat, *Langmuir* **25**, 13869 (2009).

[71] K. S. Subrahmanyam, L. S. Panchakarla, A. Govindaraj, C. N. R. Rao, *J. Phys. Chem. C* **113**, 4257 (2009).

Part 3

Investigations of Gallium Nitride Nanoparticles

Summary

Indium-doped GaN nanoparticles with 5% and 10% In have been prepared by a low temparature solvothermal method using hexamethyldisilazane as the nitriding reagent. The nanoparticles show Raman bands at lower frequencies compared to GaN. Photoluminescence spectra of the In-doped GaN nanoparticles exhibit an increase in the FWHM with the decrease in the PL band energy, the band energy itself decreasing with increase in the In content.

Optical properties of nanocomposites of GaN nanoparticles, 2-4 nm in diameter, with conjugated polymers such as poly(2-methoxy,5-(2-ethylhexoxy)-1,4-phenylenevinylene (MEHPPV) as well as with phosphor nanoparticles have been investigated for use as white light sources. Photoluminescence

Papers based on the studies have appeared in Solid State Communications (2007) and (2008).

spectra of the nanocomposites with different weight ratios of the two components are reported. Weak electroluminescence has been observed in the case of MEHPPV-GaN nanocomposites. The GaN-nanophosphor composites exhibit a high quality white light with good CIE coordinates along with an excellent colour rendering index.

3.1 Synthesis and Optical properties of In-doped GaN nanoparticles

3.1.1 Introduction

In recent years III-nitride materials such as GaN have rapidly gained prominence as efficient optical materials for laser diodes(LDs), photodetectors and light emitting diodes (LEDs). The mixture of GaN with In (InGaN) or Al (AlGaN) with a band gap dependent on the ratio of In or Al to GaN allows the manufacture of LEDs with colors that can span the UV to visible wavelength regimes. The good spectral match to sunlight, together with high heat capacity and resistance to ionizing radiation, makes them potentially suitable for solar cell arrays for satellites.

High brightness blue, green, and yellow LEDs and blue laser diodes have been fabricated using InGaN quantum wells as active layers [1, 2]. Indium gallium nitride's advantages are many. It has tremendous heat capacity and, like other group III nitrides, is extremely resist to radiation. Several studies have been reported on the growth and characterization of InGaN thin films [3–9]. III-nitride heterostructure devices have predominantly been formed through epitaxial growth techniques such as (MOCVD) or molecular beam epitaxy (MBE). It is well known that the InGaN LED devices grown by MOCVD show improved efficiency due to In-segregation [10]. Several workers have studied the phenomenon of phase separation in InGaN, since In-rich regions play an important role in the high efficiency emission of nitride-based blue or green LEDs and LDs [6, 9, 11]. Several approaches for the

fabrication of InGaN quantum dots by MBE and MOCVD are reported in the literature [12–14]. It is, however, difficult to obtain InGaN with high In content due to high volatility of In at high growth temperatures commonly employed in MOCVD and such synthetic methods [4].

A solution based synthesis would provide a path for nanoparticle based self assembly and layer by layer deposition of III-V nitrides free from lattice matched surfaces and catalysts. Thus, the interest in new chemical routes for the preparation of nanostructures of III-V nitrides continues to grow at a fast pace, driven primarily by the possibility of flexible, low cost, large area devices. Although colloidal GaN nanoparticles have been an important target material for some time, they have proven to be difficult to synthesize and to study. However, nanostructures of metal nitrides have been prepared by several methods, the most common one being the reaction of the metals (M = Al, Ga, In), their oxides or halides with NH_3, N_2, azides or nitrides. Promising methods to produce colloidal GaN nanostructures include thermal decomposition of single source precursors such as gallium urea complex and reaction of gallium cupferron or gallium chloride with hexamethyldisilazane (HMDS) in solvothermal or refluxing conditions. [15–17].

Mn doped GaN nanopartilces have been synthesised by the solvothermal decomposition of solid solution of gallium and manganese cupferronates or chlorides in the presence of HMDS [18]. To our knowledge there is no literature report on the preparation and properties of In-doped GaN nanoparticles by chemical route. We were, therefore, interested to explore whether it is possible to prepare nanoparticles of In-doped GaN nanoparticles at low temperatures and investigate their optical properties. For this purpose,

we have employed the low temperature solvothermal method employing the organometallic reagent with HMDS [15] to prepare In-doped GaN nanoparticles and studied the optical properties of the nanoparticles so obtained.

3.1.2 Experimental details

The method of synthesis of the InGaN nanoparticles involves the solvothermal decomposition of a solid solution of gallium (III) and indium (III) cupferronates, $(Ga_{1-x}In_x)$ $(C_6H_5N_2O_2)_3$, in the presence of hexamethyldisilazane (HMDS). 5% and 10% In - doped GaN nanoparticles were obtained by the reaction of 150 mg of the respective cupferronate solid solutions, $(Ga_{0.95}In_{0.05})$ $(C_6H_5N_2O_2)_3$ and $(Ga_{0.9}In_{0.1})$ $(C_6H_5N_2O_2)_3$, respectively with 4 ml of HMDS in 6 ml of toluene in a Swagelok autoclave at 300^{o}C for 24 h .

TEM images of the nanoparticles were recorded using a JEOL (JEM3010) microscope operating with an accelerating voltage of 300 kV. X-ray diffraction (XRD) patterns were recorded using a Phillips X'Pert diffractometer employing the Bragg-Brentano configuration. Photoluminescence (PL) spectra were recorded using a Perkin-Elmer LS 50B luminescence spectrophotometer fitted with a Xenon lamp excitation source (200-900nm). Micro Raman spectra were recorded with a LabRAM HR800 spectrometer using 632 nm laser radiation.

3.1.3 Results and discussion

Figure 3.1.1 shows typical TEM images of the 5% and 10% In - doped GaN nanoparticles. The nanoparticles have an average diameter of $\sim$ 9-10 nm as revealed in the size distribution histograms shown as inset of Figure 3.1.1.

XRD patterns of the nanoparticles show broad reflections similar to those observed with small nanoparticles of GaN [15, 19, 20]. The (100), (002), and (101) reflections of hexagonal GaN merge to form a broad band in the XRD pattern (Figure 3.1.2).

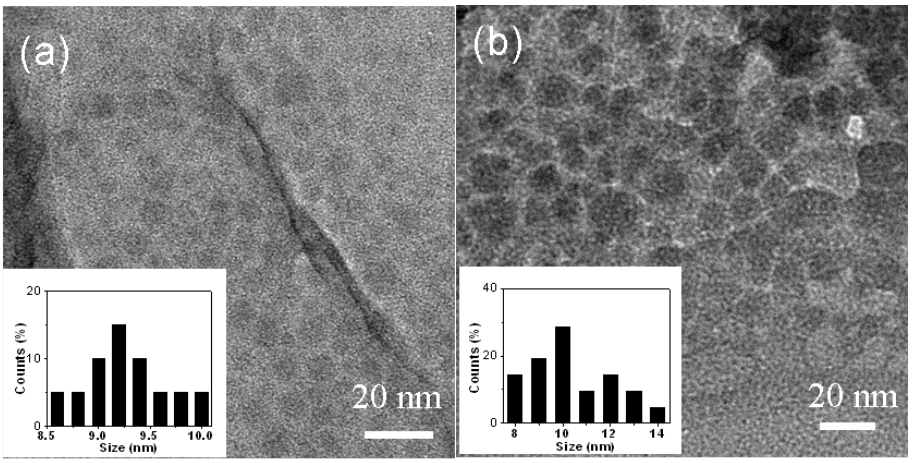

Figure 3.1.1: TEM images of (a) 5% In- doped and (b) 10% In- doped GaN nanoparticles. The insets show size distribution histograms.

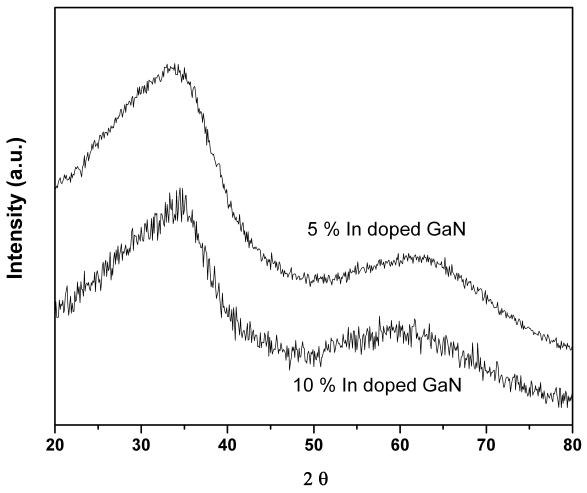

Figure 3.1.2: XRD patterns of 5% In- doped and 10% In- doped GaN nanoparticles.

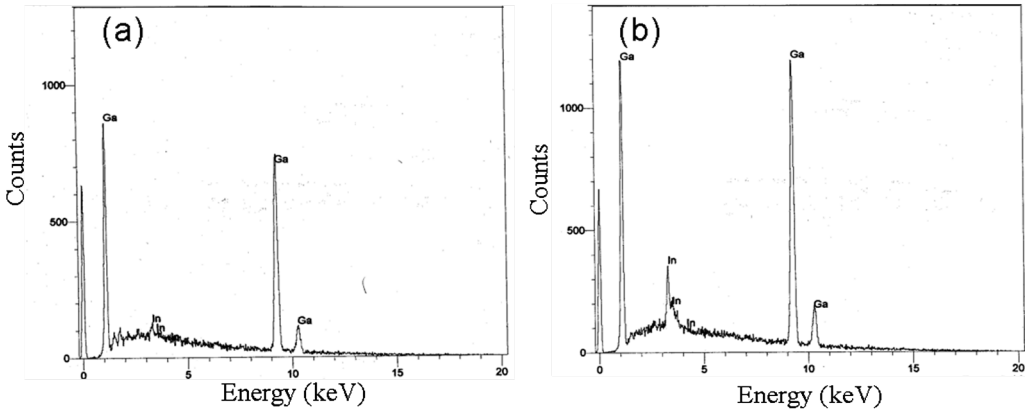

Figure 3.1.3: EDAX analysis of (a) 5% In- doped and (b) 10% In- doped GaN nanoparticles.

In Figures 3.1.3 (a) and (b) we show the results of energy dispersive x-ray analysis (EDAX) of 5% and 10% In-doped GaN nanoparticles. The analysis showed the presence of indium in the InGaN nanoparticles with the expected percentage. Raman spectra of In-doped GaN nanoparticles are shown in Figure 3.1.4. GaN nanoparticles exhibit Raman bands at 566 and 734 cm^{-1} corresponding to E_2 and A_1 modes respectively [21]. The E_2 modes of the 5% and 10% In-doped GaN nanoparticles appear at 560 cm^{-1} and 535 cm^{-1} respectively. The A_1 band of the 5% and 10% In-doped GaN nanoparticles appear at 714 cm^{-1} and 680 cm^{-1} respectively. We thus see a decrease in the Raman frequencies with increase in indium content of InGaN nanoparticles. It should be noted that InN itself shows these Raman bands corresponding to E_2 and A_1 modes at 490 cm^{-1} and 583 cm^{-1} respectively [22]. Thus, the Raman bands of the In-doped GaN nanoparticles fall in between those of GaN and InN, as one would expect [23].

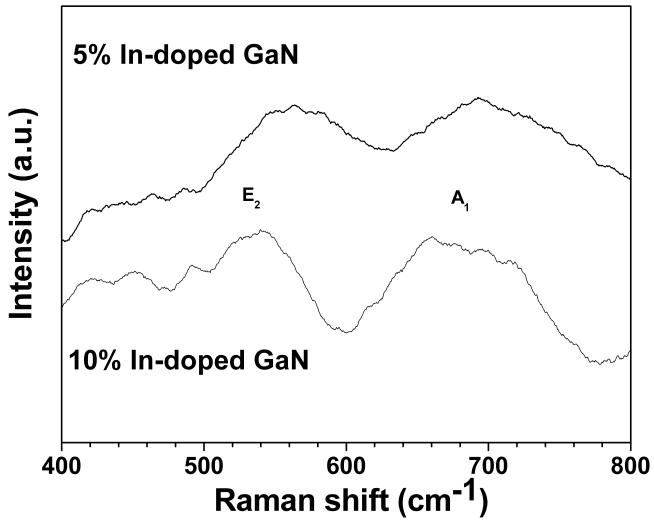

Figure 3.1.4: Raman spectra of In- doped GaN nanoparticles.

In Figure 3.1.5, we show the PL spectra of the In-doped nanoparticles along with spectrum of pure GaN nanoparticles. With increase in the percentage indium doping, the PL band shifts to longer wavelengths. We show the variation of the PL band position with the percentage of indium in InGaN nanoparticles in Figure 3.1.6. For purpose of comparison, we have plotted the PL data from literature [3, 4, 11]. The PL bands observed by us occur at much lower energy (longer wavelength) than those reported for InGaN thin films [3, 4]. Lemos *et al.* [11] have, however, reported the PL band energies for cubic InGaN quantum dot layers to be much lower than those observed by us and have suggested that the emission could originate from In-rich phases present in the layers.

In Figure 3.1.7 we plotted the full-width at half maximum (FWHM) of PL bands against the band energy. We can see that the FWHM of the PL

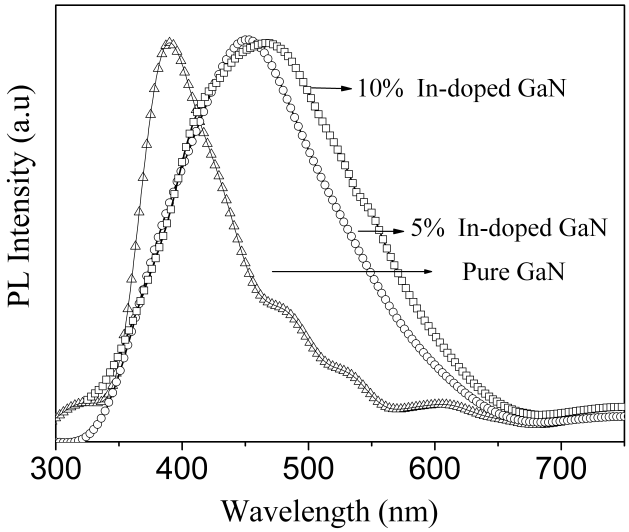

Figure 3.1.5: Photoluminescence spectra of pure GaN and In- doped GaN nanoparticles.

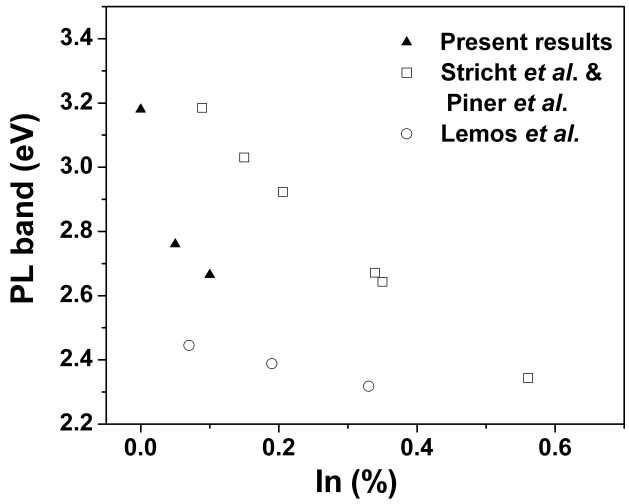

Figure 3.1.6: Variation of PL band position with the mole fraction of In in In-doped GaN nanoparticles.

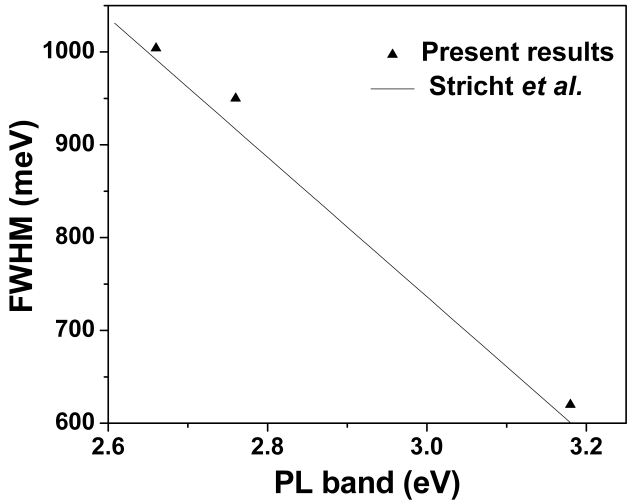

Figure 3.1.7: Variation of FWHM of the PL band with the PL energy in In-doped GaN nanoparticles.

band decreases with the increase in band energy or with the decrease in the indium content in the InGaN nanoparticles. The FWHM values observed are much larger than the values reported earlier in the literature for InGaN thin films [3]. We have therefore normalized our data with respect to the literature data at a band energy 2.66 eV. We see the nature of variation of the FWHM with the band energy observed by us is similar to the earlier reports in the literature on thin films. Interestingly, the slopes are comparable. The broadening of the emission line is an intrinsic property of InGaN alloys, factors such as local inhomogeneity in the indium content and strain-induced piezoelectric effect play a role [24, 25].

3.1.4 Conclusions

Solvothermal decomposition of mixed metal cupferronates in the presence of HMDS gives nanoparticles of In-doped GaN. It should be possible to employ the method to prepare GaN nanoparticles with a range of In concentrations as well as Al-doped GaN nanoparticles. The Raman and PL spectra of the In-doped GaN nanoparticles show systematic changes with In content.

3.2 White light sources based on composites of GaN nanoparticles with conducting polymers and nanophosphors

3.2.1 Introduction

Artificial lighting represents a major component of energy consumption, accounting for a significant part of all energy consumed worldwide. Approximately 20% of global electricity consumption is used only for illumination. The first commercial technology for lighting was based on natural gas that served thousands of streets, offices, and homes at the end of the 19th century. Ultimately, the gaslights were displaced by incandescent light bulbs. Fluorescent tubes and compact fluorescent lamps became widely available in the 1950s and early 1990s, respectively. Along with high-intensity discharge lamps, they offer a longer life and lower power consumption than incandescent sources, and have become the mainstream lighting technology in homes, offices, and public places. Still the efficiency of incandescent lamps and fluorescent lamps are limited by some fundamental factors [26]. Continuous increase in the energy demand and limited availability of energy resources make it imperative to save the energy as much as possible in the form of better efficiency lighting devices. Numerous researchers across the globe are trying to develop more energy-efficient light sources. The future of high-efficiency lighting is believed to be in the use of solid state lighting devices in the form of light emitting diodes (LEDs). The replacement of

existing lighting system with LEDs will significantly reduce our dependence on fossil fuels and the contribution to the serious threat of global warming. The high efficiency along with cost effectiveness and environmental benifits makes solid-state lighting a benevolent technology that will benefit humanity at large. In addition to the above advantages, solid-state light sources can be controlled and real-time tuned with much greater precision in terms of a number of characteristics such as the spectral composition, polarization, colour temperature etc., thereby allowing one to custom-tailor the emission properties for specific applications which include imaging and biotechnology, human health, transportation, communications, agriculture, display technology and general lighting [27].

The appearance of an object as perceived by the human eye depends on the nature of illuminating light source. Human eye has receptors for the three primary colors: red, green and blue. Any other color is seen as a mixture of these primary colors. It has been observed that the perception of a color can be achieved by different combinations of light wavelengths. So, two light sources with equal whiteness could be generated from two or more distinctly different combinations of colors. This implies that if a colored object selectively absorbs certain colors, the object might look very different when illuminated with the two different white-light sources. The quality of the white light is determined from its CIE coordinates along with correlated colour temperature (CCT) and colour rendering index (CRI).

The amounts or relative intensities of the three primary colors needed to match a test color in a three-component additive color model are called as

tristimulus values of that color. Any specific method for associating tristimulus values with each color is called a color space. CIE 1931 XYZ, created by the Commission Internationale de l'Eclairage, International Commission on Illumination (CIE) in 1931 is one of many such spaces and is a commonly used standard [28]. In CIE 1931 XYZ color space, tristimulus values are denoted by X, Y and Z, which are sort of derived parameters from the red, green and blue colors, respectively. The chromaticity of a color was then specified by parameters x, y and z, where

$$\begin{aligned} x &= \frac{X}{(X+Y+Z)} \\ y &= \frac{Y}{(X+Y+Z)} \\ z &= \frac{Z}{(X+Y+Z)} \end{aligned} \tag{3.2.1}$$

The three numbers together called a CIE coordinate and represented as (x,y,z), where x + y + z = 1. For representing in a two dimensional paper, we can only plot the x and y axis, where z = 1 - (x + y). Such a plot is called a CIE diagram. By these representations, each color that we see is represented by a single point (x,y) in the CIE diagram; for example an ideal white light corresponds to (0.33, 0.33), as shown in Figure 3.2.1.

Another essential figure of merit for a light source used in illumination applications is color rendering. The perceived color of an object depends not only on the properties of the object but also equally on the illumination source. The ability of a light source to reproduce the colors of various objects faithfully in comparison with an ideal or natural light source is quantitatively measured in terms of color rendering index, CRI. It is calculated

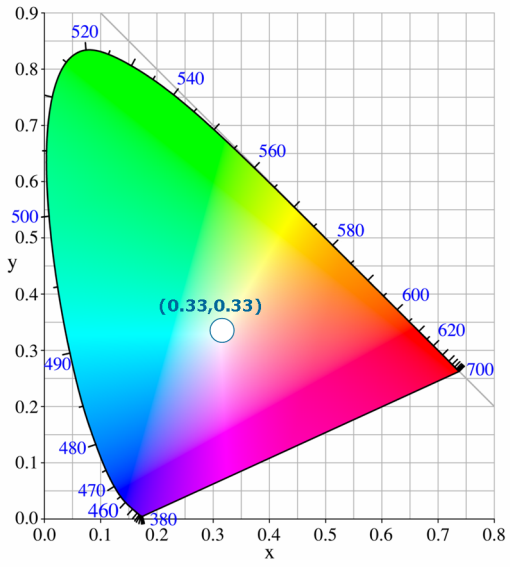

Figure 3.2.1: CIE plot showing the coordinate (0.33,0.33) corresponding to ideal white light.

Table 3.2.1: CIE coordinate, Color rendering index (CRI), Correlated color temperature (CCT) for common light sources (From ref. [29]).

Lamp	x	y	CCT	CRI
High pressure sodium	0.519	0.417	2100K	24
Xenon	0.324	0.324	5920K	94
Tungsten Halogen	0.448	0.407	2856K	100
Daylight	0.313	0.329	6500K	90
Fluorescent,cool white	0.375	0.367	4080K	89
Fluorescent,warm white	0.440	0.403	2940K	72
Incandescent bulb	0.448	0.408	2854K	100

by comparing the color rendering of the test source to that of a standard source. A high CRI value indicates that a light source will accurately render the colors of an object. The correlated color temperature (CCT) of a light source is the temperature of an ideal black-body radiator having the color most closely matching the emission from the light source. For high quality white light, sources with CIE coordinates (0.33,0.33) with a CCT between 2500 and 6500 K and a CRI above 80 are required. Table 3.2.1 gives the CIE coordinate, Color rendering index (CRI), Correlated color temperature (CCT) for common light sources [29].

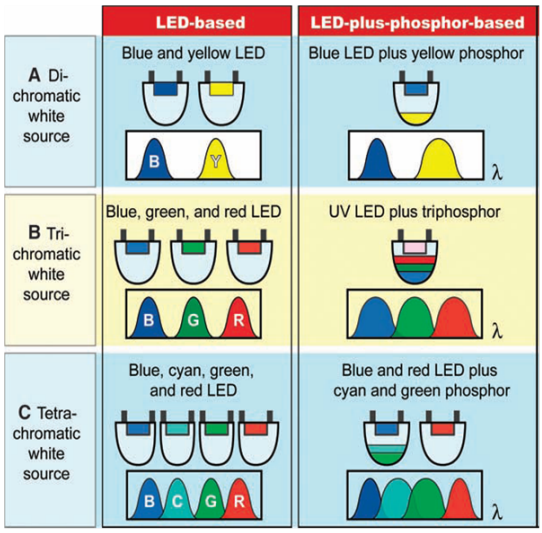

Figure 3.2.2: LED-based and LED-plus-phosphor based approaches for white light sources implemented as di-, tri- and tetrachromatic sources (From [26]).

General strategies employed in solid state lighting to create white light with the use of inorganic sources, organic sources and phosphors are shown in Figure 3.2.2, including di-, tri- and tetrachromatic approaches. The phosphor based white light sources typically contain InGaN or GaN LED that emits

in the blue or ultraviolet region and phosphors to down-convert the energy giving rise to white light [26,30]. GaN has attracted much attention since the development of bright blue light-emitting diodes (LEDs) by Nakamura and coworkers [31]. Ultraviolet or blue lasers as well as high-power-high temperature electronic devices based on GaN have been fabricated [32]. GaN-based optoelectronic devices are fabricated in the form of thin films on different substrates such as sapphire, Si and SiC, using metal-organic vapor phase epitaxy [33], molecular beam epitaxy [34] or metal organic chemical vapor deposition [35,36]. High temperature processing of GaN films makes it difficult for use in applications involving large areas and GaN-based LEDs are, therefore, typically point sources. Figure 3.2.3 shows the emission spectrum from the white LED, where a blue LED is covered with Ce:YAG phosphor.

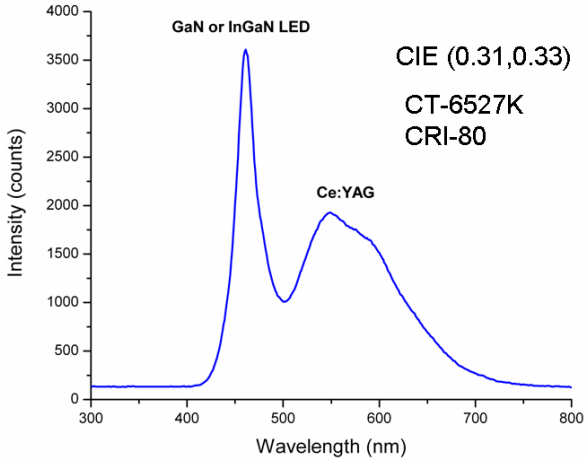

Figure 3.2.3: Emission spectrum from a conventional white LED which is the combination of a blue LED with Ce:YAG phosphor.

Applications such as light emitting diodes in flat panel displays need low cost large scale fabrication. In this regard, the availability of simple routes

to synthesize GaN nanostructures has drawn a great deal of attention. There have been few studies on photoconduction, electroluminescence and negative differential resistance in such GaN nanostructures [37–39]. The decomposition of a single source precursor under refluxing condition provides a method of simple one pot synthesis of GaN nanoparticles [16]. The combination of them with other materials would enable new optical devices and efficient phosphors. In this study we have explored the possible use of nanocomposites based on these GaN nanoparticles as white light phosphors.

White light emitting diodes based on conjugated polymers and small organic molecules can be easily processed over large areas with low-cost as well as flexibility. Such devices are now commercially used in applications such as cellular phones [29, 40–43]. There is a growing interst on the development of hybrid organic LEDs that combine the ease of procesibility of organic molecules with the narrow band efficient luminescence of colloidal quantum dots. LEDs based on nanoparticles of materials such as CdSe and their composites with conjugated polymers have been reported in the literature [44–51]. Cadmium being toxic might seriously limit the application of these devices. GaN nanoparticles being nontoxic and air stable would be ideal for use in such LEDs. GaN based large area LEDs can be fabricated by employing a combination of GaN nanoparticles with conjugated polymers. For this purpose, we have prepared composites of GaN nanoparticles with light emitting conjugated polymers, such as poly(2-methoxy,5-(2-ethylhexoxy)-1,4-phenylenevinylene) (MEHPPV) as well as segmented MEHPPV and investigated their optical properties. We have also fabricated light-emitting diodes based on the MEHPPV-GaN nanoparticle nanocomposite as

the active layer. As an alternative, we have investigated nanocomposites of GaN nanoparticles with nanophosphors in an insulating polymer matrix.

3.2.2 Experimental details

GaN nanoparticles were prepared by a simple route based on the single source precursor, gallium-urea complex $[Ga(H_2NCONH_2)_6]Cl_3$, as reported in the literature [16]. The gallium-urea complex was prepared by dissolving 2 g of Ga_2O_3 in conc.HCl to give $GaCl_3$ and the excess HCl was removed by heating. Urea (15.37 g) and isopropanol (20 ml) were added to the $GaCl_3$ and stirred for two hours. A white precipitate was obtained which was filtered and washed. GaN nanoparticle were obtained by refluxing the gallium urea complex (500 mg) in n-trioctylamine (20 ml) for 24 h. The nanoparticles were precipitated by the addition of isopropanol after cooling the reaction mixture. GaN nanoparticles were also annealed in an ammonia atmosphere at 450 ^oC for 24 h to improve their crystallinity and are designated as annealed GaN nanoparticles. The nanocomposites were prepared by ultrasonically mixing solutions of GaN nanoparticles and the conjugated polymer (MEH-PPV or segmented MEHPPV) in toluene with different weight ratios (see Table 3.2.2). In the case of GaN nanoparticle composites with nanophosphors (ZnS:Cu, ZnS:Mn/ZnO), poly (methyl methacrylate) (PMMA) was used as the polymer matrix (See Table 3.2.3). The nanoparticles and the nanophosphors were dispersed in toluene solution of PMMA by ultrasonic treatment. The nanocomposites was spin coated on clean quartz substrates for photoluminescence measurements. Transmission electron microscope (TEM) images

and selected area electron diffraction(SAED) of GaN nanoparticles were obtained using a JEOL JEM 3010, operating at 300 kV. Powder X-ray diffraction (XRD) patterns were recorded using a Bruker AXS D8 DISCOVER instrument. Photoluminescence measurements were carried out on JobinYvon Flurolog-3 spectrometer. All photoluminescence measurements were carried out with an excitation wavelength of 300 nm. The CIE coordinates, color rendering index and correlated color temperature were calculated from photoluminescence spectrum, using a commercially available software (OL750 Applications).

For the electroluminescence measurements, a device with a configuration of ITO/GaN-MEHPPV/Al was fabricated using spincoating method. The devices were fabricated in a mBraun glove box with the oxygen and water levels at less than 0.1 ppm. Aluminium ($\sim$100 nm) was then thermally evaporated on to the active layer at 10^{-6} Torr using a shadow mask. I-V testing was initially carried out in the glove box. Electroluminescence measurements were carried out using a Keithley SR-236 source meter (for applying the voltage) and the emission was recorded using the Flurolog-3 spectrometer in a helium atmosphere.

3.2.3 Results and discussion

In Figure 3.2.4 and Figure 3.2.5, we show the typical TEM image and x-ray diffraction pattern of as-prepared as well as annealed GaN nanoparticles. The as-prepared GaN nanoparticles show a broad X-ray diffraction pattern due to their small size as can be seen in Figure 3.2.5. The TEM image reveals the presence of nanoparticles with diameters in the 2-4 nm range in

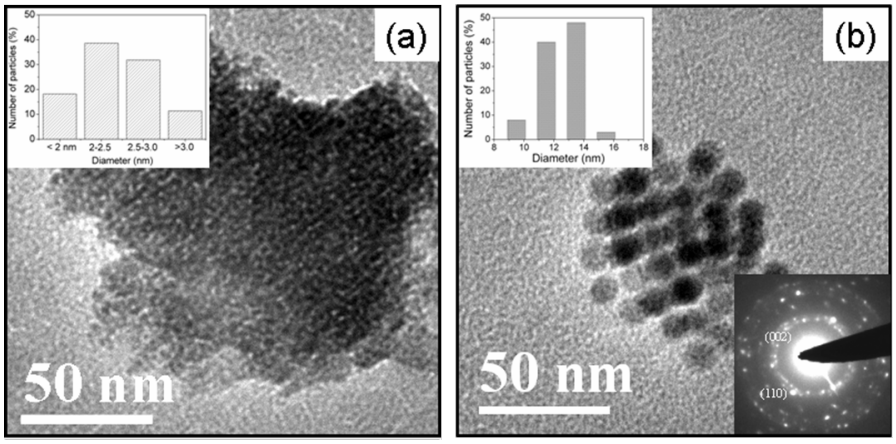

Figure 3.2.4: TEM image of (a) as prepared and (b) annealed GaN nanoparticles. Insets show the particle size distribution. Inset in (b) shows SAED pattern of annealed GaN nanoparticles.

the as-prepared sample. On annealing the nanoparticles at 450 ^{o}C in an ammonia atmosphere, they grow in size (with diameters in the 10-16 nm range). The crystallinity of the sample improves significantly as seen in the X-ray diffraction pattern which corresponds to wurtzite structue of GaN as well as the selected area electron diffraction pattern (inset in Figure 3.2.4b). The as-prepared GaN nanoparticles were found to disperse better in toluene than the annealed GaN nanoparticles.

In Figure 3.2.6, we show the photoluminescence spectra of the various materials used in this study, recorded with 300 nm light as the excitation. GaN nanoparticles exhibit broad blue emission (centered at 415 nm), while the conjugated polymers segmented-MEHPPV and MEHPPV emit greenish yellow (545 nm) and orange (560 nm) light respectively. We have used two nanophosphors, Cu doped ZnS (ZnS:Cu) which emits green light (525 nm) and ZnO coated Mn-doped ZnS (ZnS:Mn/ZnO) which emits red light (600

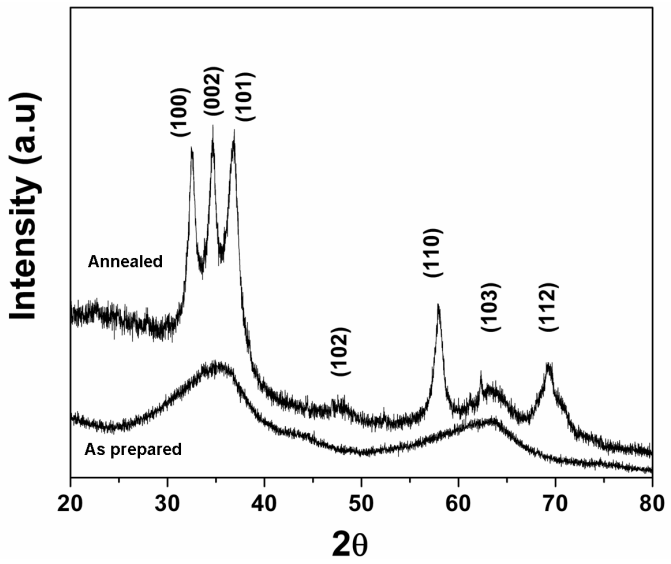

Figure 3.2.5: X-ray diffraction pattern of as prepared and annealed GaN nanoparticles.

nm). In Figure 3.2.7, we show the different chromaticity coordinates of the various starting materials.

In Figure 3.2.8, we show the photoluminescence spectra of the conjugated polymer nanocomposites with as-prepared GaN nanoparticles on excitation with 300 nm light. MEHPPV-GaN nanocomposites yields a CIE coordinate of (0.34, 0.28) as seen in the CIE plot in Figure 3.2.9, with a CCT of 4120 K and a CRI of 72. The light is more towards pinkish white and one can improve the CIE coordinates by the addition of segmented MEHPPV, which emits in the greenish yellow region. We have prepared two different composites with a combination of segmented MEHPPV and MEHPPV. For this purpose, the polymers were mixed together in the 12:1 weight ratio and then mixed with as-prepared GaN nanoparticles. On addition of segmented-MEHPPV, the

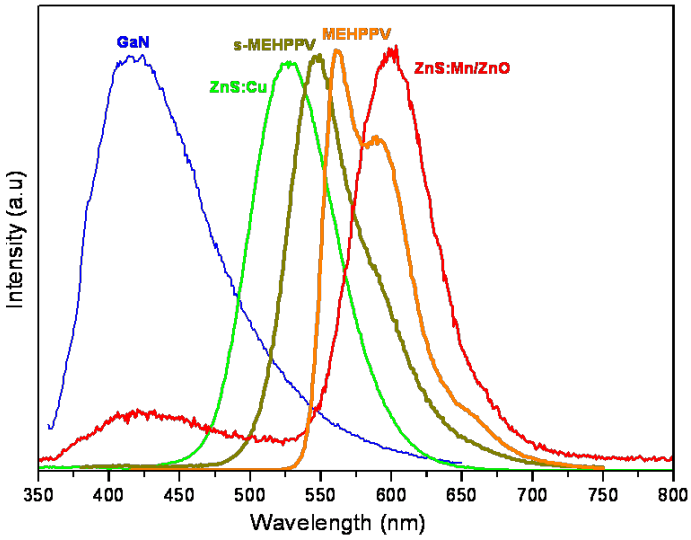

Figure 3.2.6: Photoluminescence spectra of GaN nanoparticles, ZnS:Cu phosphor, segmented MEHPPV, MEHPPV and ZnS:Mn/ZnO phosphor.

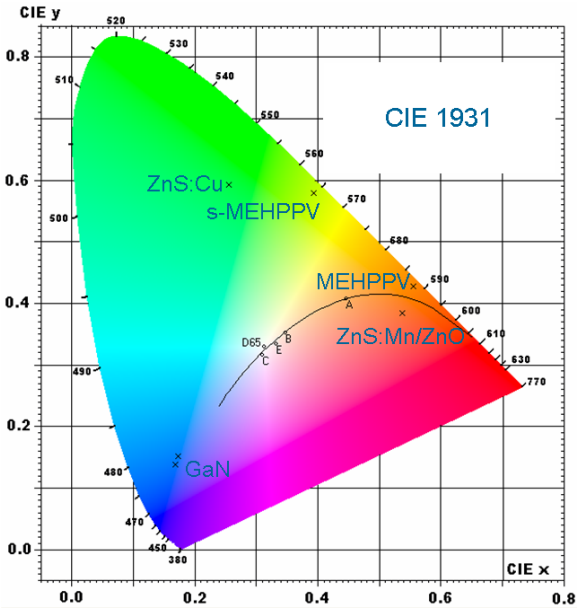

Figure 3.2.7: CIE plot for GaN nanoparticles, ZnS:Cu phosphor, segmented MEHPPV, MEHPPV and ZnS:Mn/ZnO phosphor.

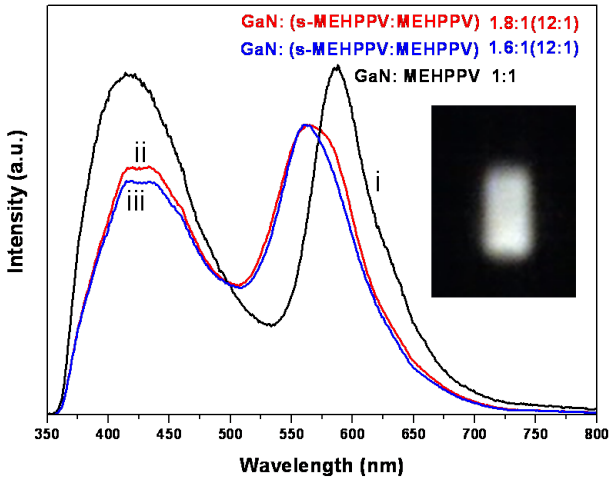

Figure 3.2.8: Photoluminescence spectra of nanocomposites of GaN nanoparticles with (i) MEHPPV, (ii) and (iii) a mixture of segmented MEHPPV and MEHPPV. Inset shows a photograph of the nanocomposite on excitation.

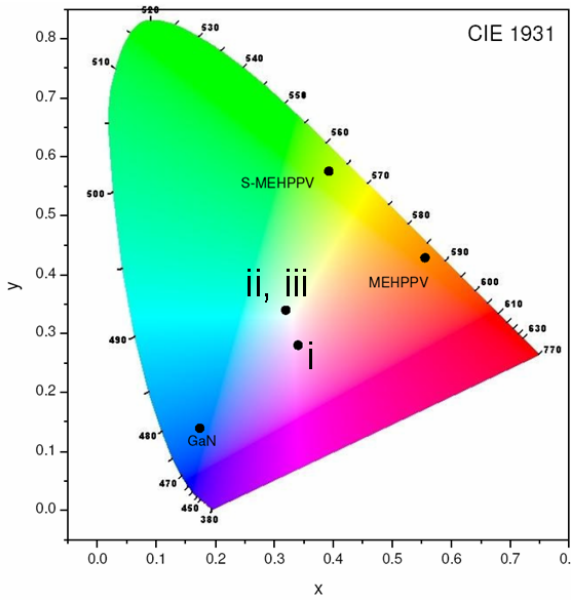

Figure 3.2.9: CIE plot for nanocomposites of GaN nanoparticles with (i) MEHPPV, (ii) and (iii) a mixture of segmented MEHPPV and MEHPPV.

S.No	Composition	x	y	CCT (K)	CRI
i	GaN:MEHPPV [1:1]	0.34	0.28	4120	72
ii	GaN:(s-MEHPPV:MEHPPV)[1.8:1(12:1)]	0.32	0.34	6135	66
iii	GaN:(s-MEHPPV:MEHPPV)[1.6:1(12:1)]	0.32	0.34	6280	65
iv	GaN:MEHPPV [1:1] (electro-luminescence)	0.33	0.33	–	–

Table 3.2.2: CIE coordinates (x,y),Correlated color temperature (CCT) and color rendering index (CRI) for GaN nanoparticle-conjugated polymer nanocomposites.

CIE coordinates of the nanocomposites shift close to (0.33, 0.33) and the CCT increases to above 6000 K. The important features of the GaN-polymer nanocomposites are summarized in Table 3.2.2. The CRI decreases from 72 to 65-66, as there is a loss in the intensity in the red region leading to a poor colour rendering in the red region thus pulling down the overall index. We show a typical photograph of the light emitted by the GaN nanoparticles-conjugated polymer nanocomposite as inset in Figure 3.2.8.

We have carried out electroluminescence studies on the MEHPPV-GaN nanocomposites with the device configuration shown schematically in Figure 3.2.10. The device exhibits a diode like behavior as shown in Figure 3.2.10. Weak electroluminescence, shown as an inset in Figure 3.2.10 was observed when a forward bias of 8 V was applied. The CIE coordinates of the electroluminescence spectrum correspond to (0.33, 0.33). We have also fabricated devices with annealed GaN nanoparticles which showed a behavior similar to that of the as-prepared GaN nanoparticles. Quantum dot-polymers blend based devices have low electroluminescence efficiency because inorganic

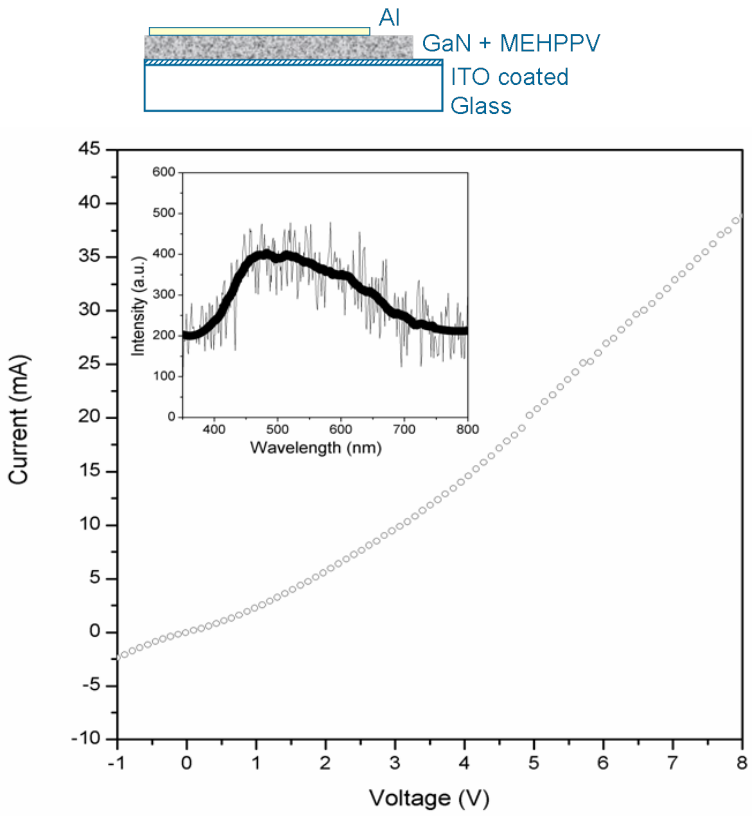

Figure 3.2.10: Schematic diagram of electro-luminescence device and I-V plot of the device. Inset shows the electroluminescence spectra recorded for the device at 8 V.

nanoparticles are poor conductors of electrons and limit the exciton formation [52,53]. Further studies are needed to improve the intensity of light from such devices and are currently underway.

We have combined nanophosphors along with GaN nanoparticles to yield white light. The nanophosphors were combined in different weight ratios and later mixed with GaN nanoparticles with a weight ratio of 1:1 in polymethyl methacrylate (PMMA) (see Table 3.2.3 for more details). Toluene dispersions of PMMA, GaN nanoparticles and nanophosphors were spin-coated

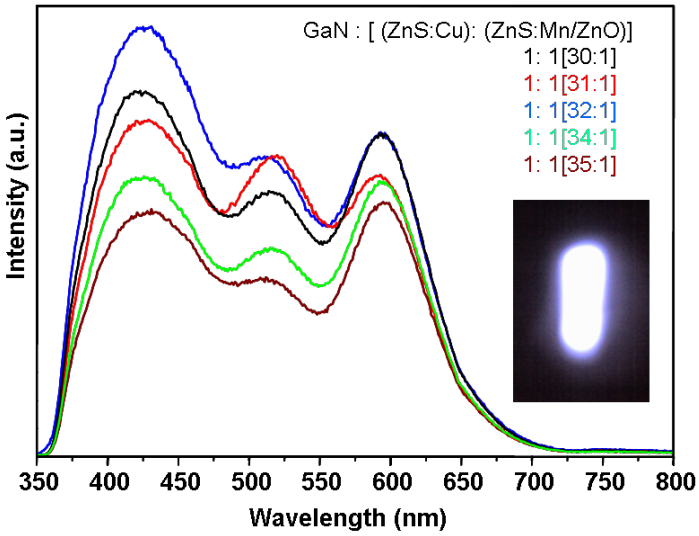

Figure 3.2.11: Photoluminescence spectra of various GaN nanoparticle-phosphor nanocomposites. Inset shows a photograph of the nanocomposite on excitation.

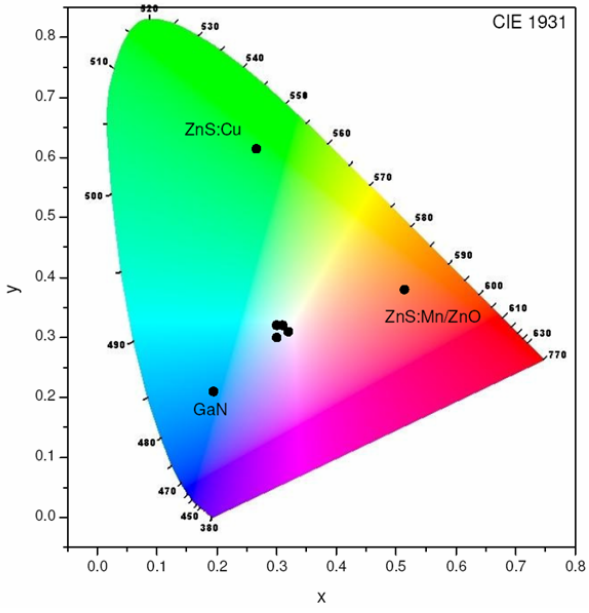

Figure 3.2.12: CIE plot for GaN nanoparticle-phosphor nanocomposites.

S.No	GaN:[(ZnS:Mn/ZnO):(ZnS:Cu)]	x	y	CCT (K)	CRI
i	1:1[30:1]	0.32	0.31	6640	92
ii	1:1[31:1]	0.30	0.32	7310	89
iii	1:1[32:1]	0.30	0.30	8100	93
iv	1:1[34:1]	0.32	0.31	6010	91
v	1:1[35:1]	0.33	0.31	5820	89

Table 3.2.3: CIE coordinates (x,y),Correlated color temperature (CCT) and color rendering index (CRI) for GaN nanoparticle-phosphor nanocomposites.

on to quartz substrates for photoluminescence measurements. In Figure 3.2.11, we show the photoluminescence spectra of the GaN nanoparticles-nanophosphor composites obtained with a 300 nm excitation. Three peaks corresponding to GaN nanoparticles, ZnS:Cu and ZnS:Mn/ZnO are observed in the photoluminescence spectra. Figure 3.2.12 shows the CIE plot of the nanocomposites. All the composites show good white light characteristics with CIE coordinates near (0.33, 0.33), CCT ranging between 5800 and 8100 K and CRI ranging between 89 and 93 as tabulated in Table 3.2.3.

3.2.4 Conclusions

In conclusion, it has been possible to obtain nanocomposites of GaN nanoparticles with conducting polymers as well as with nanophosphors with satisfactory white-light emitting properties. The observed features can be exploited for possible use in practical situations.

References

[1] S. Nakamura, M. Senoh, N. Iwasa, S.-i. Nagahama, *Jpn. J.Appl.Phys.* **34**, L797 (1995).

[2] K. Okamoto, I. Niki, A. Shvartser, Y. Narukawa, T. Mukai, A. Scherer, *Nat.Mater.* **3**, 601 (2004).

[3] W. Van Der Stricht, I. Moerman, P. Demeester, L. Considine, E. J. Thrush, J. A. Crawley, *MRS Internet J.Nitride Semicond.Res.* **2**, 16 (1997).

[4] E. L. Piner, F. G. McIntosh, J. C. Roberts, M. E. Aumer, V. A. Joshkin, S. M. Bedair, N. A. El-Masry, *MRS Internet J.Nitride Semicond.Res.* **1**, 43 (1996).

[5] S. W. Feng, T. Y. Tang, Y. C. Lu, S. J. Liu, E. C. Lin, C. C. Yang, K. J. Ma, C. H. Shen, L. C. Chen, K. H. Kim, J. Y. Lin, H. X. Jiang, *J.Appl.Phys.* **95**, 5388 (2004).

[6] Y. T. Moon, D. J. Kim, J. S. Park, J. T. Oh, J. M. Lee, Y. W. Ok, H. Kim, S. J. Park, *Appl.Phys.Lett.* **79**, 599 (2001).

[7] M. H. Kim, J. K. Cho, I. H. Lee, S. J. Park, *Phys.Status Solidi A* **176**, 269 (1999).

[8] Z. C. Feng, W. Liu, S. J. Chua, J. W. Yu, C. C. Yang, T. R. Yang, J. Zhao, *Thin Solid Films* **498**, 118 (2006).

[9] M. C. Cheung, G. Namkoong, F. Chen, M. Furis, H. E. Pudavar, A. N. Cartwright, W. A. Doolittle, *Phys.Status Solidi C* **2**, 2779 (2005).

[10] C. C. Yang, S.-W. Fengb, Y.-S. Linc, Y.-C. Cheng, C.-C. Liaob, C.-Y. Tsai, K.-J. Mac, J.-I. Chyie, *Proc. SPIE* **4280**, 20 (2001).

[11] V. Lemos, E. Silveira, J. R. Leite, A. Tabata, R. Trentin, L. M. R. Scolfaro, T. Frey, D. J. As, D. Schikora, K. Lischka, *Phys.Rev.Lett.* **84**, 3666 (2000).

[12] B. Damilano, N. Grandjean, S. Dalmasso, J. Massies, *Appl.Phys.Lett.* **75**, 3751 (1999).

[13] L. W. Ji, Y. K. Su, S. J. Chang, L. W. Wu, T. H. Fang, Q. K. Xue, W. C. Lai, Y. Z. Chiou, *Mater.Lett.* **57**, 4218 (2003).

[14] R. C. Tu, C. J. Tun, C. C. Chuo, B. C. Lee, C. E. Tsai, T. C. Wang, J. Chi, C. P. Lee, G. C. Chi, *Jpn. J.Appl.Phys.* **43**, L264 (2004).

[15] K. Sardar, C. N. R. Rao, *Adv.Mater.* **16**, 425 (2004).

[16] K. Sardar, M. Dan, B. Schwenzer, C. N. R. Rao, *J.Mater.Chem.* **15**, 2175 (2005).

[17] K. Sardar, F. Deepak, A. Govindaraj, M. Seikh, C. N. R. Rao, *Small* **1**, 91 (2005).

[18] K. Biswas, K. Sardar, C. N. R. Rao, *Appl.Phys.Lett.* **89**, 2503 (2006).

[19] L. Grocholl, J. Wang, E. G. Gillan, *Chem.Mater.* **13**, 4290 (2001).

[20] K. E. Gonsalves, S. P. Rangarajan, G. Carlson, J. Kumar, K. Yang, M. Benaissa, M. Jos-Yacaman, *Appl.Phys.Lett.* **71**, 2175 (1997).

[21] D. Kirillov, H. Lee, J. S. Harris Jr., *J.Appl.Phys.* **80**, 4058 (1996).

[22] M. Kuball, J. W. Pomeroy, M. Wintrebert-Fouquet, K. S. A. Butcher, H. Lu, W. J. Schaff, *J.Cryst.Growth* **269**, 59 (2004).

[23] A. Tabata, J. R. Leite, A. P. Lima, E. Silveira, V. Lemos, T. Frey, D. J. As, D. Schikora, K. Lischka, *Appl.Phys.Lett.* **75**, 1095 (1999).

[24] R. W. Martin, P. R. Edwards, K. P. O'Donnell, E. G. Mackay, I. M. Watson, *Phys.Status Solidi A* **192**, 117 (2002).

[25] K. P. O'Donnell, T. Breitkopf, H. Kalt, W. Van Der Stricht, I. Moerman, P. Demeester, P. G. Middleton, *Appl.Phys.Lett.* **70**, 1843 (1997).

[26] E. F. Schubert, J. K. Kim, *Science* **308**, 1274 (2005).

[27] E. F. Schubert, J. K. Kim, H. Luo, J. Xi, *Rep. Prog. Phys.* **69**, 3069 (2006).

[28] T. Smith, J. Guild, *Trans.Opt.Soc.* **33**, 73 (1931-32).

[29] B. W. D'Andrade, M. E. Thompson, S. R. Forrest, *Adv.Mater.* **14**, 147 (2002).

[30] E. F. Schubert, *Light Emitting Diodes* (Cambridge University Press, 2003).

[31] S. Nakamura, *Science* **281**, 956 (1998).

[32] S. J. Pearton, F. Ren, *Adv.Mater.* **12**, 1571 (2000).

[33] F. Shahedipour, B. W. Wessels, *Appl.Phys.Lett.* **76**, 3011 (2000).

[34] A. J. Steckl, M. Garter, D. S. Lee, J. Hekenfeld, R. Birkhahn, *Appl.Phys.Lett.* **75**, 8184 (1999).

[35] J. M. Zawada, S. X. Jin, N. Nepal, J. Y. Lin, H. X. Jiang, P. Chow, B. Hertog, *Appl.Phys.Lett.* **84**, 1061 (1994).

[36] K. Wang, R. W. Martin, K. P. O'Donnell, V. Katchkanov, E. Nogales, K. Lorenz, E. Alves, S. Ruffenach, O. Briot, *Appl.Phys.Lett.* **87**, 1 (2005).

[37] D. Kabra, K. Sardar, K. S. Narayan, *Proc. Indian Acad. Sci.* **115**, 459 (2003).

[38] M. Tan, V. Mahalingam, F. C. J. M. vanVeggel, *Appl.Phys.Lett.* **91**, 093132 (2007).

[39] B. Chitara, D. S. I. Jebakumar, C. N. R. Rao, S. B. Krupanidhi, *Nanotechnology* **20**, 405205 (2009).

[40] X. H. Zhang, M. W. Liu, O. Y. Wong, C. S. Lee, H. L. Kwong, S. T. Lee, S. K. Wu, *Chem.Phys.Lett.* **369**, 478 (2003).

[41] K. O. Cheon, J. Shinar, *Appl.Phys.Lett.* **81**, 1738 (2002).

[42] J. Thompson, R. I. R. Blyth, M. Mazzeo, M. Anni, G. Gigli, R. Cingolani, *Appl.Phys.Lett.* **79**, 560 (2001).

[43] G. Cheng, Y. Zha, Y. Zhang, S. Liu, F. He, H. Zhang, Y. Ma, *Appl.Phys.Lett.* **84**, 4457 (2004).

[44] Y. Li, A. Rizzo, R. Cingolani, G. Gigli, *Adv.Mater.* **18**, 2545 (2006).

[45] J. Xu, D. Cui, B. A. Lewis, A. Y. Wang, S. Xu, M. Gerhold, *IEEE Photonics Technol.Lett.* **17**, 2008 (2005).

[46] S. Coe, W.-K. Woo, M. Bawendi, V. Bulovic, *Nature* **420**, 800 (2002).

[47] V. L. Colvin, M. C. Schlamp, A. P. Alivisatos, *Nature* **370**, 354 (1994).

[48] P. O. Anikeeva, J. E. Halpert, M. G. Bawendi, V. Bulovic, *Nano Lett.* **7**, 2196 (2007).

[49] Z. Tan, F. Zhang, T. Zhu, J. Xu, A. Y. Wang, J. D. Dixon, N. Li, Q. Zhang, S. E. Mohney, J. Ruzyllo, *Nano Lett.* **7**, 3803 (2007).

[50] A. H. Mueller, M. A. Petruska, M. Achermann, D. J. Werder, E. A. Akhadov, D. D. Koleske, M. A. Hoffbauer, V. I. Klimov, *Nano Lett.* **5**, 1039 (2005).

[51] N. Tessler, V. Medvedev, M. Kazes, S. Kan, U. Banin, *Science* **295**, 1506 (2002).

[52] C. A. Leatherdale, C. R. Kagan, N. Y. Morgan, S. A. Empedocles, M. A. Kastner, M. G. Bawendi, *Phys.Rev.B* **62**, 2669 (2000).

[53] N. C. Greenham, X. Peng, A. P. Alivisatos, *Phys.Rev.B* **54**, 17628 (1996).

Part 4

Investigations based on ReO_3 nanoparticles

Summary

Surface-enhanced Raman spectra (SERS) of pyridine have been investigated on the surfaces of the metallic Rhenium trioxide (ReO_3) nanoparticles with diameters in the range of 12-32.5 nm. On ReO_3 nanoparticle surfaces, the Raman bands of pyridine generally shift towards lower frequencies, accompanied by enhancement of intensity. The frequency shift does not vary with particle size, but band intensification is highest with the 17 nm nanoparticles. The study establishes how an oxide metal can be employed equally effectively to observe SERS of molecules. On the basis of the success with the study of pyridine, we have extended the study to SERS of pyrimidine and pyrazine on 17 nm ReO_3 nanoparticles.

Papers based on these studies have appeared in Journal of Physical Chemistry C (2007) and Applied Physics Express (2010).

The influence of metallic ReO_3 nanoparticles placed atop silicon photovoltaic devices on absorption and photocurrent generation has been investigated. The nanoparticles improve the power transmission into the semiconductor and consequently photocurrent response at wavelengths corresponding to plasmon absorption. Increase of short circuit current up to 4.5% under simulated solar irradiation was observed experimentally, while gold nanoparticles showed enhancement up to 6.5%.

4.1 Surface-Enhanced Raman Spectra of Aza-aromatics on Nanoparticles of Metallic ReO_3

4.1.1 Introduction

Surface-enhanced Raman spectroscopy has emerged as an important spectroscopic method for surface science, analytical chemistry, physical chemistry, and biophysics because of the enhanced vibrational signals, low detection limits, and good adsorbate selectivity. The magnitude of surface enhancement is affected by factors such as surface roughness, particle size and shape, the nature of the analyte, and wavelength of laser excitation [1–5]. The major contributions to surface-enhanced Raman spectra (SERS) effect are due to the electromagnetic (EM) enhancement associated with large local fields caused by surface plasmon resonance, and chemical enhancement involving a resonance Raman-like process associated with chemical interactions between the molecule and the metal surface. EM enhancement is determined by the interaction of the incident and scattered light and the metal, which depends on the wavelength of the exciting light, the optical electronic property of metal, and surface morphology. Chemical enhancement is determined by chemisorption and the charge-transfer between the adsorbate and the substrate. In most noble metals, EM enhancement plays a dominant role. Since the early measurement of the surface-enhanced Raman spectrum of pyridine adsorbed on an electrochemically roughened Ag electrode by Fleischmann *et*

al. [6], there has been a wide range of studies on Ag [6–14], Au [7,8,15–18] and other metals such as Pt, Ru, Rh, Pd, Fe, Co, and Ni [19–23]. A comparative SERS study of pyridine with different metals has been carried out [24]. In most cases, the enhancement factor is in the range of 10^2-10^7. Large enhancement factors on the order of 10^{14}-10^{15} as well as single molecule SERS have been reported for molecules at the junctions between nanoparticles [25–28].

ReO_3 is a unique oxide metal, which looks like copper and conducts like copper, as a result of a partially filled metal d band [29, 30]. ReO_3 shows a plasmon band like gold around 520 nm in the visible region. The nanoparticles of ReO_3 of different sizes exhibit a size dependence of the plasmon band position [31]. We have examined the SERS of pyridine on ReO_3 nanoparticles of different sizes and obtained the relative enhancement ratios of the adsorbate bands relative to those of the pure liquid [7, 11]. We have found that the values of the relative enhancement ratios on the ReO_3 surface to be comparable to those reported in the literature in the case of nobel metal particles. The enhancement factors are of the order of 10^5-10^6. The bands of the pyridine adsorbed on the ReO_3 nanoparticles are shifted significantly toward lower frequencies due to bonding between the ReO_3 surface and the molecule lying on the surface. SERS effect on ReO_3 nanoparticles is also found with pyrimidine and pyrazine, thereby establishing the oxide metal to be as effective as Au or Ag nanoparticles.

4.1.2 Experimental details

ReO_3 nanoparticles in the diameter range of 12-32.5 nm were prepared by the decomposition of the Re_2O_7-dioxane complex under solvothermal conditions [31]. The synthesis of ReO_3 nanoparticles involves the preparation of the rhenium(VII) oxide-dioxane complex, Re_2O_7-$(C_4H_8O_2)_x$, as the starting material (following the literature procedure [32,33]) and its solvothermal decomposition in toluene to yield the desired nanoparticles. In a typical synthesis, 0.025 g (0.12 mmol) of Re_2O_7 was taken in a 10 ml round-bottomed flask and 0.25 ml (2.93 mmol) of anhydrous 1,4-dioxane was added to it. This mixture was warmed in a water bath maintained at 70 ^{o}C and then frozen in an ice bath alternatively until the rhenium(VII) oxide-dioxane complex (RDC) precipitated out as a dense, pearl gray deposit. The complex was dissolved in 2 ml (30.08 mmol) of ethanol and was taken in 45 ml of toluene and sealed in a Teflon-lined stainless steel autoclave of 80 ml capacity (at 70% filling fraction). It was then heated at 200 ^{o}C for 4 h. The red ReO_3 nanoparticles (12 nm diameter) were washed several times with acetone. To vary the particle size of ReO_3, the concentration of RDC and the reaction temperature were varied, keeping the amount of toluene and the filling fraction of the autoclave constant. Nanoparticles of different diameters were obtained as follows: for 12 nm, RDC dissolved in 2 ml (30.08 mmol)ethanol prepared by 0.025 g (0.12 mmol) of Re_2O_7 and 0.25 ml (2.93 mmol) of dioxane, 200 ^{o}C, 4 h; for 17 nm, RDC dissolved in 2 ml (30.08 mmol) ethanol prepared from 0.05 g (0.24 mmol) of Re_2O_7 and 0.5 ml (5.83 mmol) of dioxane, 200 ^{o}C, 4 h; for 32.5 nm, RDC dissolved in 2 ml (30.08 mmol) ethanol prepared from

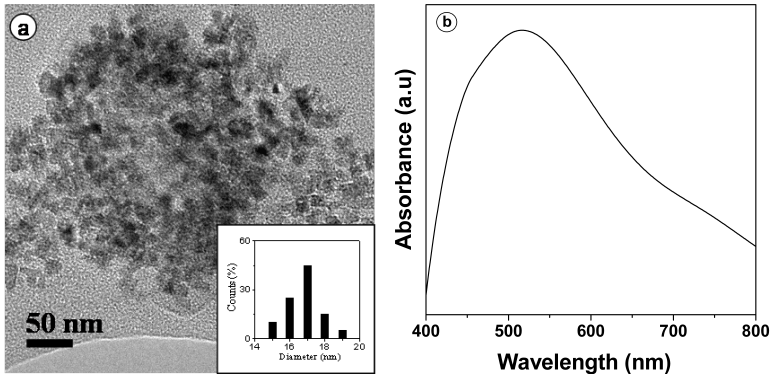

Figure 4.1.1: (a) TEM image of ReO_3 nanoparticles with an average diameter of 17 nm. Inset shows the size distribution histogram. (b)Absorption spectrum of 17 nm ReO_3 nanoparticles.

0.05 g (0.24 mmol) of Re_2O_7 and 0.5 mL (5.83 mmol) of dioxane, 220 ^oC, 4 h. For SERS measurements, we used the pure liquid or 10^{-3} M analyte (pyridine/pyrimidine/pyrazine) solution in milli-Q water. For each measurement, we took 3 mg of the ReO_3 nanoparticles on a clean glass slide in which 5 μL of the liquid anylate (pyridine/pyrimidine/pyrazine) was dropped. Raman spectroscopy was carried out with a LAB RAM HR 800 spectrometer. The excitation wavelength was 632.8 nm.

4.1.3 Results and discussion

We have carried out SERS of pyridine on ReO_3 nanoparticles of three different sizes. The particles had average diameters of 12, 17, and 32.5 nm with plasmon band maxima at 507, 516, and 543 nm, respectively. The band maximum is not that different from that found in Au nanoparticles, but the band is broadly extended over the 400-700 nm regions. In Figure 4.1.1, we show the transmission electron microscope image and the surface plasmon band of

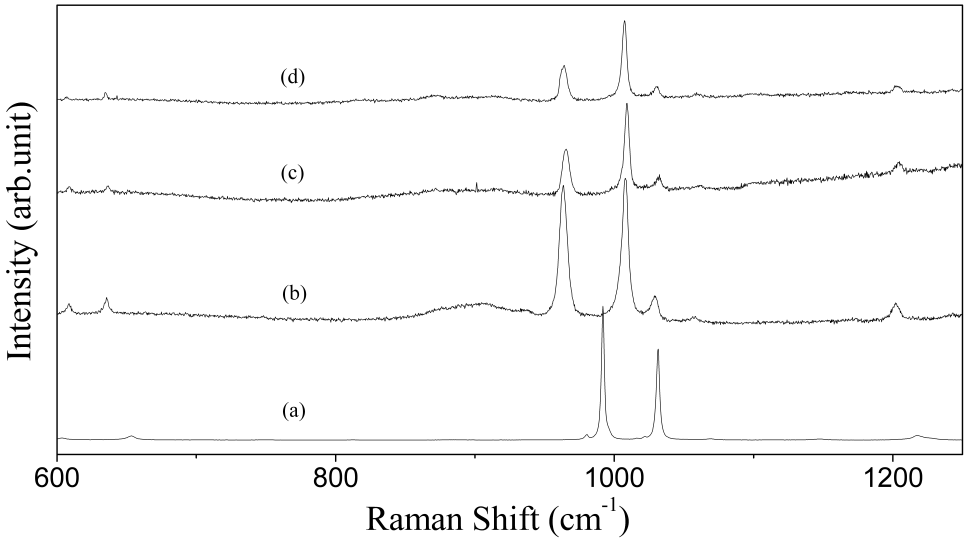

Figure 4.1.2: Raman spectra of pyridine: (a) in liquid state, (b) on 32.5 nm ReO_3, (c) on 17 nm ReO_3 and (d) on 12 nm ReO_3.

the 17 nm nanoparticles to demonstrate the essential features. A first-order Raman spectrum is forbidden for ReO_3. It only shows second-order Raman scattering [34] and we did not find any interference between Raman bands of the adsorbates and ReO_3. Figure 4.1.2 shows the Raman spectra of pyridine on ReO_3 nanoparticles in the 600-1250 cm^{-1} region, along with the spectrum of the pure liquid. On adsorption of pyridine on the ReO_3 nanoparticles, we observe bands at 610 (ν_{6a}, A_1, asymmetric ring breathing), 632 (ν_{6b}, B_2, ring in plane deformation), 962 (ν_1, A_1, symmetric ring breathing), 1006 (ν_{12}, A_1, trigonal ring breathing), 1027 (ν_{18a}, A_1, C-H in plane deformation) and 1201 cm^{-1} (ν_{9a}, A_1, C-H in plane deformation), respectively [24].

In Table 4.1.1 we show the Raman band positions of pyridine on the ReO_3 nanoparticles along with their relative intensities in parentheses. The

data for liquid pyridine are given for the purpose of comparison. From Table 4.1.1, we notice that the 610 cm^{-1} band of pyridine adsorbed on the ReO_3 nanoparticles does not show any significant change in the frequencies compared to pure pyridine, but the other five bands are shifted markedly toward lower frequencies, although all the bands show intensification. Only the band at 1582 cm^{-1} (ν_{8a}) due to ring stretching is shifted to higher frequency. The highest frequency shifts are found in the case of the 1068 (ν_{18a}, C-H in plane deformation), 991 (ν_1, symmetric ring breathing), and 1582 cm^{-1} (ν_{8a}, ring stretching) bands of pyridine, while the highest SERS intensification is found in the case of the shifted 1031 cm^{-1} (ν_{12a}, trigonal ring breathing) band.

The frequency of the ring breathing mode ν_1 is sensitive to weak σ donation and large σ/π back-donation. In the case of Au, Cu, and other transition metals, the ν_1 mode is shifted to higher frequencies, with the pyridine molecule adsorbed on the metal in the end-on configuration (binding by nitrogen lone pair) [15, 24]. On the basis of the available data, we are not able to fully explain the frequency shifts of Raman bands of pyridine adsorbed on ReO_3 nanoparticles. We, however, suggest that the molecule could be in the flat-on configuration, or possibly making a small angle with respect to the surface. If the molecule lies flat on the metal surface, the ring breathing mode is expected to be lowered relative to that of the free pure molecule [15]. Such a behavior has been observed in the SERS of flat-adsorbed benzene on Ag [35]. The ring breathing mode of adsorbed benzene occurs at 982 cm^{-1}, compared to 992 cm^{-1} in liquid benzene [35]. In the present case, there is little doubt that there is significant bonding interaction between pyridine and the ReO_3 surface, but we are not able to decide on the symmetry of the

Table 4.1.1: Raman band positions (in cm^{-1}) and relative enhancement ratios of pyridine.

Liquid pyridine Peak position (rel.inten.)	ν^a	On 32.5nm ReO_3		On 17nm ReO_3		On 12nm ReO_3	
		Peak position (rel.inten.)	R^b	Peak position (rel.inten.)	R^b	Peak position (rel.inten.)	R^b
608,A_1(6)	6a	610(10)	1.7	610(15)	2.5	610(11)	1.8
650,B_2(8)	6b	632(15)	2	634(19.2)	2.4	634(19)	2.3
991,A_1(100)	1	962(100)	1	962(100)	1	962(100)	1
1031,A_1(69)	12	1006(106)	1.9	1006(182)	2.7	1007(205)	2.9
1068,A_1(5)	18a	1027(20)	4	1027(33)	6.6	1027(29)	5.8
1214,A_1(8)	9a	1201(14)	1.8	1201(26)	3.3	1201(19)	2.4
1582,A_1(4)	8a	1628(6)	1.5	1628(9)	2.3	1628(22)	5.5

[a] ν = Wilson number.
[b] R = Relative enhancement ratio.

surface complex at present. The resonance Raman charge-transfer process itself, however, would involve the resonance transfer of electron from metal to vacant orbitals of adsorbate and the subsequent emission of Raman photon from the vibrationally excited molecule.

We have measured the relative enhancement ratio, R, defined as the relative intensity of the Raman band of pyridine adsorbed on the ReO_3 nanoparticles divided by the relative intensity of corresponding band of pyridine in the liquid state. From Table 4.1.1, we see that R varies between 1.7 and 6.6, depending on the particle size. We observe maximum values of the enhancement ratios of the pyridine bands with the 17 nm ReO_3 nanoparticles. Comparable values of R for pyridine adsorbed on Ag and Au are reported

Table 4.1.2: Selected Raman band positions (in cm^{-1}) and enhancement factors of pyridine.

Liquid pyridine Peak position (rel.inten.)	ν^a	On 32.5nm ReO_3		On 17nm ReO_3		On 12nm ReO_3	
		Peak position (rel.inten.)	EF[b]	Peak position (rel.inten.)	EF[b]	Peak position (rel.inten.)	EF[b]
608(6)	6a	610(10)	1.90 x 10^5	610(15)	2.67 x 10^5	610(11)	3.05 x 10^5
1031(69)	12	1006(106)	1.43 x 10^4	1006(182)	1.96 x 10^5	1007(205)	2.68 x 10^5
1214(8)	9a	1201(14)	3.34 x 10^4	1201(26)	4.41 x 10^5	1201(19)	4.60 x 10^5

[a] ν = Wilson number.
[b] EF = Enhancement factor.

in the literature [24]. The highest R is found in the case of the 1027 cm^{-1} (ν_{18a}, A_1) band of adsorbed pyridine. A quantitative explanation for the spectral differences (intensity and frequency) on the different metal surfaces, for example ReO_3 compared to Ag or Au, is difficult to provide at present. It is known that the vibrational spectral features of adsorbate can vary from one surface to another. Thus, the intensity of the ν_{12} band, which is the second strongest band of pyridine in liquid and gas phases, is high on Ag, but weak on Au and Cu [24]. On ReO_3, the ν_{12} band is more intense than the ν_1 band. The potential energy distribution of the ν_{12} mode appears to vary significantly for metals with different Fermi levels. We have calculated the surface enhancement factor (EF) for pyridine molecules adsorbed on ReO_3 nanoparticles by using the following equation [2, 18]:

$$EF = (\frac{I_{SERS}}{I_{bulk}})(\frac{N_{bulk}}{N_{ads}}) \tag{4.1.1}$$

where I_{SERS}, I_{bulk}, N_{bulk}, and N_{ads} represent the measured SERS intensity for adsorbed pyridine molecules on ReO_3 nanoparticles, normal Raman intensity from liquid pyridine, the number of the probe molecules under laser illumination for the bulk sample, and the number of probe molecules on the ReO_3 surface, respectively. N_{ads} is calculated from the average radius of ReO_3 nanoparticles, the surface density of the adsorbate molecule, the area of the laser spot, and surface coverage of ReO_3 nanoparticles. To calculate EF, we use the value of the monolayer surface density of pyridine [15] on Au as 4 x 10^{-10} mol/cm^2. N_{bulk} was obtained from area of the laser spot, the penetration depth, the density of the analyte, and the molecular weight of the analyte. The value of N_{bulk} for pyridine is 2.45 x 10^{-13} mol.

The values of EF calculated for the ν_{6a}, ν_{12}, and ν_{9a} bands of pyridine adsorbed on the 12, 17, and 32.5 nm ReO_3 nanoparticles are listed in Table 4.1.2. A similar EF for adsorbed pyridine on Ag colloidal nanospheres is reported,the values being around of 106, 104, and 102 for 5, 50, and 500 nm of Ag colloids, respectively [9]. Fleischmann *et al.* [6] reported EF of the order of 106 for pyridine on an electrochemically roughened Ag electrode. Orendorff *et al.* [8] have observed EF's for 4-mercaptopyridine on 31 nm Au nanoparticles and 34 nm Ag nanoparticles, which are 1.2 x 10^4 and 4.8 x 10^6, respectively. In all the cases, the EF decreases with the increase in particle size. SERS-active systems must ideally possess structures in the 5-100 nm range [3]. Likewise, the dimensions of the active structure cannot be much smaller than a lower bound. The upper bound of the SERS-active system is determined by the wavelength. For a given metal system, the SERS intensity is optimal when the particle size is small with respect to the wavelength of

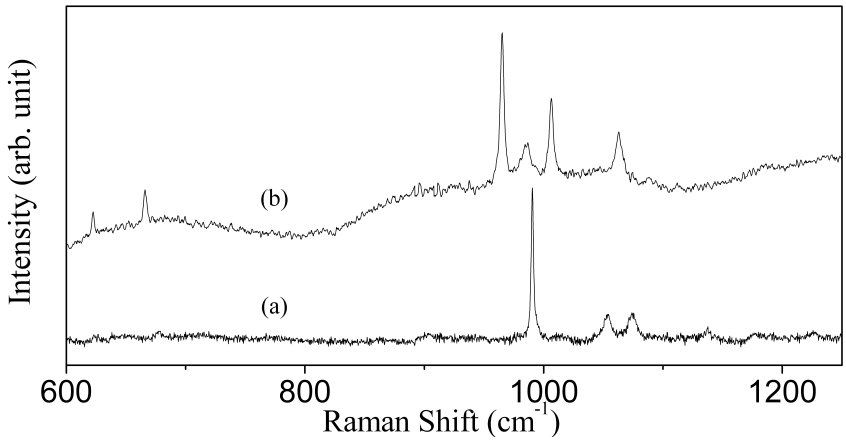

Figure 4.1.3: Raman spectra of pyrimidine: (a) in liquid state, (b) on 17 nm ReO_3.

exciting light as long as the size is not much smaller than the electronic mean free path of the conduction electrons [3].

The results discussed hitherto clearly demonstrate how ReO_3 nanoparticles can be effectively used to investigate SERS of pyridine. We have extended the SERS study to pyrimidine and pyrazine. Figure 4.1.3 shows the Raman spectrum of pyrimidine on the 17 nm ReO_3 nanoparticles along with that of the pure liquid. On adsorption of pyrimidine on ReO_3, we observe bands at 620 (ν_{6b}, B_2, ring in-plane deformation), 666 (ν_{6a}, A_1, ring in-plane deformation), 965 (ν_1, A_1, ring stretching), 986 (ν_5, B_1, C-H out-of-plane deformation), 1010 (Fermi resonance, A_1), and 1060 cm^{-1} (ν_{12}, A_1, ring stretching) [36].

In Table 4.1.3, we show the Raman band positions of pyrimidine and the relative intensities in parentheses. Adsorbed pyrimidine bands are shifted to the lower frequencies compared to the bands of liquid pyrimidine, due to bonding between the adsorbed molecule and the ReO_3 surface. The highest

Table 4.1.3: Raman band positions (in cm^{-1}), relative enhancement ratios and enhancement factors of pyrimidine.

Liquid pyrimidine Peak position (rel.inten.)	On 17nm ReO_3			
	Peak position (rel.inten.)	R[a]	EF[b]	ν[c]
624,B_2(6)	620(17)	2.8	3.6 x 10^5	6b
675,A_1(6)	666(25)	4.2	5.5 x 10^5	6a
991,A_1(100)	965(100)	1	1.3 x 10^5	1
	986,B_1(19)			5
1053,A_1(14)	1010(56)	4	5.4 x 10^5	(10b+16b)FR
1075,A_1(16)	1060(29)	1.8	3.1 x 10^5	12

[a] R = Relative enhancement ratio.
[b] EF = Enhancement factor.
[c] ν = Wilson number.

frequency shifts are found in the case of 1053 (ν_{12}, ring stretching) and 991 cm^{-1} (ν_1, ring stretching) bands of pyrimidine on the ReO_3 nanoparticles. We also observe a new band at 986 cm^{-1} (ν_5, C-H out-of-plane deformation). We have enlisted the relative enhancement ratios of the adsorbed pyrimidine bands in Table 4.1.3. The value of R varies between 1.8 and 4.2. Comparable values of R for pyrimidine adsorbed on Ag sols are reported in the literature [11] The intensities of the A_1 type bands are generally higher, as also the values of R. The bands of the A_2 species are either absent or weak. We have estimated the enhancement factor for the Raman bands of pyrimidine using the same procedure employed for pyridine and listed them in Table 4.1.3. The value of N_{bulk} for pyrimidine is 2.52 x 10^{-13} mol. Centeno *et al.* [36], on the basis of their experiments and calculations, propose perpendicular orientation

of pyrimidine on the Ag surface (end-on), with the surface complex having C_s symmetry. The red shifts of the band observed by us, however, seem to favor a flat-on configuration for the pyrimidine molecule.

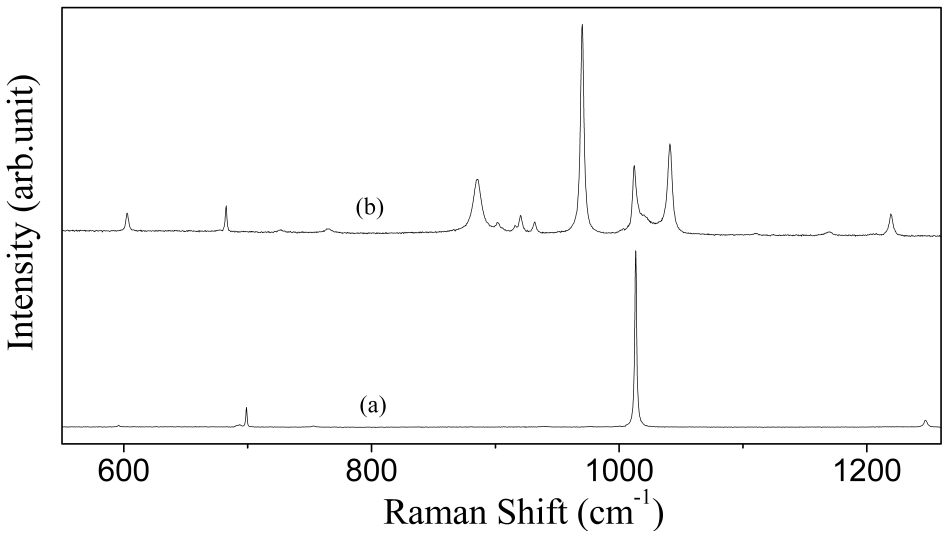

Figure 4.1.4: Raman spectra of pyrazine: (a) in liquid state, (b) on 17 nm ReO_3.

Figure 4.1.4 shows the Raman spectra of liquid pyrazine solution and of that adsorbed on 17 nm ReO_3 nanoparticles. In Table 4.1.4, we show the Raman band positions of pyrazine and the relative intensities in parentheses. Raman bands of adsorbed pyrazine are also at lower frequencies than the bands of liquid pyrazine solution, suggesting the pyrazine molecule is likely to have a flat-on orientation on the ReO_3 surface. The highest frequency shift is in the case of the 1015 cm^{-1} (ν_1, ring breathing) band of pyrazine. Only the band at 1580 cm^{-1} (ν_{8a}, ring streching) is shifted to higher frequency. We observe new bands belonging to the B_{1u}, B_{2u}, B_{3u}, and B_{3g} species. Thus, the bands at 765 (B_{3u}), 1012 (B_{1u}) ,1042 (B_{2u}), and 1169 cm^{-1} (B_{1u}) are

Table 4.1.4: Raman band positions (in cm^{-1}), relative enhancement ratios and enhancement factors of pyrazine.

Liquid pyrazine Peak position (rel.inten.)	On 17nm ReO_3			
	Peak position (rel.inten.)	R[a]	EF[b]	ν[c]
594,A_g(1.1)	602(8.9)	8.1	6.6 x 10^7	6a
693(0.9)	677(1.08)	1.2		
700,B_{2g}(11.7)	682(12.5)	1.1	4.3 x 10^5	4
752,B_{1g}(0.8)	726(1.5)	1.9	7.9 x 10^5	10a
	765,B_{3u}(2)			11
	885(26)			
930,B_{2g}(0.6)	901(4.8)	8	4.1 x 10^7	5
	920(7.8)			
	932(4.6)			
1015,A_g(100)	970(100)	1	3.5 x 10^5	1
	1012,B_{1u}(30)			12
	1042,B_{2u}(44)			15
	1110,B_{3g}(1.1)			
	1169,B_{1u}(1.7)			18a
1243,A_g(4.5)	1219(10)	2.3	1.9 x 10^6	9a
1580,A_g(1.05)	1589(6.2)	5.9	2.3 x 10^6	8a

[a] R = Relative enhancement ratio.
[b] EF = Enhancement factor.
[c] ν = Wilson number.

Raman forbidden and IR-active. The appearance of Raman forbidden bands in the spectra of the adsorbed molecule is probably due to the break down of selection rules. Dornhaus *et al.* [10] have shown that pyrazine adsorbed on an Ag electrode exhibits all IR-active modes in the SERS spectrum. The presence of Raman forbidden bands in the SERS spectrum of pyrazine on Ni electrodes has been observed by Huang *et al.* [21]. Erdheim *et al.* [37] propose that when pyrazine is adsorbed on a metal surface, the symmetry of the molecule is lowered from D_{2h} to C_{2v} by the removal of the inversion element. This would change the Raman forbidden modes into active modes. The value of R for pyrazine varies between 1.1 and 8.1. Comparable values of R for pyrazine adsorbed on Ag sols are reported in the literature [11]. The values of R are high for bands of the A_g and B_{2g} species. We have calculated the enhancement factors for Raman bands of adsorbed pyrazine and listed them in Table 4.1.4. To calculate EF, the value of N_{bulk} for pyrazine is used as 2.57 x 10^{-13} mol.

4.1.4 Conclusions

We have observed SERS of aza-aromatics on nanoparticles of an oxide metal for the first time. Thus, we observe large shifts of the bands of pyridine toward the lower frequencies on adsorption of the molecules on the ReO_3 nanoparticle surface. The observed SERS effect suggests that there is bonding interaction between the metallic ReO_3 surface and the adsorbed molecules. We observe enhancement of Raman signal intensities on ReO_3 nanoparticle surfaces comparable to those on noble metals. On the basis of the spectral

features, we are unable to decide on the exact geometry of the adsorbed pyridine on ReO_3 surfaces, although the red shifts of the bands are indicative of a flat-on configuration. Preliminary studies of pyrimidine and pyrazine adsorbed on ReO_3 nanoparticles also show SERS effect similar to pyridine. In the case of adsorbed pyrazine, we observe the appearance of new bands, some of which are IR-active.

4.2 Effect of metallic ReO_3 nanoparticles on the performance of Si solar cell

4.2.1 Introduction

Commercially available crystalline Si solar cells, which currently dominate the photovoltaics market, typically possess power conversion efficiencies in the range of 10-20%. As potential routes to improving the performance of photovoltaic devices, there is extensive interest in light trapping and manipulation techniques such as antireflection coatings (ARCs), surface texturing and increasing the optical path length for thin photovoltaic films *etc.* [38]. Surface plasmon resonances in metallic nanoparticles are currently being exploited for a variety of applications employing the large electromagnetic field enhancement near the surface of the nanoparticle. The excitation of surface plasmons in metal nanoparticles placed on a semiconductor might enhance the optical absorption of incident photons within the semiconductor region near each nanoparticle. The optical absorption enhancement via scattering from metallic nanoparticles is a recently developed light-trapping technique for semiconductor devices such as solar cells [39–44].

Several studies report measurable photocurrent enhancement for silicon-on insulator photodiode structures [39, 40], hydrogenated amorphous Si thin film cells [42, 45], crystalline Si p-n photodiodes [41, 44] and organic bulk heterojunction solar cells [46] using gold or silver metal nanostructures. The design principles for plasmonic solar cells with broadband absorption enhancement are being developed [47–49]. Metallic ReO_3 nanoparticles, exhibiting

the plasmon absorbance like gold around 520 nm in the visible region, have been shown to be SERS active (See section 4.1). Here, we present the study of the effect of these metallic nanoparticles on the photocurrent generation in silicon solar cells. The experiment has been carried out with gold nanoparticles as well for the purpose of comparison.

4.2.2 Experimental

The solar cell devices used in our experiments consisted of crystalline Si p-n juncton with frontside surface texturing and without antireflection coating, obtained from Bharat Electonics Ltd. A 100 nm thick gold layer was coated on the top as the contanct by thermal evaporation. Aqueous solutions of colloidal Au nanoparticles were syntheised following the reported procedure [50]. ReO_3 nanopaticles were prepared by the decomposition of the Re_2O_7-dioxane complex under solvothermal conditions [31] and ultrasonically dispersed in toulene. Au or ReO_3 colloidal particle solution was drop coated onto the sample and then blown dry with nitrogen. The divice structure with deposited metallic nanoparticles is shown schematically in Figure 4.2.1. Field emission scanning electron microscope (FESEM) images were recorded with a FEI NOVA NANOSEM 600, to observe the nanoparticles deposited onto the devices. To measure the photocurrent response, samples were illuminated at normal incidence using a xenon lamp through a monochromator (TRIAX 180, JOBIN YVON). For measurements at wavelengths of 600 nm and longer, a red filter was employed to eliminate illumination from the second-order diffraction line. Current-voltage (I-V) characteristics were obtained, either in the dark or under illumination from a 300 W Newport Solar

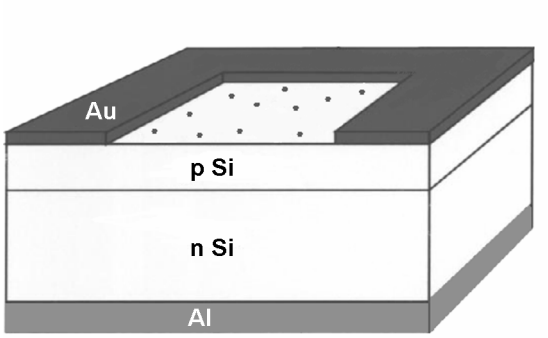

Figure 4.2.1: Schematic diagram of the Si p-n junction solar cell with metallic nanoparticles deposited on the device surface.

Simulator with a global AM 1.5 direct filter, using a Keithley 236 source measure unit.

4.2.3 Results and discussion

Figure 4.2.2 (a) and (b) show the FESEM images of Au nanoparticles and ReO_3 nanoparticles deposited onto the devices. The density of Au nanoparticles was approximately 4.1 x 10^8 cm^{-2} as estimated from the FESEM image. Although Au nanoparticles are present predominantly as isolated single particles, ReO_3 nanoparticles show significant clustering and can be seen as multiparticle clusters. The density of ReO_3 nanoparticles on the device surface can be estimated to be in the range of 10^9 cm^{-2} from the FESEM image. Figure 4.2.3 shows measured I-V characteristics under AM 1.5 illumination for devices with ReO_3 nanoparticles. Inset shows the I-V characteristics for Au nanoparticles. Clear increase in I_{sc} are observed in the presence of nanoparticles with the increase being 6.5% and 4.5% for Au and ReO_3

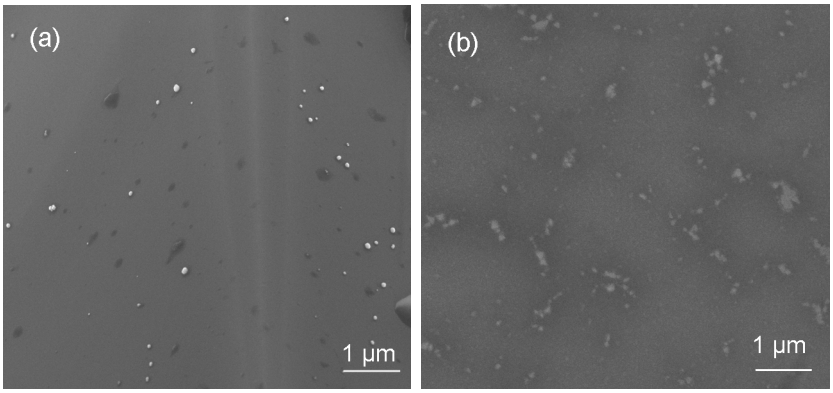

Figure 4.2.2: Field emission Scanning Electron Micrographs of (a) Au and (b) ReO_3 nanoparticles deposited on Si solar cell surfaces.

nanoparticles respectively. An increase in the short circuit current leads directly to an increase in the power conversion efficiency η = FF x I_{sc} x V_{oc} / P_{in}, where FF, I_{sc}, V_{oc}, and P_{in} are the fill factor, short circuit current, open circuit voltage, and input power respectively. Small changes in the V_{oc}, fill factor and maximum power were observed in the measurements from sample to sample, most likely due to the non-ideal nature of the commercial grade cells.

Figure 4.2.4 shows experimentally observed photocurrent response spectra for devices on which ReO_3 nanoparticles have been deposited along with that of the same device prior to nanoparticle deposition. Inset shows the photocurrent response spectra for the case of Au nanoparticles. The correspondence between the plasmon absorption peaks and the photocurrent response peaks is clear evidence of the role of the nanoparticle plasmon resonances in the observed photocurrent response. At the plasmon resonance wavelengths, increase in photocurrent response relative to that of the Si solar

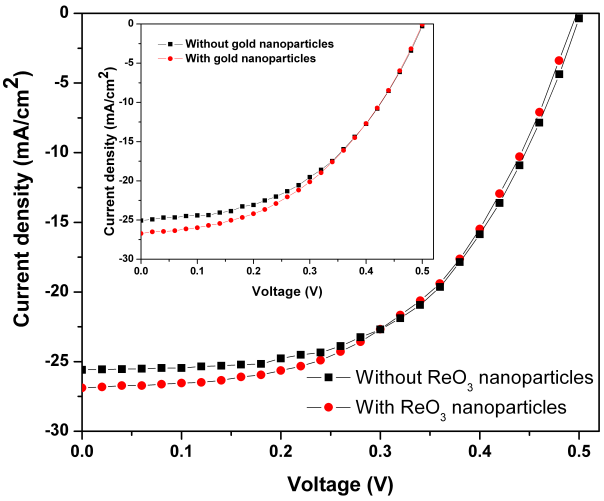

Figure 4.2.3: I-V characteristics, under AM 1.5 illumination, for silicon solar cell before and after deposition of ReO_3 , Au (inset) nanoparticles.

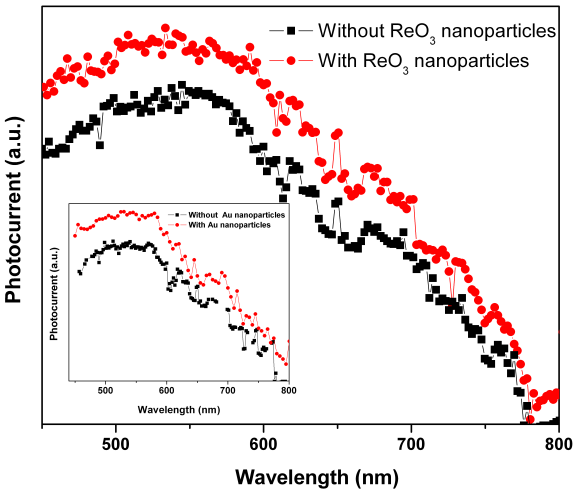

Figure 4.2.4: Photocurrent response as a function of illumination wavelength for Si solar cell in the absence of nanoparticles and with ReO_3, Au (inset) nanoparticles.

cell were $\sim$ 8.5 % and 14% for ReO_3 and Au nanoparicles respectively. Considerably larger increases may be possible at greater nanoparticle densities and by avoiding the nanoparticle clustering.

The observed enhancement in I_{sc} of Si p-n junction device for gold nanoparticles is higher than the values reported in the literature (1- 3 %) [44]. The reported values for enhancement of photocurrent in plasmonic solar cells vary significantly. The systematic research to investigate the optimum particle parameters varying the shape, size, particle material and dielectric environment for plasmon enhanced light trapping is yet to be done [47]. However, the resulting increase in photocurrent is smaller than that achievable with conventional ARC technologies for crystalline silicon solar cells. The nanoparticle-based scattering for light trapping may be beneficial for organic semiconductor devices, where it is difficult to employ traditional antireflection coatings [44, 46].

4.2.4 Conclusions

In conclusion, enhancement in short circuit current up to 4.5% has been measured for crystalline Si photovoltaic devices for ReO_3 nanoparticle based scattering, compared to the 6.5% enhancement in the case of Au nanoparticles. Increased photocurrent generation is observed at wavelengths corresponding to the plasmon absorption of metallic nanoparticles.

References

[1] R. K. Chang, T. E. Furtak, *Surface Enhanced Raman Scattering* (Plenum Press,New York, 1982). Cited By (since 1996): 712.

[2] Z. Q. Tian, B. Ren, D. Y. Wu, *J.Phys.Chem.B* **106**, 9463 (2002).

[3] M. Moskovits, *J.Raman Spectrosc.* **36**, 485 (2005).

[4] K. Kneipp, H. Kneipp, I. Itzkan, R. R. Dasari, M. S. Feld, *Chem.Rev* **99**, 1957 (1999).

[5] C. J. Orendorff, A. Gole, T. K. Sau, C. J. Murphy, *Anal.Chem.* **77**, 3261 (2005).

[6] M. Fleischmann, P. J. Hendra, A. J. McQuillan, *Chem.Phys.Lett.* **26**, 163 (1974).

[7] C. Lee, S. J. Bae, M. Gong, K. Kim, S. W. Joo, *J.Raman Spectrosc.* **33**, 429 (2002).

[8] C. J. Orendorff, L. Gearheart, N. R. Jana, C. J. Murphy, *Phys.Chem.Chem.Phys.* **8**, 165 (2006).

[9] M. Kerker, *Pure Appl.Chem* **56**, 1429 (1984).

[10] R. Dornhaus, M. B. Long, R. E. Benner, R. K. Chang, *Surf.Sci.* **93**, 240 (1980).

[11] M. Miranda, N. Neto, G. Sbrana, *J.Phys.Chem.* **92**, 954 (1988).

[12] H. H. Wang, C. Y. Liu, S. B. Wu, N. W. Liu, C. Y. Peng, T. H. Chan, C. F. Hsu, J. K. Wang, Y. L. Wang, *Adv.Mater.* **18**, 491 (2006).

[13] A. M. Michaels, M. Nirmal, L. E. Brus, *J.Am.Chem.Soc.* **121**, 9932 (1999).

[14] K. A. Bosnick, J. Jiang, L. E. Brus, *J.Phys.Chem.B* **106**, 8096 (2002).

[15] A. G. Brolo, D. E. Irish, J. Lipkowski, *J.Phys.Chem.B* **101**, 3906 (1997).

[16] N. Felidj, S. L. Truong, J. Aubard, G. Lvi, J. R. Krenn, A. Hohenau, A. Leitner, F. R. Aussenegg, *J.Chem.Phys.* **120**, 7141 (2004).

[17] X. C. Yang, Y. Fang, *J.Phys.Chem.B* **107**, 10100 (2003).

[18] Z. Zhu, T. Zhu, Z. Liu, *Nanotechnology* **15**, 357 (2004).

[19] B. Ren, Q. J. Huang, W. B. Cai, B. W. Mao, F. M. Liu, Z. Q. Tian, *J.Electroanal.Chem.* **415**, 175 (1996).

[20] J. S. Gao, Z. Q. Tian, *Spectrochim.Acta* **53**, 1595 (1997).

[21] Q. J. Huang, J. L. Yao, B. W. Mao, R. A. Gu, Z. Q. Tian, *Chem.Phys.Lett.* **271**, 101 (1997).

[22] P. G. Cao, J. L. Yao, B. Ren, B. W. Mao, R. A. Gu, Z. Q. Tian, *Chem.Phys.Lett.* **316**, 1 (2000).

[23] D. Y. Wu, Y. Xie, B. Ren, J. W. Yan, B. W. Mao, Z. Q. Tian, *Phys.Chem.Commun.* **18**, 1 (2001).

[24] C. Zuo, P. W. Jagodzinski, *J.Phys.Chem.B* **109**, 1788 (2005).

[25] S. Nie, S. R. Emory, *Science* **275**, 1102 (1997).

[26] J. Jiang, K. Bosnick, M. Maillard, L. Brus, *J.Phys.Chem.B* **107**, 9964 (2003).

[27] H. Xu, E. J. Bjerneld, M. Kall, L. Borjesson, *Phys.Rev.Lett.* **83**, 4357 (1999).

[28] A. M. Michaels, J. Jiang, L. Brus, *J.Phys.Chem.B* **104**, 11965 (2000).

[29] C. N. R. Rao, B. Raveau, *Transition Metal Oxides* (Wiley-VCH,Weinheim, Germany, 1995).

[30] A. Ferretti, D. B. Rogers, J. B. Goodenough, *J.Phys.Chem.Solids* **26**, 2007 (1965).

[31] K. Biswas, C. N. R. Rao, *J.Phys.Chem.B* **110**, 842 (2006).

[32] H. Nechamkin, A. N. Kurtz, C. F. Hiskey, *J.Am.Chem.Soc.* **73**, 2828 (1951).

[33] L. F. Audrieth, *Inorg.Synth.* **3**, 187 (1950).

[34] M. Ishii, T. Tanaka, T. Akahane, N. Tsuda, *J.Phys.Soc.Jpn.* **41**, 908 (1976).

[35] M. Moskovits, D. P. DiLella, *J.Chem.Phys.* **73**, 6068 (1980).

[36] S. P. Centeno, I. Lpez-Tocn, J. F. Arenas, J. Soto, J. C. Otero, *J.Phys.Chem.B* **110**, 14916 (2006).

[37] G. R. Erdheim, R. L. Birke, J. R. Lombardi, *Chem.Phys.Lett.* **69**, 495 (1980).

[38] T. Markvart, L. Castaner, *Practical Handbook of Photovoltaics: Fundamentals and Applications* (Elsevier Advanced Technology, Oxford, UK, 2003).

[39] S. Pillai, K. R. Catchpole, T. Trupke, M. A. Green, *J. Appl. Phys.* **101**, 093105 (2007).

[40] H. R. Stuart, D. G. Hall, *Appl. Phys. Lett.* **73**, 3815 (1998).

[41] D. M. Schaadt, B. Feng, E. T. Yu, *Appl.Phys.Lett.* **86**, 063106 (2005).

[42] D. Derkacs, S. H. Lim, P. Matheu, W. Mar, E. T. Yu, *Appl. Phys. Lett.* **89** (2006).

[43] D. Derkacs, W. V. Chen, P. M. Matheu, S. H. Lim, P. K. L. Yu, E. T. Yu, *Appl. Phys. Lett.* **93** (2008).

[44] P. Matheu, S. H. Lim, D. Derkacs, C. McPheeters, E. T. Yu, *Appl.Phys.Lett.* **93**, 113108 (2008).

[45] M. Losurdo, M. M. Giangregorio, G. V. Bianco, A. Sacchetti, P. Capezzuto, G. Bruno, *Sol. Energy Mater. Sol. Cells* **93**, 1749 (2009).

[46] A. J. Morfa, K. L. Rowlen, T. H. Reilly III, M. J. Romero, J. van de Lagemaat, *Appl.Phys.Lett.* **92**, 013504 (2008).

[47] K. R. Catchpole, A. Polman, *Opt. Express* **16**, 21793 (2008).

[48] F. Hallermann, C. Rockstuhl, S. Fahr, G. Seifert, S. Wackerow, H. Graener, G. v. Plessen, F. Lederer, *Phys. Status Solidi A* **205**, 2844 (2008).

[49] R. A. Pala, J. White, E. Barnard, J. Liu, M. L. Brongersma, *Adv. Mater.* **21**, 3504 (2009).

[50] F. Kim, J. H. Song, P. Yang, *J. Am. Chem. Soc.* **124**, 14316 (2002).

Part 5

Tuning the Emission Bands of Nanophosphors through the Refractive Index of the Medium

Summary

Photoluminescence spectra of nanophosphors including the yellow phosphor YAG:Ce as well as the green and red phosphors based on CdSe nanoparticles have been studied in the media of oxide gels and polymers of different refractive indices. The oxide gels employed are of silica, zirconia and their solid solutions with the refractive index, n, varying between 1.46 and 2. Different polymers afforded the variation of refractive index in the range 1.35-1.58. The wavelength corresponding to emission maxima of the phosphors

A paper based on this study has appeared in Chemical Physics Letters (2006).

are found to shift to lower wavelengths with increase in the refractive index of the medium. The shifts in the various media are found to be proportional to the refractive index term, $(n^2- 1)/(2n^2 + 1)$. The sensitivity of the emission maxima of the nanophosphors to the medium refractive index may be useful for practical applications such as solid-state lighting.

5.1 Introduction

Solid-state lighting is assuming great importance since it promises not only high brightness and efficiency but also cost effectiveness. The most popular, phosphor based white light sources typically contain a diode that emits in the blue or ultraviolet region and phosphors to down-convert the energy giving rise to white light.

The first phosphor-based white LED used a blue GaInN LED pumping a YAG:Ce ($Y_3Al_5O_{12}$:Ce^{3+}) yellow phosphor. YAG:Ce has been found to be suitable phosphor for converting the blue LED radiation into a very broad band yellow emission [1, 2]. The broad excitation band covering between 400 and 500 nm gives rise to the blue-complementary yellow emission which provides a basis to use the phosphor along with blue GaN LEDs to produce white light. The amount, density, matrix and distribution of phosphor inside LED packages are adjusted to optimize the colour-rendering characteristics and the device efficiency. Therefore, any improvement in the luminescence of YAG:Ce is extremely valuable to raise the quality of the white light. The blue light with a shorter wavelength should be matched by yellow light that also has a shorter wavelength to produce ideal white light in a complementary manner. At present, the emission peak of individual blue LEDs varies from 450 to 480 nm. As a result, it is necessary to have YAG:Ce phosphors with adjustable emission wavelength matching the blue LEDs so as to obtain optimal quality of white light. It is therefore, an aspect of great interest and value to tune the emission band of the phosphor. In this context, even a small shift or broadening of the emission band could be beneficial for optimising

the quality of white light in terms of CIE co-ordinates, color rendering index and color temperature.

There is an intense research today on the right choice of phosphors and the matrices for dispersing the phosphors. Nanophosphors such as nanoparticles of YAG:Ce and CdSe nanoparticles have been extensively investigated during the last decade due to their application potential for various high-performance displays and devices [3]. In YAG system the Y^{3+} site occupied by Ce^{3+} has a distorted cubic symmetry. Ce^{3+} with $4f^1$ configuration has a ground state split into a doublet due to spin-orbit interaction. On photo-excitation, the 4f electron is excited to a 5d level which is further split into various Stark levels due to crystal field excited by the host matrix. The allowed 5d-4f transition gives rise to intense yellow emission. The emission band of YAG:Ce phosphor is known to shift depending on methods of preparation and codoping [4–6]. There are also attempts to tune the luminescence of Ce^{3+} in garnet phosphors by altering the symmetry around the rare-earth ion in different host matrices [7].

Highly photoluminescent quantum dots also have been attracting a great attention as potential nanophosphors with their advantages over other phosphors in terms of emission tunability, efficiency and photostability [3]. There have been reports on the white light emitting composites and LEDs based on luminescent quantum dots [8–12]. In this regard, the incorporation of the quantum dots as chromophores in various host materials such as polymers [13–15] and inorganic oxides [16,17] is gaining importance. The optical properties of semiconductor nanocrystals are also influenced by the surrounding medium, according to the studies by varying the solvent or matrix of

dispersion [16, 18–20]. Bullen *et al.* studied the effect of incorporation of quantum dots into ZrO_2-SiO_2 sol gel matrix and found a shift to shorter wavelengths for emission peak. The studies carried out in oxygen rich environment showed blue shift in emission peak due to photooxidation [21].

In photonic crystals, the periodic variation in the dielectric function or index of refraction is the key to unique colors. The color change of metal nanocrystals from blue to red in glassy film matrices of different refractive indices is also well known [22, 23]. While a large number of workers are trying to discover better phosphors by doping appropriate rare earth ions in different matrices, we considered it worthwhile to explore how the emission bands of phosphors can be tuned by varying the optical properties of the matrix. In many applications utilising phosphors, the refractive index of the matrix plays an important role. To achieve enhanced light absorption using phosphor layers on solar cells, the refractive index of the matrix need to be suitable for directing the scattered as well as emitted light towards the the underlying solar cell [24]. The efficiency of a white LED was shown to improve by introducing a difference in refractive indices among the layers of phosphor geometry using a silicone gel sandwich layer which decreases reabsorption of light among phosphors [25]. Thus, it is interesting to explore the effect of refractive index of the medium on the emission properties of the nanophosphors. For this purpose, we have varied the refractive index of the matrix to tune the emission band of nanophosphors by employing gels of SiO_2, 45% SiO_2-55% ZrO_2 and ZrO_2 with refractive indices, n, of 1.46, 1.71 and 2.0 respectively. We have also employed polymer matrices of different

refractive indices. The polymers employed are tetrafluoroethylene hexafluoropropylene vinylidene fluoride (THV), polymethyl methacrylate (PMMA) and polycarbonate (PC) with refractive indices 1.35, 1.49 and 1.58 respectively. While the quantum dots of semiconductors such as CdS and CdSe have been incorporated in films of oxide gels and polymers, their emission properties have not been studied by varying the refractive index of the matrix. There has also been no study of the yellow phosphor YAG:Ce in these gel and polymer matrices. The present study demonstrates the sensitivity of the luminescence bands to the refractive index of the medium and provides a simple relation between the wavelength corresponding to emission maximum and the refractive index.

5.2 Experimental details

Luminescent YAG:Ce nanoparticles were prepared by sol-gel pyrolysis method as reported by Lu *et al.* [26], using urea and polyvinyl alcohol as fuels. Yittrium nitrate, cerium nitrate, aluminium nitrate, polyvinylalcohol and urea taken in molar ratios 0.57:0.03:1:1.6:1.6 were dissolved in 20 ml of distilled water and heated at 100 ^{o}C for 2 h to give a homogeneous sol. The sol was heated to 250 ^{o}C for 2 h to get an yellow gel, which was then calcined at 1000 ^{o}C for 4 h to obtain YAG:Ce nanoparticles.

Dodecanethiol-capped CdSe nanoparticles were prepared by the procedure described by Gautam *et al.* [27]. In a typical reaction, 0.34 g of cadmium stearate, 25 mg of dodecanethiol, 50 mg of tetralin, and 39.5 mg of selenium powder were taken in 12.5 ml of toluene in a teflon gasketed stainless steel autoclave (70% filling). The autoclave was held at 250 ^{o}C for 5

h and cooled to room temperature.The transparent orange coloured solution obtained was treated with 2-propanol to precipitate the CdSe nanoparticles. The CdSe nanoparticles were redissolved in toluene and precipitated again using 2-propanol. This procedure yielded nanoparticles of $\sim$3 $\pm$1 nm diameter (Figure 5.3a).When the amounts of cadmium stearate, selenium, and tetralin taken were halved with the double the amount of dodecanethiol in the above reaction, we could obtain CdSe nanoparticles of $\sim$5$\pm$1 nm size (Figure 5.3b).

SiO_2, 45% SiO_2-55% ZrO_2 and ZrO_2 sols were prepared by using tetraethyl orthosilicate (TEOS) and zirconium isopropoxide as precursors, according to the procedure reported in the literature [22]. The silica sol (25 equivalent wt% SiO_2) was prepared using TEOS, n-propanol, water, and catalytic amount of hydrochloric acid. The molar ratio of TEOS: n-propanol:water:HCl was 1:3.5:1:0.01. Zirconia sol (20 equivalent wt% of ZrO_2) was prepared from zirconium isopropoxide,n-propanol, and acetyl acetone. The molar ratio of zirconium propoxide:n-propanol:acetyl acetone was 1:3.5:0.6. The silica sol and zirconia sol in molar ratio 45:55 were mixed under stirring to prepare a silica-zirconia sol. Nanocrystalline YAG:Ce was ultrasonically dispersed in the SiO_2, SiO_2-ZrO_2 or ZrO_2 sol and deposited on quartz substrates by spincoating. The doped mole percentage of YAG:Ce nanoparticles in the sol was 0.17% . The composite films were dried at 200 ^oC for 1 h and heated to 500 ^oC for 2 h. Also solutions of CdSe nanoparticles in toluene (with concentrations of 6.6 and 4 μM for particles of 3 and 5 nm diameter, respectively) were mixed with the SiO_2, SiO_2-ZrO_2 or ZrO_2 sol (1 ml/1 ml) and spincoated on quartz substrates.

The composite films were dried at 200 ^{o}C for 1 h. Nanoparticle-polymer composite films of YAG:Ce and CdSe were prepared with THV, PMMA, and PC using suitable solvents such as acetone, toluene, and chloroform. YAG:Ce nanoparticles (20 mg) were ultrasonically dispersed in polymer solutions and spincoated on the quartz substrates. CdSe-polymer composite films were prepared by mixing 1 ml of the nanophosphor solution (with concentrations 6.6 and 4 μM for 3 and 5 nm sized particles, respectively) with the polymer solutions. The composite films were dried at 100 ^{o}C to remove the solvents. It was ascertained that the nanophosphor particles were nicely dispersed in the inorganic or polymer matrix.

X-ray diffraction (XRD) patterns of the nanoparticles were recorded using a Seifert instrument. Transmission electron microscope (TEM) images were obtained with a JEOL JEM 3010, operating at 300 kV. Electronic absorption spectra were recorded with a Perkin-Elmer UV-Visible spectrometer. Photoluminescence spectra were recorded using Perkin-Elmer LS55 luminescence spectrometer.

5.3 Results and discussion

The YAG:Ce particles gave the characteristic X-ray diffraction pattern of cubic garnet structure with a = 12.021 A^o (JCPDS: 33-0040). The particles had an average diameter of 40 nm as revealed from transmission electron microscope (TEM) image (Figure 5.1). YAG:Ce particles show an absorbtion band covering from 400 to 500 nm and a broad yellow emission band centerd at 530 nm (Figure 5.2).

The X-ray diffraction patterns of the CdSe nanoparticles showed the cubic

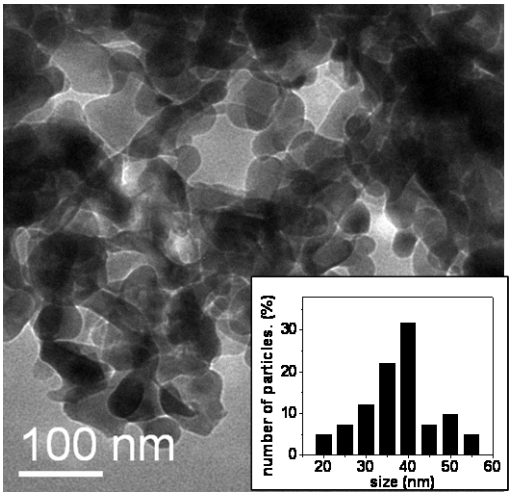

Figure 5.1: TEM image of YAG:Ce nanoparticles. Inset in the Figure shows the particle size distribution.

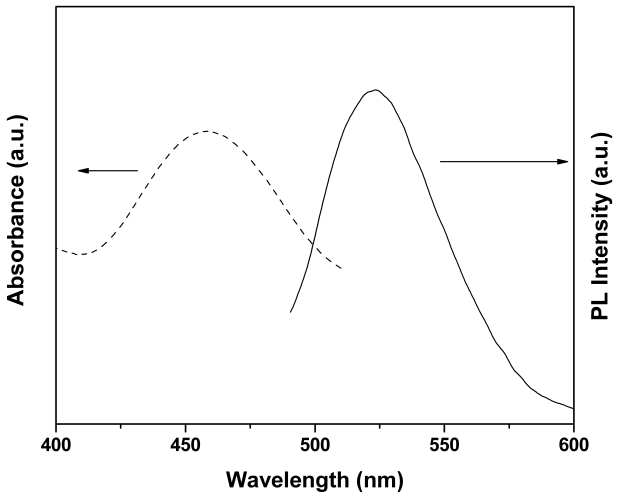

Figure 5.2: Absorption and Photoluminescence spectra of nanoparticles of YAG:Ce.

zinc blende structure (JCPDS: 19-0191). The 3 and 5 nm nanoparticles of CdSe (Figure 5.3) exhibit green and red emissions, respectively (Figure 5.4).

In Figure 5.5a, we show the photoluminescence (PL) spectra of the YAG:Ce nanoparticles in SiO_2 (S) and SiO_2- ZrO_2(SZ) gels with refractive indices of 1.46, and 1.71, respectively. The photoluminescence spectra of YAG:Ce nanoparticles embedded in melted boric acid- glass matrix (B) with refractive index of 1.49 [28] is also included in Figure 5.5a. We observe a blue-shift of the emission maximum with the increase in the refractive index. A similar shift in the PL spectrum is observed when the YAG:Ce nanoparticles are dispersed in the different polymers,THV, PMMA and PC with refractive indices of 1.35, 1.49 and 1.58, respectively (Fig5.5b). We, therefore, suggest that it should be possible to coat a blue emitter with layers of YAG:Ce in gels or polymers of different refractive indices to obtain a satisfactory, broad emission band between 500 and 600 nm, for possible use in improving the quality of white light.

In Figure 5.6 a, we show the PL spectra of the CdSe nanoparicles incorporated in SiO_2(S), SiO_2-ZrO_2 (SZ), and ZrO_2(Z) gel matrices. With increase in the refractive index of the matrix, we observe progressive blue-shifts of the emission bands of the CdSe nanoparticles, with green and red emissions. The PL spectra of these CdSe nanoparticles dispersed in the different polymer matrices are shown in Figure 5.6b. The spectra in Figure 5.6b also exhibit blue-shifts with increase in the refractive index. It appears that a suitable combination of the red and green nanophosphors and the matrices can be used to obtain a better down conversion of blue emission from a LED.

The observed blue shift in the emission peaks with increasing refractive

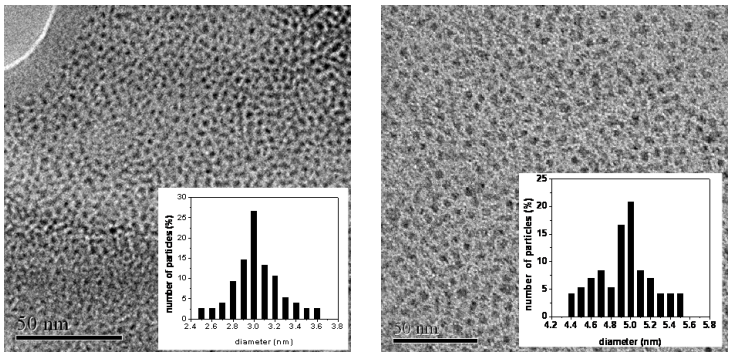

Figure 5.3: TEM images of (a) CdSe 3 nm and (b) CdSe 5 nm nanoparticles. Inset in each Figure shows the particle size distribution.

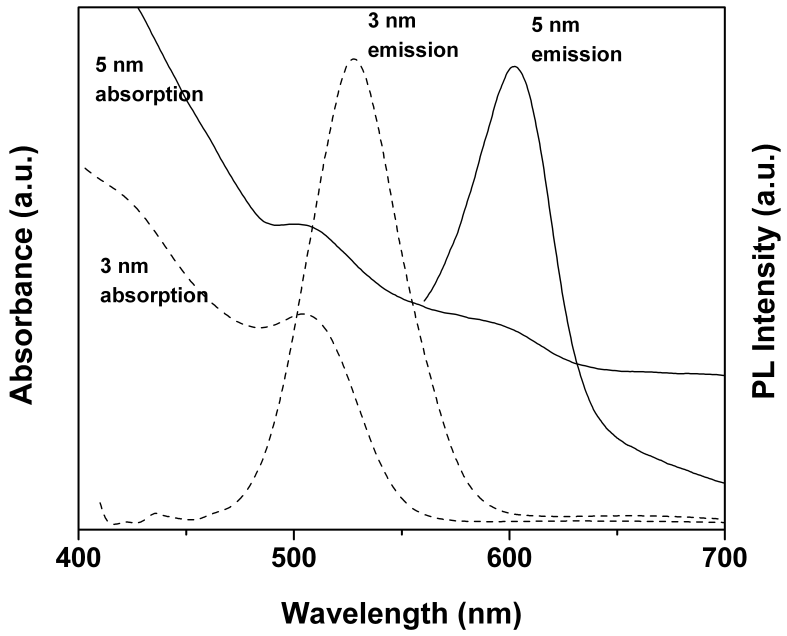

Figure 5.4: Absorption and Photoluminescence spectra of nanoparticles of CdSe.

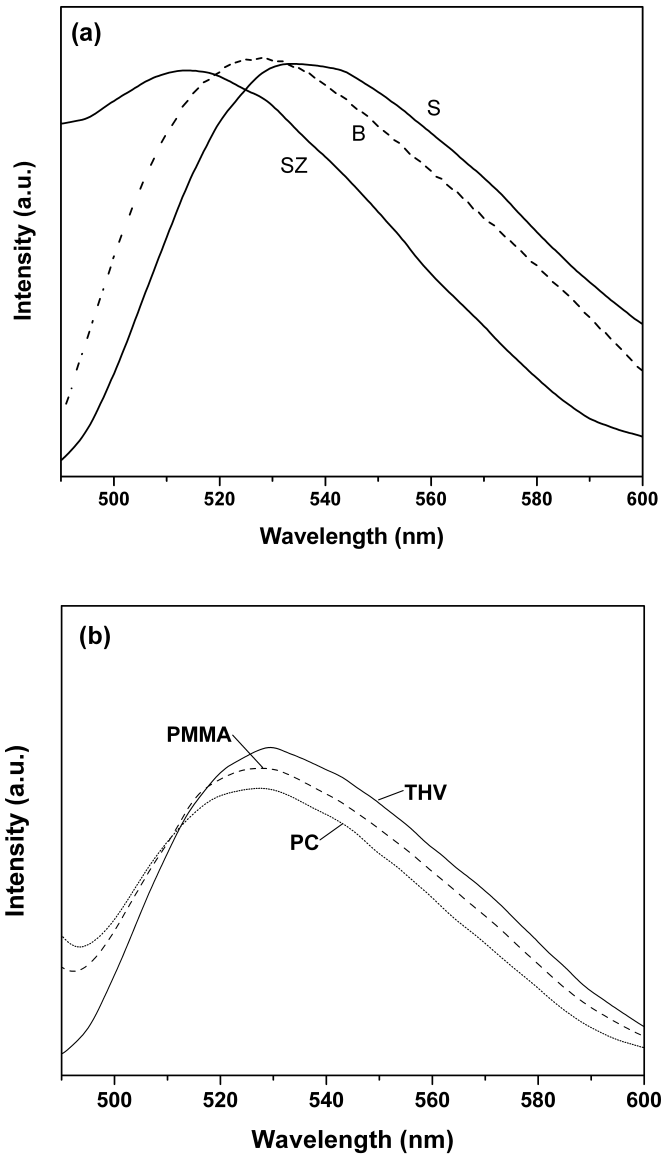

Figure 5.5: Photoluminescence spectra of YAG:Ce nanoparticles embedded in (a) SiO_2(S), B_2O_3 (B) and SiO_2 - ZrO_2 (SZ) gel matrices (b) THV, PMMA, PC polymers. (exc = 460 nm)

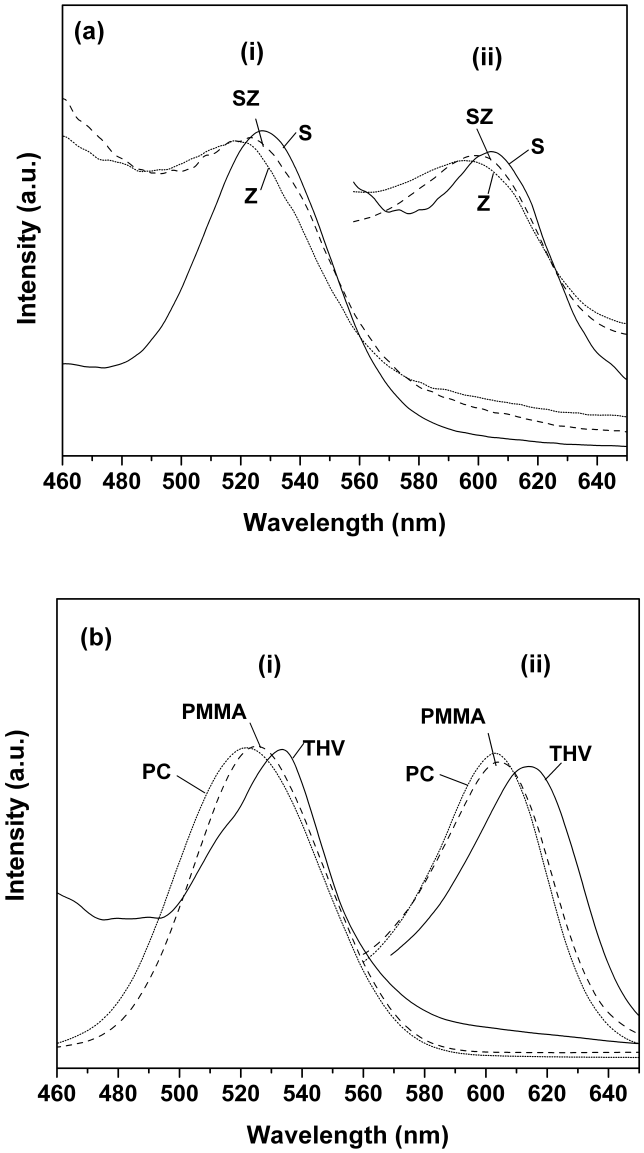

Figure 5.6: (a) Photoluminescence spectra of (i) 3nm and (ii) 5nm CdSe nanoparticles embedded in SiO_2 (S), SiO_2- ZrO_2 (SZ) and ZrO_2 (Z) gel matrices. (b) Photoluminescence spectra of (i) 3nm and (ii) 5nm CdSe nanoparticles embedded in the polymers THV, PMMA and PC. (exc = 400 nm)

index of the matrix agrees well with the relevent literature on semiconductor quantum dots [16, 29, 30]. Increasing the refractive index of the medium causes partial screening of excitons and allows excitonic levels to shift to closer to bandgap, resulting in a shift in PL emission towards higher energy.

In YAG:Ce, it is known that the emission of Ce^{3+} is very sensitive to local crystal field environment [4, 6]. The chemical environment and the symmetry of the host matrix determines the extent of splitting and spiting pattern energy levels in Ce^{3+}. Unlike the 4f level with the shielding of outer shell 6s and 5p electrons, the shift of 5d level and hence the 5d-4f emission band is heavily dependent on the crystal field surroundings. This may also explain the observation that our experiments with other nanophosphors such as $LaPO_4$Eu and $LaPO_4$:Tb, whose emission bands involve f-f transitions of rare earth ions, show no considerable shift in the emission band.

The effect of solvent-solute interactions on the molecular electronic spectra giving raise to solvent dependent emission properties is well documented [31, 32]. Different approaches leading to expressions for band shift due to specific solute-solvent interactions have been developed. Most of the expressions have $(n^2 - 1)/(2n^2 + 1)$ or similar terms to represent solvent parameters, where n is the refractive index. The refractive index term, which is the basis for the well-known Lorentz-Lorentz equation, is also known as Lorentz polarization term. The solvent effects are generally accounted for by showing the linearity of the plot of spectral shift against the refractive index term.

With the data on the different phosphors incorporated in gel and polymer matrices of different refractive indices, we have sought to quantify the variation of the emission band position with the refractive index of medium

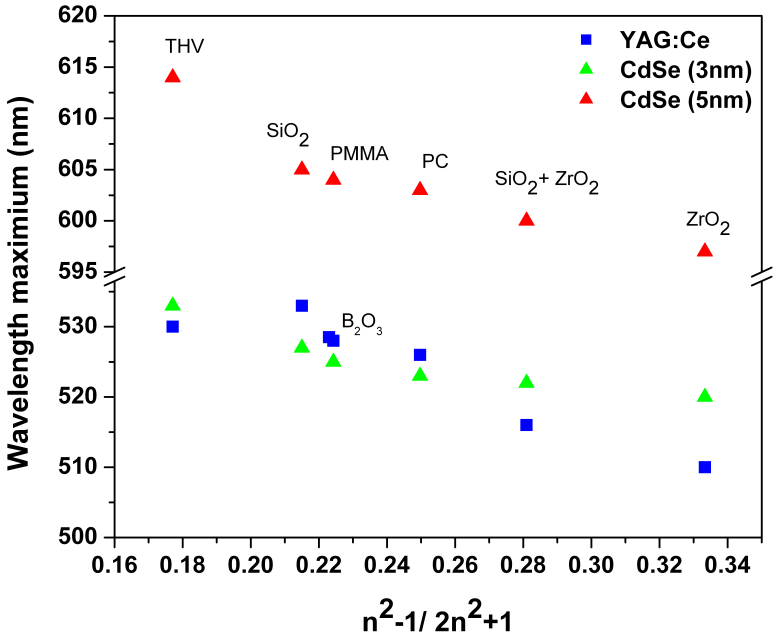

Figure 5.7: Variation of the wavelength of the emission maximum with the refractive index term $(n^2- 1)/(2n^2 + 1)$.

employing the refractive index term. In Figure 5.7, we have plotted the available data of the emission band maxima of the three nanophosphors against the refractive index term $(n^2- 1)/(2n^2 + 1)$. We find that the band position varies proportionally with $(n^2- 1)/(2n^2 + 1)$. Similar variation of wavelength of emission maximum with refractive index term has been observed for ZnO nanoparticles dispersed in solvents of varying refractive index [19]. This relation would be useful in predicting and utilizing emission bands of nanophosphors in practical situations.

5.4 Conclusions

In conclusion, the present study establishes the sensitivity of luminescence bands of nanophosphors to the refractive index of the medium. Although the

electronic and optical properties of nanocrystals of semiconductors such as CdSe have been considered to be sensitive to the medium, especially its dielectric properties [20, 30], the observation of a linear relationship between the wavelength corresponding to emission maximum and the refractive index term, $(n^2 - 1)/(2n^2 + 1)$, is indeed noteworthy. The results of the present study can be extended to other phosphors as well as different gel and polymer matrices for possible use in solid-state lighting and other applications.

References

[1] A. Bergh, G. Craford, A. Duggal, R. Haitz, *Phys.Today* **54**, 42 (2001).

[2] E. F. Schubert, J. K. Kim, H. Luo, J. Xi, *Rep. Prog. Phys.* **69**, 3069 (2006).

[3] H. Chander, *Mater.Sci.Eng.Rep.* **49**, 113 (2005).

[4] Y. Pan, M. Wu, Q. Su, *J.Phys.Chem.Solids* **65**, 845 (2004).

[5] X. Lia, H. Liua, J. Wanga, H. Cuia, F. Han, *Mater.Res.Bull.* **39**, 1923 (2004).

[6] M. Kottaisamy, P. Thiyagarajan, J. Mishra, M. S. R. Rao, *Mater.Res.Bull.* **43**, 1657 (2008).

[7] J. L. Wu, G. Gundiah, A. K. Cheetham, *Chem.Phys.Lett.* **441**, 250 (2007).

[8] J. Park, J. Kim, B. Chin, Y. Kim, J. Kim, O. Park, *Nanotechnology* **15**, 1217 (2004).

[9] H. Sun, J. Zhang, H. Zhang, Y. Xuan, C. Wang, M. Li, Y. Tian, Y. Ning, D. Ma, B. Yang, Z. Y. Wang, *ChemPhysChem* **7**, 2492 (2006).

[10] Y. Xuan, D. Pan, N. Zhao, X. Ji, D. Ma, *Nanotechnology* **17**, 4966 (2006).

[11] M. Tan, V. Mahalingam, F. C. J. M. Veggel, *Appl.Phys.Lett.* **91**, 093132 (2007).

[12] Y. Li, A. Rizzo, R. Cingolani, G. Gigli, *Adv.Mater.* **18**, 2545 (2006).

[13] M. Peres, L. C. Costa, A. Neves, M. J. Soares, T. Monteiro, A. C. Esteves, A. Barros-Timmons, T. Trindade, A. Kholkin, E. Alves, *Nanotechnology* **16**, 1969 (2005).

[14] L. Pang, Y. Shen, K. Tetz, Y. Fainman, *Opt.Express* **13**, 44 (2005).

[15] A. V. Firth, D. J. Cole-Hamilton, J. W. Allen, *Appl.Phys.Lett.* **75**, 3120 (1999).

[16] C. Bullen, P. Mulvaney, C. Sada, M. Ferrari, A. Chiasera, A. Martucci, *J.Mater.Chem.* **14**, 1112 (2004).

[17] Q. Wang, N. Iancu, D. Seo, *Chem.Mater.* **17**, 4762 (2005).

[18] T. Qiu, X. L. Wua, F. Konga, H. B. Mac, P. K. Chub, *Phys.Lett.A* **334**, 447 (2005).

[19] D. Haranath, S. Sahai, P. Joshi, *Appl.Phys.Lett.* **92**, 233113 (2008).

[20] H. Nasu, A. Tanaka, K. Kamada, T. Hashimoto, *J.Non-Cryst.Solids* **351**, 893 (2005).

[21] A. Nazzal, X. Wang, L. Qu, W. Yu, Y. Wang, P. Peng, M. Xiao, *J. Phys. Chem. B* **108**, 5507 (2004).

[22] F. Gonella, G. Mattei, G. Battaglin, A. Quaranta, G. De, M. Montecchi, *Chem.Mater.* **11**, 814 (1999).

[23] S. K. Medda, S. De, G. De, *J.Mater.Chem.* **15**, 3278 (2005).

[24] J. A. Mawyin, S. G. Chawda, G. P. Halada, C. R. Clayton, R. J. Tonucci, C. M. Fortmann, *J. Non-Cryst. Solids* **354**, 2492 (2008).

[25] Y.-H. Won, H. S. Jang, K. W. Cho, Y. S. Song, D. Y. Jeon, H. K. Kwon, *Opt.Lett.* **34**, 1 (2009).

[26] X. H. Lu, H. C. Hong, R. Jagannathan, *J.Mater.Chem.* **12**, 2525 (2002).

[27] U. K. Gautam, M. Rajamathi, F. Meldrum, P. Morgan, R. Seshadri, *Chem.Commun.* pp. 629–630 (2001).

[28] H. Schwarz, J.and Ticha, *J.Optoelectron.Adv.Mater.* **5** (2003).

[29] H. A. Lopez, X. Chen, S. Jenekhe, P. Fauchet, *J.Lumin.* **80**, 115 (1999).

[30] E. Rabani, B. Hetnyi, B. J. Berne, L. E. Brus, *J.Chem.Phys.* **110**, 5355 (1999).

[31] C. N. R. Rao, S. Singh, V. Senthilnathan, *Chem.Soc.Rev.* **5**, 297 (1976).

[32] C. N. R. Rao, *Ultraviolet and Visible Spectroscopy* (Butterworths, London, 1975).

Part 6

Optical Spectroscopic Studies of Composites of Conducting PANI with CdSe and ZnO Nanoparticles

Summary

Composites of CdSe and ZnO nanoparticles with conducting polyaniline have been prepared and investigated by optical spectroscopic method. A decrease in nanoparticle photoluminescence has been observed with the increase in the concentration of the polymer in the composites. The study shows that polyaniline causes the quenching of the nanoparticle luminescence.

A paper based on this study has appeared in Chemical Physics Letters (2006).

6.1 Introduction

Semiconductor nanoparticles are an important class of nanomaterials as they exhibit size-dependent electronic and optical properties with applications in biological tagging, non-linear optics, light emitting diodes and other optoelectronic devices [1]. A simple approach towards integration of nanoparticles in device fabrication is to incorporate them into polymer matrices. The preparation and characterization of polymer-nanoparticle composite materials have therefore been of much interest. A number of polymers and semiconductor nanoparticles have been examined in this context. Thus, charge separation and transport in poly(2-methoxy,5-(20-ethyl)-hexyloxy-p-phenylenevinylene) (MEH-PPV)-CdX (X = S, Se) nanoparticle composites have been studied by photoluminescence quenching and photoconductivity [2, 3]. Kucur *et al.* [4, 5] have examined photoluminescence quenching in CdSe nanoparticle-conducting polymer composites and found strong quenching of photoluminescence of the conjugated polymers such as poly-3-octylthiophene and polyvinylpyrrolidone in the presence of the nanoparticles because of rapid charge transfer. In the case of poly-3-hexylthiophene, quenching of CdSe emission has been observed. Cyr *et al.* [6] have studied polyferrocene materials as host matrices for CdSe nanoparticles and found that the ferrocene centres in the polymers cause quenching of CdSe nanoparticle luminescence. The photoinduced charge transfer evidenced by the photoluminescence quenching in such polymer nanocomposites is made use of in devices such as solar cells.

Polyaniline (PANI) is an air stable polymer and has attracted considerable attention because of its high electrical conductivity. Several device applications of PANI include electrodes for rechargeable batteries, sensors, electrochromic displays and photovoltaic devices. PANI is unique as its electronic properties can be controlled both by varying the oxidation state of the main chain and by protonation [7]. The nonconducting emaraldin base form of polyaniline can be converted to highly conducting emaraldin salt form by protonation (doping with H^+ ions) using an acid such as HCl or camphor sulphonic acid (CSA). Recent investigations have shown that PANI can be an excellent matrix for forming polymer-nanomaterial composites [8–11]. Enhancement in CdS photoluminescence has been observed by Xi *et al.* [12] on incorporation of CdS nanowires in non-conducting PANI matrix. A mechanism wherein photo-generated charge carriers transfer from PANI to CdS has been suggested. Similar effects have been observed in PANI-ZnO nanocomposites [13]. In this part, a study of the optical properties of composites of PANI with CdSe and ZnO nanoparticles has been presented. The PANI-nanoparticle composites were prepared using highly conducting camphor sulfonic acid doped PANI. We observe the quenching of the nanoparticle luminescence on their incorporation in the polymer matrix.

6.2 Experimental details

A camphor sulfonic acid doped polyaniline (PANI-CSA) solution was prepared in m-cresol by mixing 1.092 g (0.012 M) of emaraldine base with 1.394 g (0.006 M) of camphor sulfonic acid using an agate mortar and pestle [14].

PANI-CSA (2 wt%) solution was prepared by adding the appropriate quantity of PANI-CSA to m-cresol. The mixture was then treated in an ultrasonic bath for 48 h and subsequently centrifuged. Most of the PANI- CSA complex dissolved to give a deep green solution. Minor insoluble solids were removed by decanting. TOPO-capped CdSe nanoparticles were prepared by the solvothermal reaction of cadmium stearate, tetralin, TOPO and selenium powder in toluene at 250 ^{o}C for 5 h [15]. The transparent orange coloured solution obtained was treated with 2-propanol to precipitate the CdSe nanoparticles. The CdSe nanoparticles were redissolved in toluene and precipitated again using 2-propanol. A solution of nanoparticles in m-cresol was prepared and was used in the preparation of the composites. ZnO nanoparticles were prepared by precipitation from $Zn(CH_3COO)_2$ and NaOH as reported in the literature [16].

The composite solutions were prepared by mixing ultrasonically the appropriate amounts of PANI-CSA solution and the nanoparticles dispersed in m-cresol. The molar compositions of the PANI- CdSe composites were 2:1, 2:3, 2:10 (molar ratios). The compositions of the PANI- ZnO composites were 3:1, 1:1, 1:2, 1:4, 1:8. Transmission electron microscope (TEM) images of the composites were obtained with a JEOL JEM 3010, operating at 300 kV. Electronic absorption spectra were recorded with a Perkin Elmer UV-visible-NIR spectrometer. Photoluminescence spectra were recorded using Perkin Elmer LS55 luminescence spectrometer.

6.3 Results and discussion

In Figure 6.1 (a) and (b), we show the TEM images of CdSe and ZnO nanoparticles used in the preparation of the nanocomposites. The CdSe and ZnO nanoparticles had average diameters of 4 nm and 40 nm respectively. The X-ray diffraction pattern of the CdSe and ZnO nanoparticles showed the cubic zinc blende structure (JCPDS: 19-0191) and the hexagonal structure (JCPDS: 36-1451) respectively. In Figure 6.1 ((c) and (d), we show typical TEM images of PANI-CdSe and PANI-ZnO composites respectively.

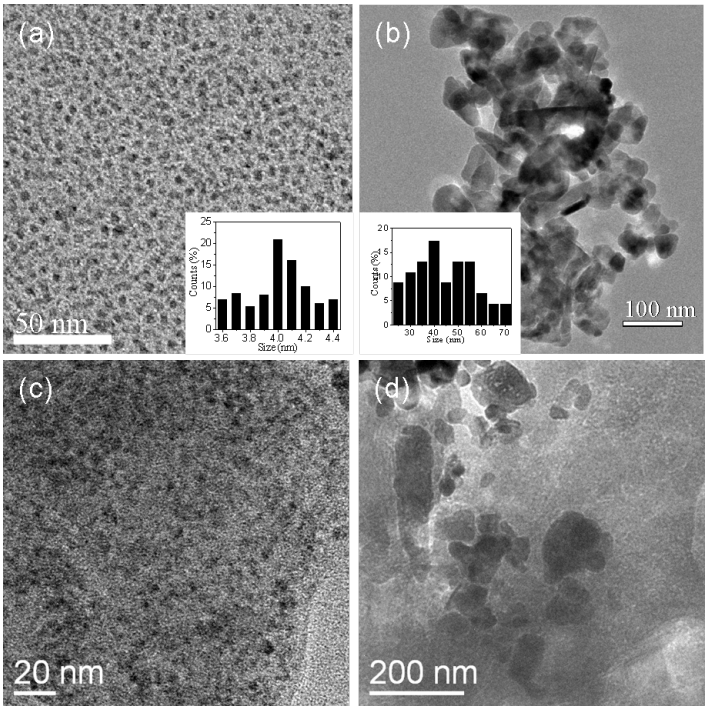

Figure 6.1: TEM images of (a) CdSe nanoparticles, (b) ZnO nanoparticles, (c) PANI-CdSe nanoparticle composite and (d) PANI-ZnO nanoparticle composite. Insets in (a) and (b) show particle size distribution of CdSe and ZnO nanoparticles respectively.

The nanoparticles are seen to be dispersed in the polymer matrix. In Figures 6.2 and 6.3, we show the absorption and photoluminescence (PL) spectra of PANI, CdSe nanoparticles and the PANI-CdSe nanoparticle composites. PANI shows a sharp absorption band centered at 440 nm due to the polarons. The broad band in the near IR region is due to the free charge carriers, characteristic of high electrical conductivity [17]. The CdSe nanoparticles exhibit an excitonic absorption band at 512 nm as shown in Figure 6.2. For the purpose of comparison, we have normalized the absorption spectra of the nanocomposites with respect to the molar fraction of PANI in the composites. We observe a decrease in the intensity of absorption bands corresponding to that of PANI as the concentration of CdSe nanoparticles was increased in the composites. The CdSe excitonic band shows an increase in intensity with decreasing PANI content. We observe a strong band edge luminescence centered at 550 nm arising from CdSe nanoparticles (Figure 6.3) and a marked decrease in the intensity of CdSe luminescence with the increase of the concentration of PANI in the composite.

In Figures 6.4 and 6.5, we show the absorption and photoluminescence spectra of PANI, ZnO nanoparticles and the PANI-ZnO nanoparticle composites. The ZnO nanoparticles show an absorption band at 375 nm. Similar to the PANI-CdSe composites, we observe a decrease in the intensity of the PANI absorption bands and an increase in the intensity of the ZnO absorption band as the concentration of ZnO increases in the composite. The broad emission band at 488 nm due to ZnO nanoparticles shows a large decrease in intensity as the proportion of PANI in the composite increases. Similar observations have been reported for ZnO-graphene oxide nanocomposites, where

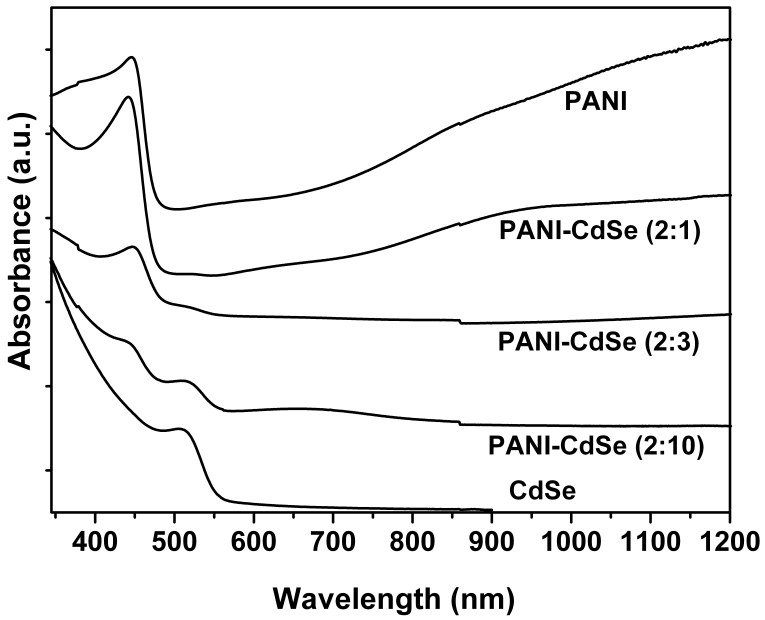

Figure 6.2: Absorption spectra of various PANI-CdSe nanoparticle composites.

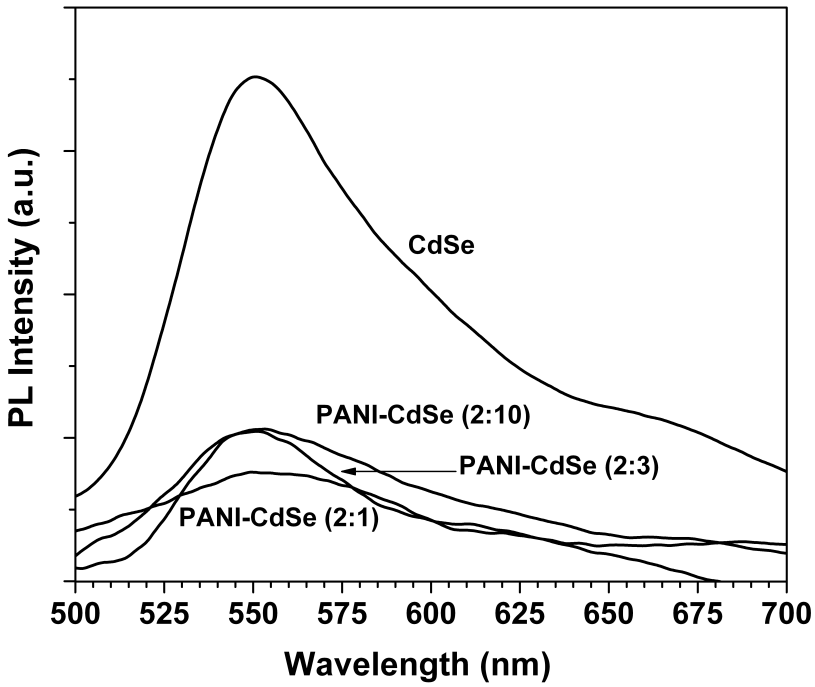

Figure 6.3: Photoluminescence spectra of various PANI-CdSe nanoparticle composites.

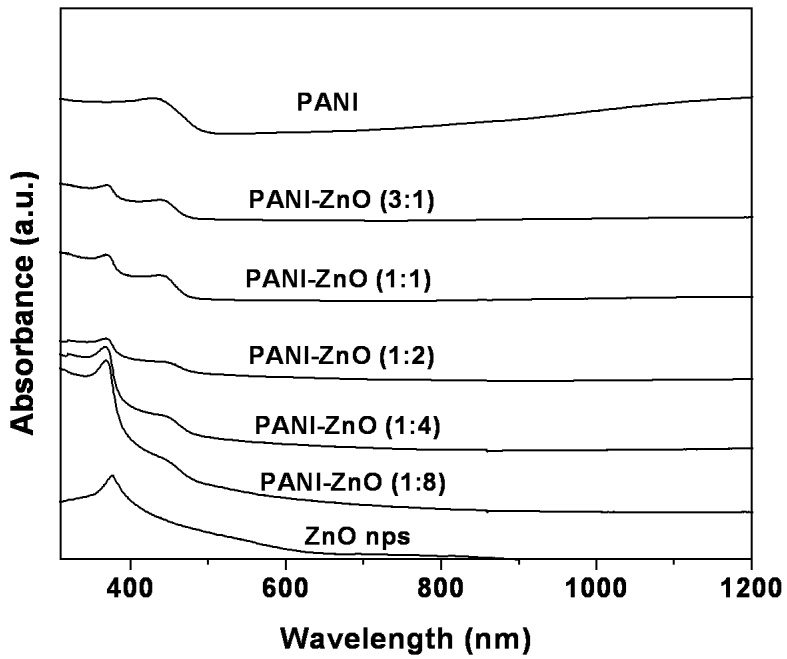

Figure 6.4: Absorption spectra of various PANI-ZnO nanoparticle composites.

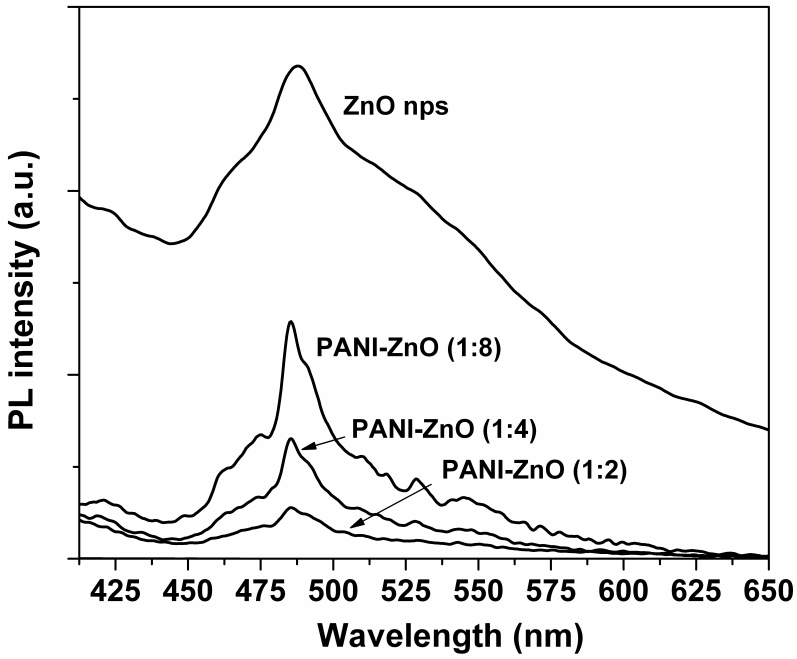

Figure 6.5: Photoluminescence spectra of various PANI-ZnO nanoparticle composites.

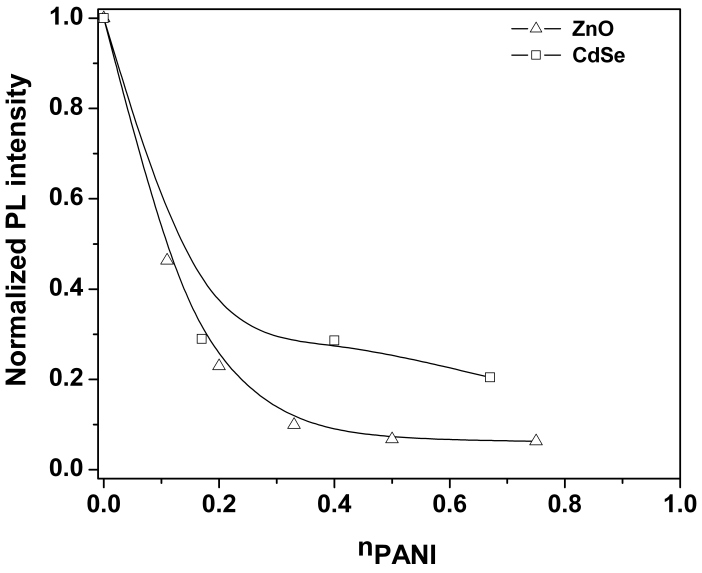

Figure 6.6: Variation of the photoluminescence intensity of CdSe and ZnO nanoparticles in PANI composites.

the luminescence quenching of the green emission of ZnO served as a probe to monitor the electron transfer from excited ZnO to graphene oxide [18].

In Figure 6.6, we have shown the variation of the PL intensity of the CdSe and ZnO nanoparticles with respect to the molar fraction of PANI in the composite. We observe a large decrease in the intensity indicating the quenching of nanoparticle luminescence by PANI. The transfer of photo-generated charge carriers (electrons) from the nanoparticles to hole-conducting PANI causes the decrease in their luminescence. This is also reflected in the decrease of the near IR absorption in PANI, suggesting that the holes from PANI are involved in the quenching of the nanoparticle luminescence. The ZnO emission quenches more rapidly because of the absence of capping agent as compared to the TOPO capped CdSe nanoparticles.

6.4 Conclusions

In conclusion, the present study establishes the effect of PANI on the optical properties of CdSe and ZnO nanoparticles. The photoluminescence spectra of the composites show that the intensity of emission of both CdSe as well as ZnO nanoparticles decreases as the concentration of PANI increases in the composite, thus suggesting the occurrence of quenching of the nanoparticle luminescence by the conducting polymer.

References

[1] C. N. R. Rao, A. Mueller, A. K. Cheetham, *The Chemistry of Nanomaterials: Synthesis, Properties and Applications* (Wiley-VCH, Weinheim, 2004).

[2] N. C. Greenham, X. Peng, A. P. Alivisatos, *Phys.Rev.B* **54**, 17628 (1996).

[3] W. U. Huynh, J. J. Dittmer, A. P. Alivisatos, *Science* **295**, 2425 (2002).

[4] E. Kucur, J. Riegler, G. A. Urban, T. Nann, *J.Chem.Phys.* **120**, 1500 (2004).

[5] E. Kucur, J. Riegler, G. A. Urban, T. Nann, *J.Chem.Phys.* **121**, 1074 (2004).

[6] P. W. Cyr, M. Tzolov, M. A. Hines, I. Manners, E. H. Sargent, G. D. Scholes, *J.Mater.Chem.* **13**, 2213 (2003).

[7] J. L. Bredas, R. Silbey, *Conjugated Polymers* (Kluwer Academic Publishers,London, 1991).

[8] D. Y. Godovsky, A. E. Varfolomeev, D. F. Zaretsky, R. L. N. Chandrakanthi, A. Kndig, C. Weder, W. Caseri, *J.Mater.Chem.* **11**, 2465 (2001).

[9] R. L. N. Chandrakanthi, M. A. Careem, *Thin Solid Films* **417**, 51 (2002).

[10] P. K. Khanna, M. V. Kulkarni, N. Singh, S. P. Lonkar, V. V. V. S. Subbarao, A. K. Viswanath, *Mater.Chem.Phys.* **95**, 24 (2006).

[11] S. R. C. Vivekchand, K. C. Kam, G. Gundiah, A. Govindaraj, A. K. Cheetham, C. N. R. Rao, *J.Mater.Chem.* **15**, 4922 (2005).

[12] Y. Xi, J. Zhou, H. Guo, C. Cai, Z. Lin, *Chem.Phys.Lett.* **412**, 60 (2005).

[13] Z. X. Zheng, Y. Y. Xi, P. Dong, H. G. Huang, J. Z. Zhou, L. L. Wu, Z. H. Lin, *PhysChemComm* **5**, 63 (2002).

[14] M. Reghu, Y. Cao, D. Moses, A. J. Heeger, *Phys.Rev.B* **47**, 1758 (1993).

[15] U. K. Gautam, M. Rajamathi, F. Meldrum, P. Morgan, R. Seshadri, *Chem.Commun.* pp. 629–630 (2001).

[16] J. Bang, H. Yang, P. H. Holloway, *Nanotechnology* **17**, 973 (2006).

[17] Y. Xia, J. M. Wiesinger, A. G. MacDiarmid, A. J. Epstein, *Chem.Mater.* **7**, 443 (1995).

[18] G. Williams, P. Kamat, *Langmuir* **25**, 13869 (2009).

Part 7

A Raman study of the Phase Transition in $KHSO_4$

Summary

Temperature dependent Raman spectroscopic studies have been carried out on $KHSO_4$ single crystal in the temperature range 298 - 493K. A structural phase transition driven by the lattice and molecular disorder is observed at 473K. The spectral data enables an understanding of the nature of the lattice disorder across the phase transition leading to the superionic phase transition. The disorder in HSO_4^- polymeric hydrogen bonded chain leads to a higher symmetry in the high temperature phase is clearly captured from our Raman results.

A paper based on this study has appeared in J. Phys. Chem. A (2010).

7.1 Introduction

Ion conducting solids are of extreme importance because of their potential applications in fuel cells, steam electrolysis and sensors [1–5]. Ion conduction occurs in numerous types of materials [6–11], including hydrogen-bonded systems [12–20]. Among the ion conducting solids, superionic solids exhibit anomalously high conductivity in high temperature phase [12–20]. $KHSO_4$ belongs to the family of alkali sulfates $AHSO_4$ (A= Cs, Rb, NH_4), which are known for their ferroelectric property [21, 22]. $KHSO_4$ does not, however, exhibit ferroelectricity [23], but undergo super ionic phase transition at high temperature [24, 25]. The high conductivity in the super ionic phase in $AHSO_4$ could be due to disorder in crystallographic sites, rotational motion of HSO_4^- or the dynamical motion of the crystal lattice. The room temperature crystal structure of $KHSO_4$ is orthorhombic (space group *Pbca*) with 16 formula units per unit cell. The structure contains two crystallographically independent $KHSO_4$ units. The HSO_4^- ion is usually found in a distorted tetrahedral symmetry. Furthermore, it is connected with short O-H...O hydrogen bonds forming one dimensional long polymeric chains and zero-dimensional dimers.

The structural phase transitions in $KHSO_4$ were studied by several authors using thermal analysis [24], NMR spectroscopy and conductivity measurement [25]. Based on their conductivity measurements, Sharon *et al.* [26] predicted that the superionic phase transition in $KHSO_4$ is driven by the conversion of dimer units into chains and increase in the rotational degree of freedom of the chain units. A more detailed and accurate analysis of the

phase transition was given by Swain *et al.* [27] using *in situ* single crystal X-ray diffraction. They reported that the structure still remains orthorhombic after the phase transition, but the space group symmetry increases from *Pbca* to *Cmca* keeping 16 formula units per unit cell intact. In the *Cmca* structure, one of the HSO_4^- which is involved in polymeric hydrogen bond chain is disordered at O and H crystallographic sites.

Raman spectroscopy is an ideal tool for capturing the dynamics and local structural changes in crystal systems [28]. It is, therefore, of interest to study the internal as well as external vibrations of molecular units as a function of temperature to understand the mechanism of fast ion conduction and the dynamics of structural phase transition resulting in the superionic phase. The room temperature vibrational modes of $KHSO_4$ have already been reported [29]. In the present study, we have investigated the dynamics of HSO_4^- units using variable temperature Raman spectroscopy in order to understand the changes in structure, conductivity and the nature of the disorder associated with $KHSO_4$ during the phase transition.

7.2 Experimental

Single crystals of $KHSO_4$ were grown by slow evaporation from aqueous solution containing equimolar quantities of the K_2SO_4 and H_2SO_4. The quality of the crystal used for the experiment was checked under an optical polarizing microscope. The temperature evolution of the Raman spectra of $KHSO_4$ was recorded in the 180^0 backscattering geometry, using a 532 nm excitation from a diode pumped frequency doubled Nd-YAG solid state laser

(model GDLM-5015 L, Photop Suwtech Inc., China) and a custom-built Raman spectrometer equipped with a SPEX TRIAX 550 monochromator and a liquid nitrogen cooled CCD (Spectrum One with CCD 3000 controller, ISA Jobin Yovn). Laser power at the sample was ∼8 mW, and a typical spectral acquisition time was 1 min. The spectral resolution chosen was 2 cm^{-1}. The temperature was controlled with an accuracy of (±0.1 K) by using a temperature-controller (Linkam TMS 94) equipped with a heating stage unit (Linkam THMS 600). The spectral profile was fitted using Lorentzian functions with the appropriate background.

7.3 Results and discussion

Figure 7.1 shows the unpolarized Raman spectra of $KHSO_4$ recorded at room temperature in the range of 50-1350 cm^{-1} arising from the external and internal vibrational modes. The internal modes in the region 300-1350 cm^{-1} are divided into three groups: (i) S-OH bending (β_{S-OH}) and O-S-O deformation (δ_{OSO}) (410-870 cm^{-1}), (ii) S-OH stretching (ν_{S-OH}) (855, 872 cm^{-1}) and (iii) symmetric and asymmetric S-O stretching (ν_{S-O}) (1002, 1027, 1165, 1241 cm^{-1}) by considering SO_4^{2-} as a distorted tetrahedra in $C_{3\nu}$ symmetry [29]. The structure contains two crystallographically independent HSO_4^-, corresponding to the chain and dimer units. Raman modes corresponding to these units have been distinguished by Dey *et al.* [29] by considering the interaction among the HSO_4^- units. The interactions are strong in case of dimer than in chain. Hence the frequencies of vibrational modes observed in Raman and IR spectra occur at higher frequencies in the case of the dimer. In contrast, the vibrational modes associated with S-OH

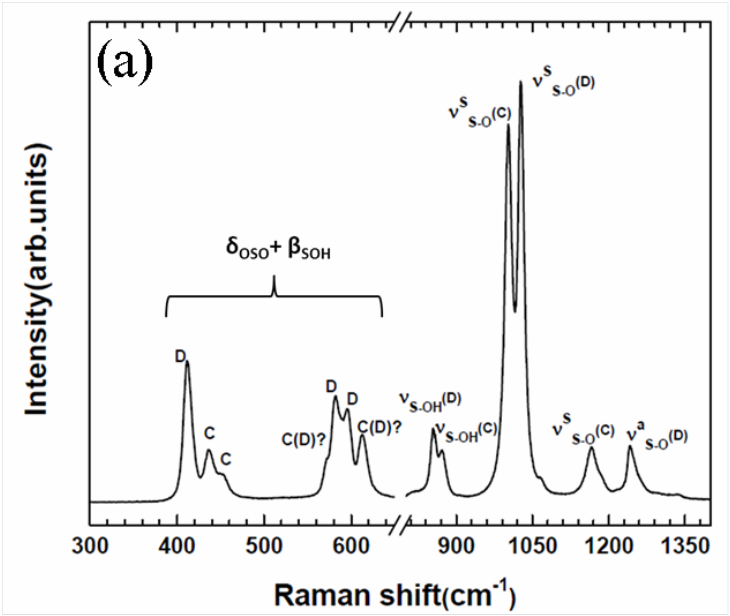

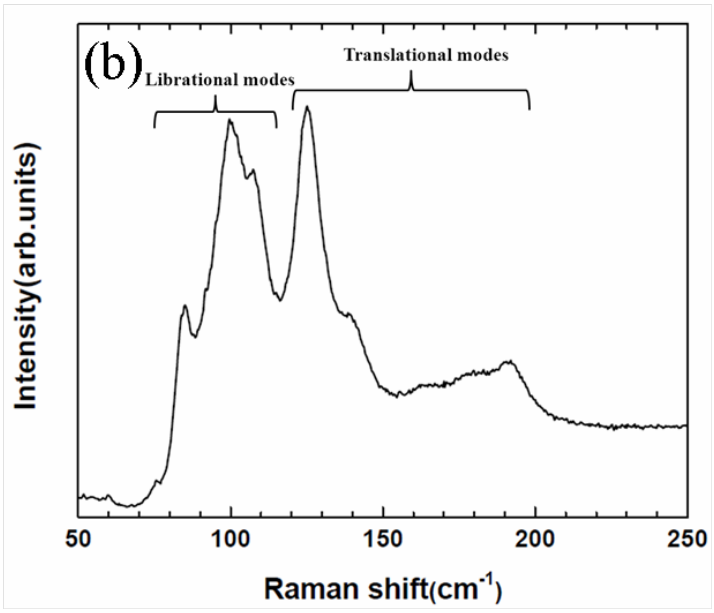

Figure 7.1: Room temperature Raman spectrum of $KHSO_4$ in the frequency range (a) 300-1350 cm^{-1} , (b) 50-250 cm^{-1} (D= Dimer, C= Chain).

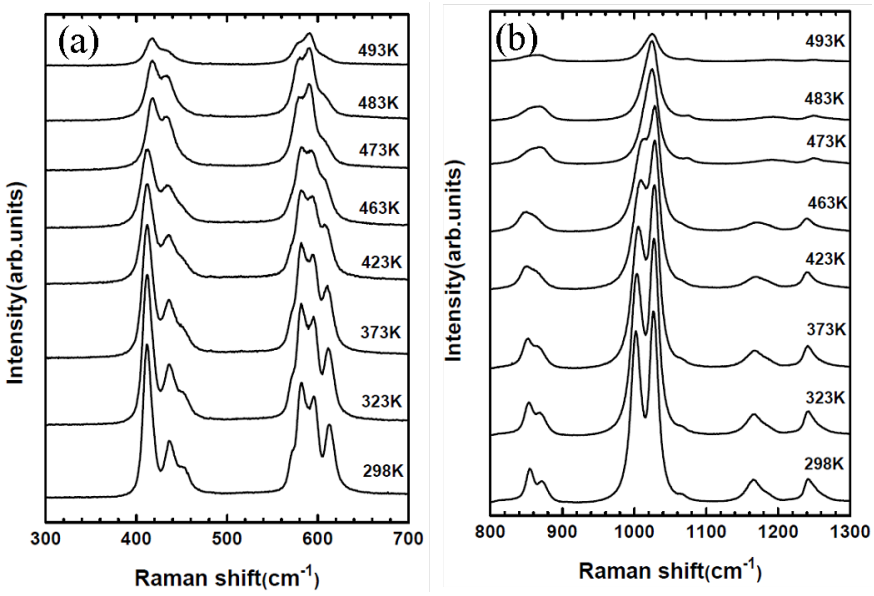

Figure 7.2: Temperature dependent Raman spectra of $KHSO_4$ in the spectral range (a) 300-700 cm^{-1} , (b) 800-1300 cm^{-1}.

stretching and deformation in the dimer should appear at lower frequencies than in the chain (See Figure 7.1a). This is due to the strong hydrogen bonding in the dimer causing the hydrogen atom getting to be pulled away from the oxygen in S-OH. The lattice modes at 84, 90, 99, 108 cm^{-1} are assigned to the librational and those at 125, 139, 165, 179, 192 cm^{-1} to the translational modes (See Figure 7.1b).

The temperature evolution of the Raman spectra of $KHSO_4$ in the temperature range 298-493K is shown in Figure 7.2. We observe major changes in the spectral features around the phase transition temperature (T_C = 473K) and in agreement with the structural phase transition reported by Swain *et al.* [27]. The important changes in the Raman spectra are: disappearance of splitting in symmetric S-O stretching modes (ν_{S-O}); sudden increase in the

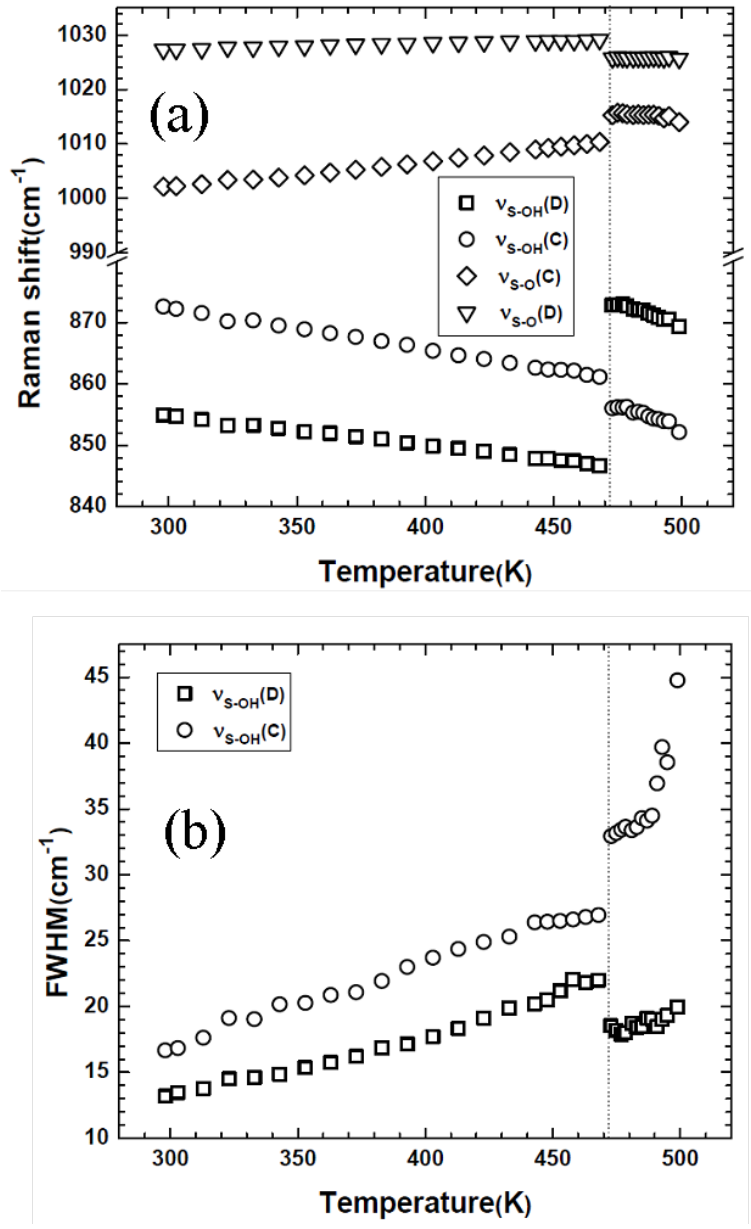

Figure 7.3: (a) Temperature evolution of ν_{S-O}, ν_{S-OH} mode frequencies, (b) FWHM of ν_{S-OH} modes in the temperature range 298-493K (D= Dimer, C= Chain).

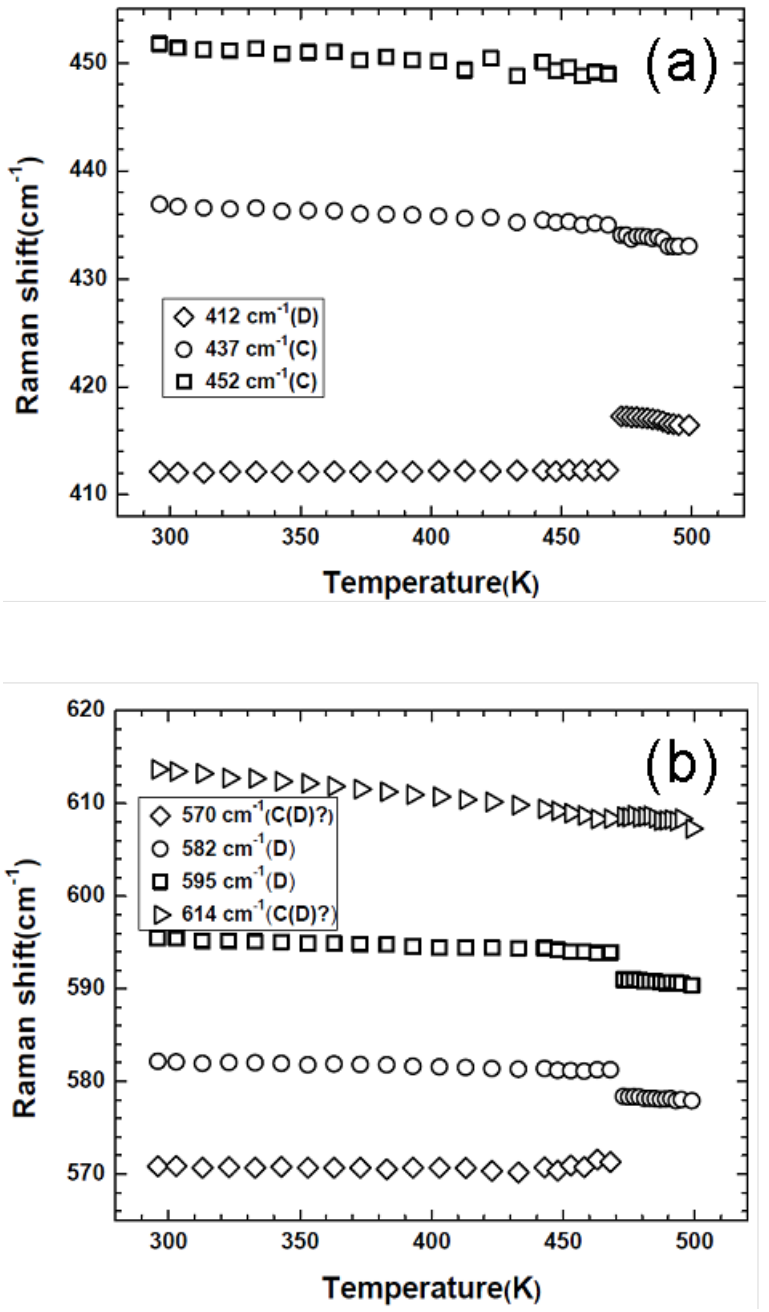

Figure 7.4: Temperature evolution of β_{S-OH}, δ_{OSO} deformation frequencies in the temperature range 298-493K (D= Dimer, C= Chain).

frequency of the S-OH stretching mode (ν_{S-OH}); disappearance of the Raman modes at 452 cm^{-1} and 571 cm^{-1} belong to S-OH bending (β_{S-OH}) and O-S-O deformation (δ_{OSO}) at T_C. These changes are shown in Figure 7.3 and 7.4, where we have plotted the temperature evolution of phonon frequencies and the full width at half maxima (FWHM) of some of the modes. With increase in temperature, ν_{S-OH} decreases, whereas ν_{S-O} increases for both the dimer and the chain. At T_C, there is an abrupt change in the frequency of both ν_{S-O} and ν_{S-OH} modes. The bending mode frequencies plotted in Figure 7.4 also show abrupt changes with some of the modes disappearing above the T_C. We observe an anomalous increase in the FWHM of ν_{S-O} mode across the T_C as can be seen from Figure 7.3b. The line width of ν_{S-O} mode of the chain increases abruptly from 26 to 34 cm^{-1} at 473K and increases steeply to 46 cm^{-1} at 493K. A similar behavior can be seen in the case of ν_{S-O} mode of the chain at 1161 cm^{-1} . It abruptly increases to a higher frequency at T_C as depicted in Figure 7.5. The anomalous broadening of ν_{S-O} mode can also be seen clearly in the inset of Figure 7.5. The reason behind this anomalous behavior will be discussed later. As in the case of the internal modes, the external lattice modes of $KHSO_4$ showed in Figure 7.6 also exhibit significant changes around T_C. Most of the external modes decrease in intensity with temperature and collapse into a broad wing after the phase transition.

We shall now examine the implications of the changes observed in the vibrational modes of $KHSO_4$ across the transition. The anomalous changes in ν_{S-O} and ν_{S-OH} vibrational mode frequencies across phase transition are mainly due to the variations in the bond lengths leading to structural phase

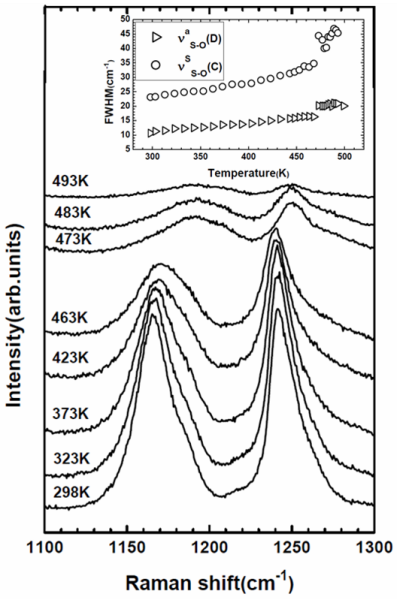

Figure 7.5: Temperature evolution of ν^s_{S-O} (C) and ν^a_{S-O} (D) modes; the inset shows corresponding line-widths (D= Dimer, C= Chain).

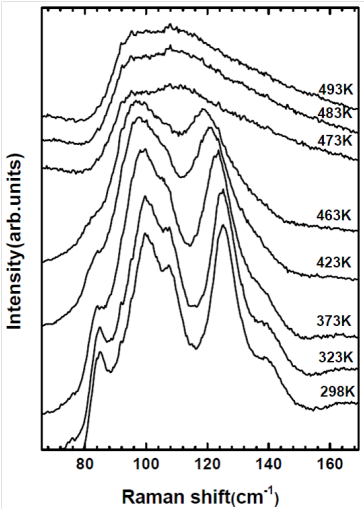

Figure 7.6: Temperature dependence of external lattice modes.

transition at T_C. The disappearance of some of the modes such as the bending modes at T_C implies a higher symmetry structure expected at high temperatures.

The sudden increase in the line width of chain ν_{S-O} and ν_{S-OH} modes shown in Figure 7.3 and in the inset of Figure 7.5 is interesting. Due to the lattice disorder associated with O and H positions in the high-temperature phase, there is a large variation in bond strengths associated in these molecular sub-units. This results in the broadening of these modes. Since the lattice modes are much weaker than the internal modes, this is more evident in their behavior as a function of temperature. The increase in the width leads to the loss of the fine features in the external mode at high temperature. The onset of the disorder in the system due to the variation in the position of oxygen and hydrogen atoms in the system, initiating the transition, is clearly evidenced in the behavior of both the internal and external modes.

Sharon *et al.* [26] proposed that the high conductivity of high temperature phase of $KHSO_4$ is due to the conversion of dimer units into chain and the subsequent rotation of the HSO_4^- tetrahedra. However, our experimental results suggest that there is no such dimer to chain conversion as all the dimer vibrational modes are still present after the phase transition (See Figure 7.3a for example). In fact the excessive broadening suggests that HSO_4^- units are disordered in the polymeric hydrogen bonded chains leading to a higher symmetry in the high temperature phase. Our Raman results demonstrate that the transition is a result of lattice disorder, which sets in much before the transition. It has been suggested in case of chain hydrogen bonded systems, that ion conduction is mainly due to the proton transfer from one end of

the chain to other [30]. From our Raman results, we strongly believe that in our system, the lattice disorder associated with chain HSO_4^- units weakens the hydrogen bonding between two chain units and facilitates the proton to hop from one unit to another resulting in the high conductivity reported in $KHSO_4$ [25].

7.4 Conclusions

The present temperature-dependent Raman spectroscopic investigation is able to explain the dynamics of structural phase transition in $KHSO_4$ crystal. The disappearance and discontinuities of phonon frequencies at T_C are attributed to the structural changes in the crystal during the phase transition. Based on our experimental results, the conversion of dimer units into chain during phase transition can be ruled out. The superionic phase transition in $KHSO_4$ is mainly driven by disorder in chain HSO_4^- ions due to the disorder in the oxygen and hydrogen atom positions. It is clear that the internal S-OH and S-O stretching modes and to a limited extent, the external modes, throw light on the disorder mechanism and the enhancement of conductivity after transition.

References

[1] S. M. Haile, D. A. Boysen, C. R. I. Chisholm, R. B. Merle, *Nature* **410**, 910 (2001).

[2] K. Kreuer, *Chem. Mater.* **8**, 610 (1996).

[3] B. Zhu, I. Albinsson, B.-E. Mellander, G. Meng, *Solid State Ionics* **125**, 439 (1999).

[4] B. Zhu, *Solid State Ionics* **125**, 397 (1999).

[5] R. Bouchet, S. Miller, M. Duclot, J. L. Souquet, *Solid State Ionics* **145**, 69 (2001).

[6] D. Swain, T. N. Guru Row, *Chem. Mater.* **19**, 347 (2007).

[7] R. Murugan, V. Thangadurai, W. Weppner, *Angew. Chem. Int. Ed.* **46**, 7778 (2007).

[8] C. J. Leo, G. V. Subba Rao, B. V. R. Chowdari, *J. Mater. Chem.* **12**, 1848 (2002).

[9] T. Yamada, M. Sadakiyo, H. Kitagawa, *J. Am. Chem. Soc.* **131**, 3144 (2009).

[10] H. A. Every, A. G. Bishop, D. R. MacFarlane, G. Oradd, M. Forsyth, *J. Mater. Chem.* **11**, 3031 (2001).

[11] Y. Matsuo, K. Takahashi, S. Ikehata, *Solid State Commun.* **120**, 85 (2001).

[12] V. Verma, N. Rangavittal, C. N. R. Rao, *J. Sol. Stat. Chem.* **106**, 164 (1993).

[13] A. I. Baranov, L. A. Shuvalov, N. M. Shchagina, *JETP Lett.* **36**, 459 (1982).

[14] R. H. Chen, R.-J. Wang, T. Fukami, C. S. Shren, *Solid State Ionics* **110**, 277 (1998).

[15] A. Kawada, A. R. McGhie, M. M. Labes, *J. Chem. Phys.* **52**, 3121 (1970).

[16] A. I. Baranov, R. M. Fedosyuk, N. M. Schagina, L. A. Shuvalov, *Ferroelect. Lett.* **2**, 25 (1984).

[17] R. Blinc, J. Dolinsek, G. Lahajnar, I. Zupancic, L. A. Shuvalov, A. I. Baranov, *Phys. Status. Solidi* **B123**, k83 (1984).

[18] A. I. Baranov, B. W. Merinov, A. V. Tregubchenko, V. P. Khiznichenko, L. A. Shuvalov, N. M. Schagina, *Solid State Ionics* **36**, 279 (1989).

[19] K. Gesi, *J. Phys. Soc. Jpn.* **48**, 886 (1980).

[20] R. H. Chen, T. M. Chen, C. S. Shern, *J. Phys. Chem. Sol.* **61**, 1399 (2000).

[21] R. Pepinsky, K. Vedam, S. Hoshino, Y. Okaya, *Phys. Rev.* **111**, 1508 (1958).

[22] R. Pepinsky, K. Vedam, *Phys. Rev.* **117**, 1502 (1960).

[23] C. S. Sunandana, *Phys. Stat. sol.* **119**, k59 (1983).

[24] M. E. Kassem, *J. therm. Anal.* **37**, 513 (1991).

[25] Y. Yoshida, Y. Matsuo, S. Ikehata, *Ferroelectrics* **302**, 85 (2004).

[26] M. Sharon, K. A.K., *J .Sol. Stat. Chem.* **31**, 295 (1980).

[27] D. Swain, T. N. Guru Row, *Inorg. Chem.* **47**, 8613 (2008).

[28] G. Pradhan, D. Swain, T. N. Guru Row, C. Narayana, *J. Phys. Chem. A.* **113**, 1505 (2009).

[29] B. Dey, Y. S. Jain, A. L. Verma, *J. Raman Spectrosc.* **13**, 209 (1982).

[30] G. Aruldhas, *Bull.Mater.sci.* **15**, 229 (1992).